CHAPTER
13

Radar Measurements and Scatterometers

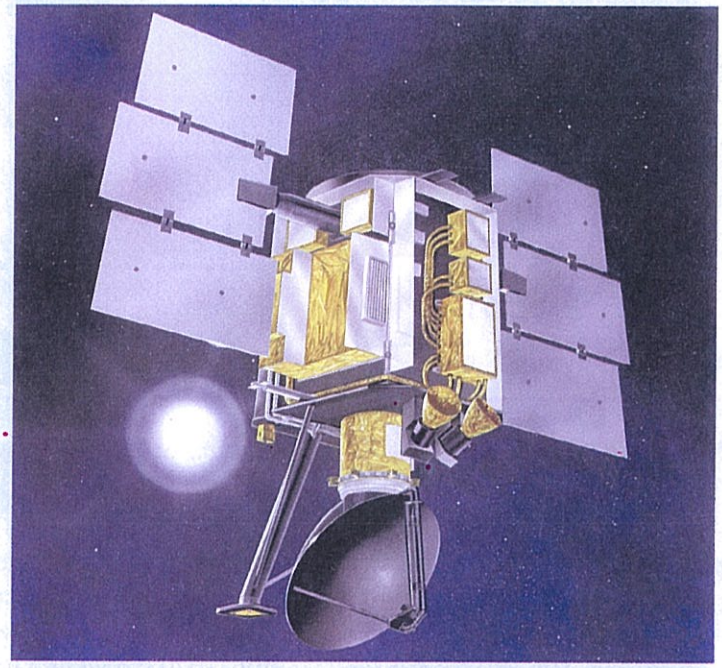

SeaWinds Scatterometer on the QuikSCAT Satellite

CONTENTS

Overview

In microwave remote sensing, information about the earth's terrain, ocean, or atmosphere must be extracted from the received microwave signal emitted or reradiated by them. For remote sensing radar, the received signal is due to reflection of the transmitted signal by the subject area. Because the radar designer can control the transmitted signal, the transmitted signal can be tailored to extract more information about the subject than is possible from passive sensing. Fundamentally, a remote sensing radar can make measurements of the received signal (1) power or amplitude, (2) frequency or Doppler shift, and (3) time delay or range. Antenna pointing provides direction discrimination capability.

▶ Even though the received signal consists of the sum of echoes from different areas within the antenna footprint, range and Doppler information makes it possible to separate or discriminate the signal components arriving from different areas within the illuminated area. ◀

This means that a radar can achieve higher resolution than that dictated by the antenna pattern alone. This discrimination is possible by exploiting the properties of the transmitted signal and the coherent nature of the received signal. In order to develop the system design and signal processing concepts necessary to perform these tasks, we devote this chapter to a description of the basic radar system configurations used in remote sensing and delve into the theory of radar measurement and discrimination.

A ***scatterometer*** is a radar designed to measure the reflectivity of desired targets. It does this by transmitting a microwave signal and then observing the signal scattered from the target and received by the antenna. The simplest scatterometers measure only the power of the scattered signal return. However, more sophisticated systems can extract additional information from the received signal using time delay and Doppler frequency shift.

13-1 CW Radar

The simplest radar employs a ***continuous wave*** (CW) transmitter. As illustrated in Fig. 13-1, part of the signal transmitted by the radar reflects or ***scatters*** off the target toward the receive antenna. The radar may be ***monostatic***, wherein the same antenna is used for transmit and receive, or ***bistatic***, wherein different antennas (located at different positions but with overlapping footprints) are used for transmit and receive. In the radar signal flow diagrams illustrated in Fig. 13-1, the received signal is mixed with a copy of the transmitted signal. This is known as ***homodyne*** processing and is used to shift the frequency of the received signal down to baseband to simplify the signal processing. The receiver then amplifies the mixed-down signal and passes it on to an indicator or processor that extracts the characteristics of interest.

For a single stationary point target, the received signal is a time-delayed, attenuated copy of the transmitted signal. The time delay arises from the time-of-flight of the signal from the transmit antenna to the target and back to the receive antenna. The signal amplitude depends on the range, antenna gain, frequency, and the radar cross section (RCS) of the target, as given by the radar equation derived in Section 5-4. If the target is moving relative to the radar, the received signal has a slightly different frequency due to the Doppler shift caused by the motion of the target relative to the radar.

13-1.1 Target Stationary Relative to Radar

In a CW radar the transmit signal voltage $v_t(t)$ can be expressed as

$$v_t(t) = A\cos(2\pi f_0 t). \tag{13.1}$$

Limiting our attention to monostatic systems for simplicity,* the two-way signal ***time of flight*** T is related to the distance R between the radar and target by

$$T = \frac{2R}{c}. \tag{13.2}$$

*For a bistatic radar with separate transmit and receive antennas $2R$ is replaced by the sum of the distances between the target and transmit antenna R_t and target and receive antenna R_r.

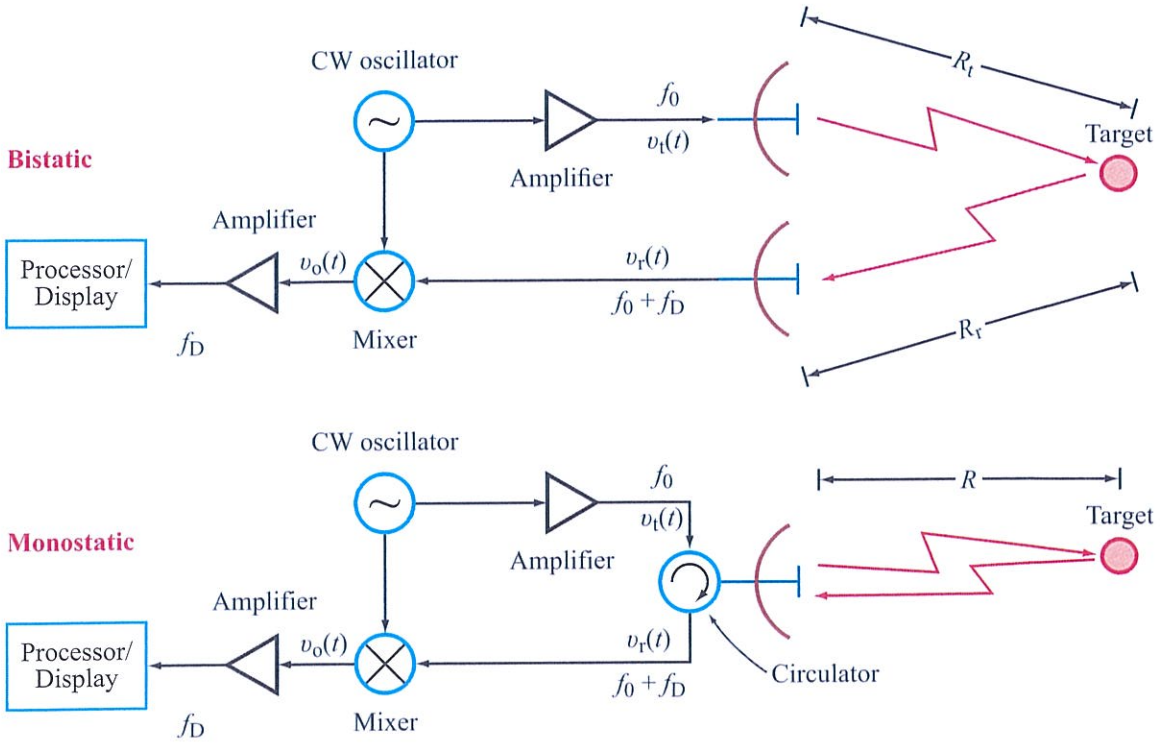

Figure 13-1: CW radar in bistatic and monostatic configurations.

The received signal $v_r(t)$, when the target is not moving relative to the radar, is

$$v_r(t) = K\cos[2\pi f_0(t-T)] = K\cos(2\pi f_0 t - \phi), \quad (13.3)$$

where K is a constant computed from the radar equation given by Eq. (5.29b):

$$K = A\,\frac{G\lambda}{(4\pi)^{3/2}R^2}\,\sqrt{\sigma_{pq}}\,, \quad (13.4)$$

and the signal phase shift ϕ due to the signal time-of-flight is

$$\phi = 2\pi f_0 T = 2\pi f_0 \cdot \frac{2R}{c} = \frac{4\pi R}{\lambda}\,. \quad (13.5)$$

In Eq. (13.4), G is the antenna gain in the direction of the target and σ_{pq} is the target RCS for a q-polarized transmit antenna and a p-polarized receive antenna. Note that Eq. (13.3) can be written as

$$\begin{aligned} v_r(t) &= K\cos[2\pi f_0(t-T)] \\ &= K\cos(2\pi f_0 t - 2kR), \end{aligned} \quad (13.6)$$

where $k = 2\pi/\lambda$ is the wave number. The phase ϕ, modulo 2π, can be determined by comparing the transmitted and received signals. This can be done with a mixer that, in effect, multiplies the two signals together. The mixer output $v_0(t)$ in Fig. 13-1 is

$$\begin{aligned} v_0(t) &= v_t(t)\,v_r(t) \\ &= [A\cos(2\pi f_0 t)][K\cos(2\pi f_0 - \phi)] \\ &= \frac{AK}{2}\,[\cos(4\pi f_0 t - \phi) + \cos\phi]\,. \end{aligned} \quad (13.7)$$

After lowpass filtering, only the second term, known as the *baseband* term, is retained and $v_0(t)$ becomes

$$v_0(t) = \frac{AK}{2}\cos\phi = \frac{AK}{2}\cos 2kR = \frac{AK}{2}\cos\left(\frac{4\pi R}{\lambda}\right). \quad (13.8)$$

(baseband signal)

Note that the output is a constant value that does not change with time if the relative range between the target and radar is fixed. It only changes if the range to the target changes. We note that for an ideal sine wave, only ϕ modulo 2π is significant, which corresponds to the fractional part of $2R/\lambda$. This means that the output voltage is very sensitive to small changes in range. The output amplitude can vary from $-AK/2$ to $+AK/2$, corresponding to a change of $\lambda/4$ in the range R. At X-band ($\lambda = 3$ cm), this is a change in R of only 0.75 cm!

13-1.2 Signal Scintillation

Consider what happens when there are two targets in the scene at slightly different ranges. The received signal voltage is the sum of the signal voltages from the two targets:

$$\begin{aligned} v_r(t) &= v_1(t) + v_2(t) \\ &= K_1\cos[2\pi f_0(t - T_1)] + K_2\cos[2\pi f_0(t - T_2)] \\ &= K_1\cos(2\pi f_0 t - 2kR_1) + K_2\cos(2\pi f_0 t - 2kR_2), \end{aligned} \quad (13.9)$$

where the subscripts indicate the target number. The corresponding baseband mixer output after lowpass filtering is

$$v_0(t) = \frac{AK_1}{2}\cos 2kR_1 + \frac{AK_2}{2}\cos 2kR_2. \quad (13.10)$$

(baseband signal for 2 targets)

For the purposes of analysis, we assume that the targets have similar radar cross sections and similar (but not identical) ranges, so $K_1 \approx K_2 = K$. Using this approximation and geometric relations, Eq. (13.10) can be written as

$$v_0(t) = AK\cos[k(R_1 + R_2)]\cos[k(R_1 - R_2)]. \quad (13.11)$$

For the next step, refer to Fig. 13-2(a), which shows the geometry of the two targets and the radar. The two targets are separated by a distance of d at a mean range of $R_0 = (R_1 + R_2)/2$. If the range is sufficiently large, the two rays to the targets are nearly parallel in the vicinity of the targets so that we can approximate R_1 and R_2 as

$$R_1 \approx R_0 + (d/2)\sin\theta, \qquad R_2 \approx R_0 - (d/2)\sin\theta. \quad (13.12)$$

Substituting these approximations in Eq. (13.11) leads to

$$v_0(t) = AK\cos(2kR_0)\cos(kd\sin\theta). \quad (13.13)$$

The magnitude of the baseband voltage has the form

$$|V| = V_0\,|\cos(kd\sin\theta)|, \quad (13.14)$$

where $V_0 = AK\cos 2kR_0$ is a constant.

A plot of $|V|$ as a function of $\sin\theta$ is shown in Fig. 13-2(b). The signals from the two targets interfere with each other to reinforce or cancel each other depending on the aspect angle θ between the baseline between the targets and the direction to the radar.

▶ This interference phenomenon arises due to the *coherence* of the transmit and receive signals. Signal coherence is a fundamental property of radars. ◀

It is instructive to consider the characteristics of this pattern. Note, for example, that the first null away from the origin occurs at $\theta = \theta_1$ where

$$\frac{2\pi d}{\lambda}\sin\theta_1 = \frac{\pi}{2}. \quad (13.15)$$

Here the subscript 1 is used to indicate the fact that it is the first null. This equation may be solved to obtain

$$\sin\theta_1 = \frac{\lambda}{4d},$$

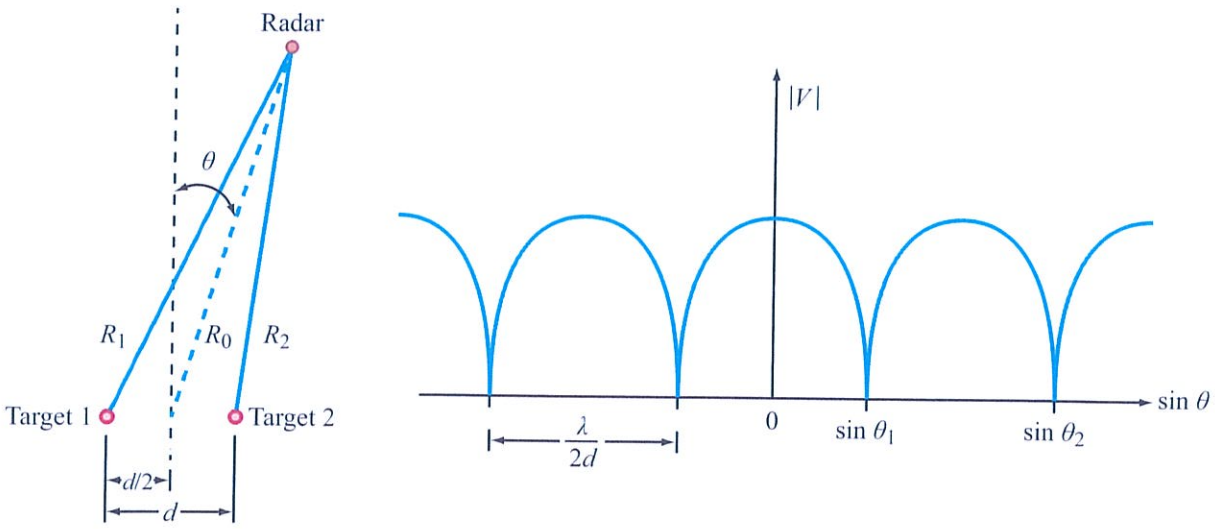

(a) Two-target geometry

(b) Two-target response

Figure 13-2: Scattering from two targets.

or

$$\theta_1 \approx \frac{\lambda}{4d}, \quad \text{if } d \gg \lambda. \tag{13.16}$$

The last result occurs when the scatterers are many wavelengths apart, so the null angle is close to zero. The second null is obtained from

$$\frac{2\pi d}{\lambda} \sin\theta_2 = \frac{3\pi}{2}, \tag{13.17}$$

which leads to

$$\sin\theta_2 = \frac{3\lambda}{4d},$$

or

$$\theta_2 \approx \frac{3\lambda}{4d}, \quad \text{if } d \gg \lambda. \tag{13.18}$$

The angular spacing between the two adjacent nulls can be derived using

$$\Delta \sin\theta = \sin\theta_2 - \sin\theta_1 = \frac{\lambda}{2d},$$

or

$$\Delta\theta \approx \theta_2 - \theta_1 = \frac{\lambda}{2d}, \quad \text{if } d \gg \lambda. \tag{13.19}$$

Thus the nulls in θ are spaced by approximately the inverse of twice the target spacing in wavelengths.

When θ is fixed, the baseband signal is fixed. However, if the targets move relative to the radar, θ may vary with time. This causes the baseband signal amplitude to vary so that the signal appears to "fade" in strength with time. This ***fading*** occurs due to the coherent nature of the scattered signals as discussed in detail in Section 5-6. Additional targets leads to more complicated fading patterns and signal fluctuations.

13-1.3 Target Moving Relative to Radar

When the target is moving relative to the radar, the received signal is also ***Doppler-shifted***. The ***Doppler frequency*** is the rate of change of the phase of the signal due to the changing distance between the radar and target. We note that the instantaneous frequency of a sine wave is the time derivative of the argument of the sine wave. Thus, the instantaneous frequency ω of the received signal in Eq. (13.6) is

$$\omega = \frac{d}{dt}(2\pi f_0 t - 2kR)$$

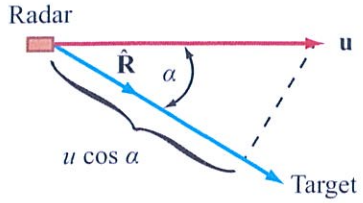

Figure 13-3: Doppler geometry.

$$= 2\pi f_0 - 2k\frac{d}{dt}R = 2\pi f_0 - \frac{4\pi}{\lambda}\frac{d}{dt}R. \qquad (13.20)$$

The frequency f of the received signal is then

$$f = \frac{\omega}{2\pi} = f_0 - \frac{2}{\lambda}\frac{d}{dt}R = f_0 + f_D, \qquad (13.21)$$

where f_D is the Doppler frequency shift of the carrier frequency f_0 caused by the change in R with time:

$$f_D = -\frac{2}{\lambda}\frac{d}{dt}R = -\frac{2u_R}{\lambda}, \qquad (13.22)$$

where u_R is the ***relative velocity*** between the radar and target in the radial direction. That is, the Doppler frequency shift is the negative of twice the radial speed in wavelengths per second.

► The negative sign comes about because the Doppler frequency is positive when the radar is approaching the target, so that R is decreasing, while the Doppler frequency is negative when the radar is receding from the radar when R is increasing. ◄

The radial component of the velocity u_R may be obtained from the total velocity vector $\mathbf{u}$ and the vector distance $\mathbf{R}$ by (Fig. 13-3)

$$u_R = -\mathbf{u}\cdot\frac{\mathbf{R}}{|\mathbf{R}|} = -u\cos\alpha, \qquad (13.23)$$

where α is the angle between the velocity vector and the radius vector from the radar to target. Hence, we may

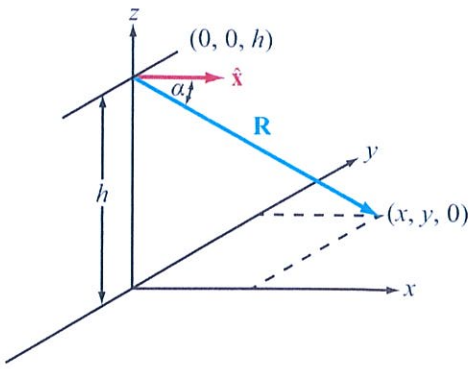

Figure 13-4: Geometry for Doppler calculation for horizontal motion above a plane surface.

write the Doppler frequency of Eq. (13.22) as

$$f_D = -\frac{2\mathbf{u}\cdot\mathbf{R}}{\lambda R}. \qquad (13.24)$$

If we assume that the radar is traveling in the positive x direction as shown in Fig. 13-4, then

$$\mathbf{u} = \hat{\mathbf{x}}u \qquad (13.25a)$$

and

$$\mathbf{R} = \hat{\mathbf{x}}x + \hat{\mathbf{y}}y - \hat{\mathbf{z}}h. \qquad (13.25b)$$

Using these definitions in Eq. (13.24) leads to

$$f_D = -\frac{2ux}{\lambda\sqrt{x^2+y^2+h^2}}. \qquad (13.26)$$

For a fixed value of f_D and h, this expression is a hyperbolic equation in x and y. The magnitude of the Doppler shift is largest when the radar is moving directly toward or away from the target; this value is defined as f_{D0},

$$f_{D0} = \pm\frac{2u}{\lambda}. \qquad (13.27)$$

Thus, the maximum range of Doppler frequencies extends from $-f_{D0}$ to $+f_{D0}$. Choosing various values within this range, we can plot lines of constant Doppler

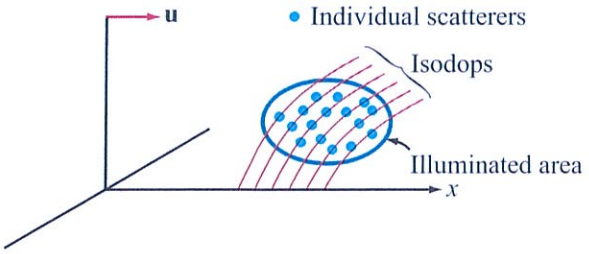

Figure 13-5: Multiple targets within an antenna footprint.

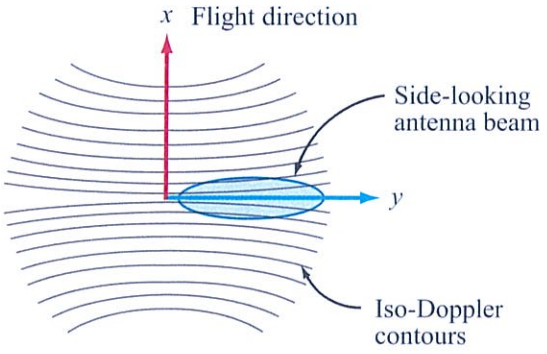

Figure 13-6: Iso-Doppler contours for horizontal motion above a plane surface. The oval represents the surface illumination area of the antenna mainlobe of a side-looking radar.

shift on the surface. These lines are known as ***iso-Doppler lines*** or ***isodops***. Figure 13-5 illustrates an evenly spaced set of isodops for a radar moving in the x direction over a stationary plane. Scatterers along the same isodop generate the same Doppler shift.

As an aside, an important special case of Eq. (13.26) occurs for a side-looking radar. For a side-looking radar traveling in the x direction, as shown in Fig. 13-6, the antenna is pointed to one side, along the y direction (or $-y$ direction). If the antenna beam is sufficiently narrow so that $x^2 \ll y^2$ over the mainlobe of the antenna on the surface, Eq. (13.26) can be approximated as

$$f_D = -\frac{2ux}{\lambda\sqrt{x^2+y^2+h^2}} \approx -\frac{2ux}{\lambda\sqrt{y^2+h^2}}. \qquad (13.28)$$

This expression suggests that the Doppler frequency in the side-looking case is approximately linearly proportional to the along-track displacement x for a narrow-beam antenna.

When there are multiple targets in the illumination area shown in Fig. 13-5, the received signal is the linear sum of the returns from all targets. Since each target has a different x and y position, each target has a slightly different combination of Doppler shift and range or phase offset. This corresponds to the distributed target model introduced in Section 5-7. As the platform moves past the target, the relative phases and Doppler frequencies vary, resulting in time-varying signal fading and scintillation. This is discussed further later.

The isodop plot in Fig. 13-6 suggests a strategy whereby we can ***discriminate*** between different areas within the antenna illumination area because different areas of the antenna illumination pattern in Fig. 13-6 have different Doppler frequencies.

> ▶ By appropriately bandpass-filtering the received signal we can separate the return from one area (defined by the antenna pattern and the Doppler frequencies that fall within the bandpass filter) and another area similarly defined but for a different range of Doppler frequencies. ◀

This enables resolution of the antenna footprint into smaller areas by filtering the signal based on the Doppler frequency. Note that this is possible due to the Doppler shift of the received signal relative to the transmitted signal and requires that the radar be phase coherent.

13-2 Pulsed Radar

A CW radar transmits and receives continuously. However, signal leakage from the transmitter to the receiver limits its performance. As a result, most remote-sensing radars are pulsed. A ***pulsed*** radar transmits short signals, and then "listens" for the returns during the intervals between the transmit pulses. The transmit ***pulse length*** τ and ***pulse repetition frequency*** (PRF) f_p are chosen so that the desired return signal can

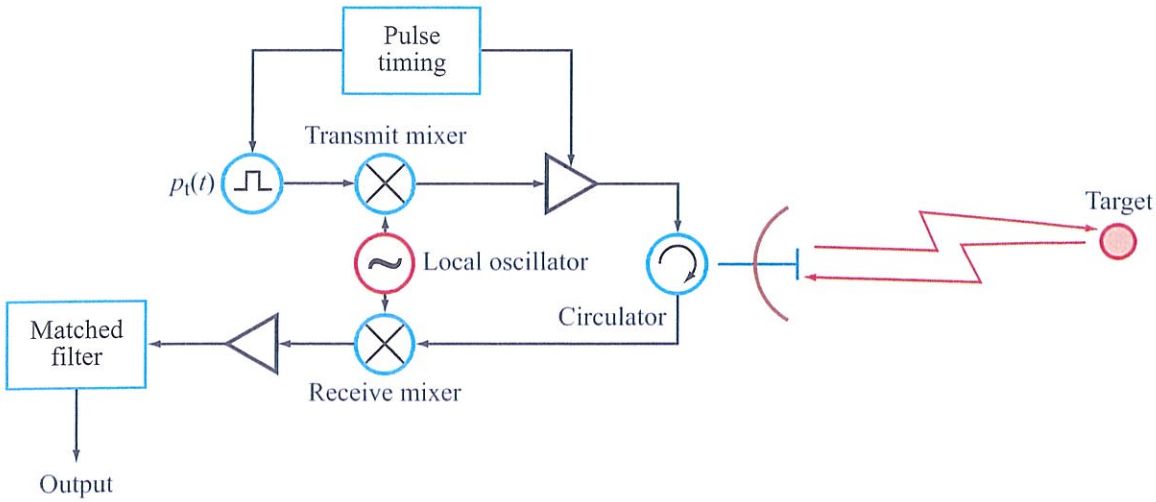

Figure 13-7: Pulsed-radar configuration.

be received without interference from the transmitted signal. On many radars, the timing is set so that there is only one pulse in flight at a time, though some radars employ multiple pulses in flight at a time.

Pulsed radars differ from CW radars by including a scheme to ***pulse-modulate*** the transmit signal as shown in Fig. 13-7. In this figure, the voltage of the transmitted pulse, represented by $p_t(t)$, is modulated or frequency-shifted from baseband to the transmit carrier frequency. Note that all radars generate baseband pulses; some radars generate transmit pulses by turning on and off a CW oscillator.

For a point target, the received pulse is a replica of the transmitted pulse delayed in time by an amount $T = 2R/c$:

$$v_r(t) = a(T)\, p_t(t - T) = a(R)\, p_t\left(t - \frac{2R}{c}\right), \quad (13.29)$$

where $a(T)$, and equivalently $a(R)$, is a factor that contains all system, target, and attenuation parameters, and $p_t(t)$ describes the transmitted pulse. For an area target containing n scatterers, the voltage received by the radar is the sum of all their contributions:

$$\begin{aligned} v_r(t) &= \sum_{i=1}^{n} a(T_i)\, p_t(t - T_i) \\ &= \sum_{i=1}^{n} a(R_i)\, p_t\left(t - \frac{2R_i}{c}\right), \end{aligned} \quad (13.30)$$

where $a(T_i)$ describes the amplitude of the backscattered voltage due to the ith scatterer at time delay T_i (or range R_i). For a ***rectangular pulse*** of duration τ,

$$p_t(t) = \begin{cases} V_0 \cos 2\pi f t & \text{for } 0 \le t \le \tau, \\ 0 & \text{otherwise.} \end{cases} \quad (13.31)$$

If the radar is moving relative to a point target i, the received voltage waveform is

$$p_r\left(t - \frac{2R_i}{c}\right) = \begin{cases} V_0 \cos\left[2\pi(f + f_{D_i})\left(t - \dfrac{2R_i}{c}\right)\right] & \text{for } T_i < t < T_i + \tau, \\ 0 & \text{otherwise,} \end{cases} \quad (13.32)$$

where T_i is the roundtrip time delay to target i, and f_{D_i} is the ***Doppler shift*** associated with that target.

Pulsing the transmit signal enables a capability not possible with passive sensors: ***range discrimination***—the ability to discriminate between targets at different ranges within the antenna illumination area. This capability is illustrated with the aid of Fig. 13-8. The figure shows $p_t(t)$ for a rectangular pulse approaching two targets at different ranges. In Fig. 13-8(a) targets 1 and 2 give radar echoes that cannot be separated or ***resolved*** because the return echoes overlap due to the fact that the two targets are too close together. At time t_1 the pulse has not returned from either target. At t_2 enough time has elapsed so that a return has started from target number 1. At t_3 a return has started from target 2, but target 1 is still providing a return. At t_4 no return is coming from target 1, but a return continues from target 2. And finally, at t_5 the pulse has passed both targets and no return is observed. The radar output shown separately exists for an extended period longer than the pulse, but there is no gap between the signals returned from targets 1 and 2 so they cannot be separated. The output as shown is constant, but in fact it may be different during the time when both targets are illuminated simultaneously. The return from the two targets together may be either larger or smaller than that from a single object, because the signals may either add coherently or cancel, depending upon their relative phases. The variation in amplitude, however, does not in general enable differentiation of the two targets, particularly in the presence of noise.

In Fig. 13-8(b) the two targets are far enough apart so that they can be separately resolved. That is, at t_2 the signal has started to return from target 1 and at t_3 it has ceased to return from target 1. Thus, a single unique return pulse is obtained from each target. The discrimination capability is therefore related to the duration of the pulse relative to the spacing between the two targets.

If target 1 is at a distance R_1 with corresponding round-trip time delay $T_1 = 2R_1/c$, the total time between the start of the transmitted pulse and the arrival of the tail

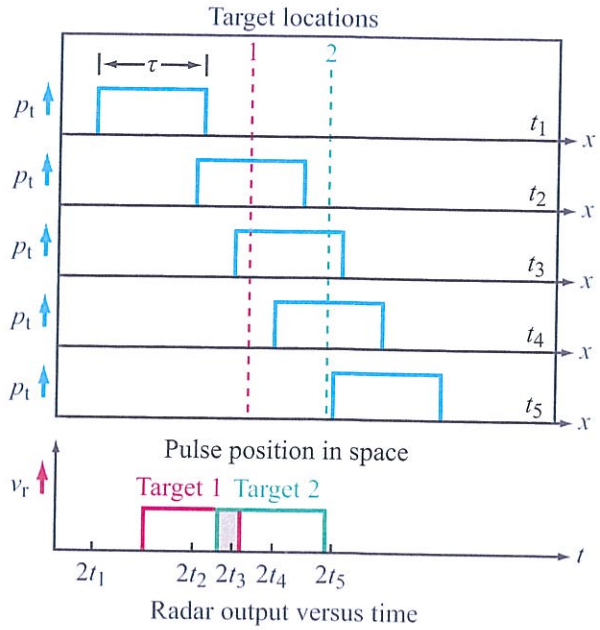

(a) Targets not resolved

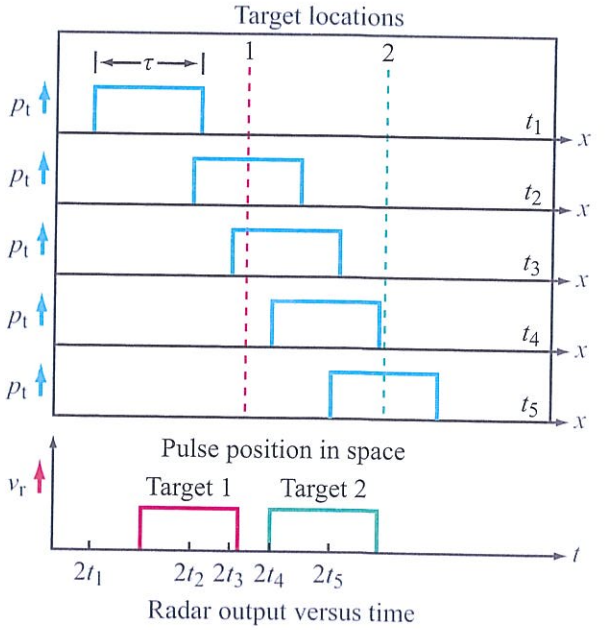

(b) Targets resolved

Figure 13-8: Examples of range resolution and target discrimination with a windowed pulse.

end of the returned pulse is

$$T_a = \frac{2R_1}{c} + \tau, \tag{13.33}$$

where τ is the pulse length. For target 2, the earliest response time, corresponding to the arrival of the front end of the returned pulse, is

$$T_b = \frac{2R_2}{c}. \tag{13.34}$$

To discriminate between the two targets, T_b must be greater than T_a. The condition $T_b = T_a$ represents the minimum spacing between R_2 and R_1 such that the two targets are distinguishable on the basis of their time delay. Setting $T_b = T_a$ leads to

$$\frac{2R_1}{c} + \tau = \frac{2R_2}{c}, \tag{13.35}$$

from which we obtain the ***range resolution***

$$\Delta R = R_2 - R_1 = \frac{c\tau}{2}. \tag{13.36}$$

A more realistic pulse-shape example is shown in Fig. 13-9, where the pulse shape is no longer rectangular—either by design or due to unavoidable filtering in the hardware. In the left column, the two targets are so close together that the returns overlap. A small decrease in power at the midpoint is indicated, as would be found if the two returns were in phase with each other. However, the presence of two targets in this situation can only be established if the noise level is small enough that the dip between the two returns can be reliably interpreted. In the middle example the targets are somewhat farther apart, and have a correspondingly deeper dip between the two returns. In the right column, the targets are far enough apart so that the response goes essentially to zero between them, and one can clearly establish that two distinct targets are present.

We observe that the return signals from targets at different ranges or time delays can be separated based on the pulse shape and length. For a platform moving horizontally over a flat surface, Fig. 13-10 displays lines

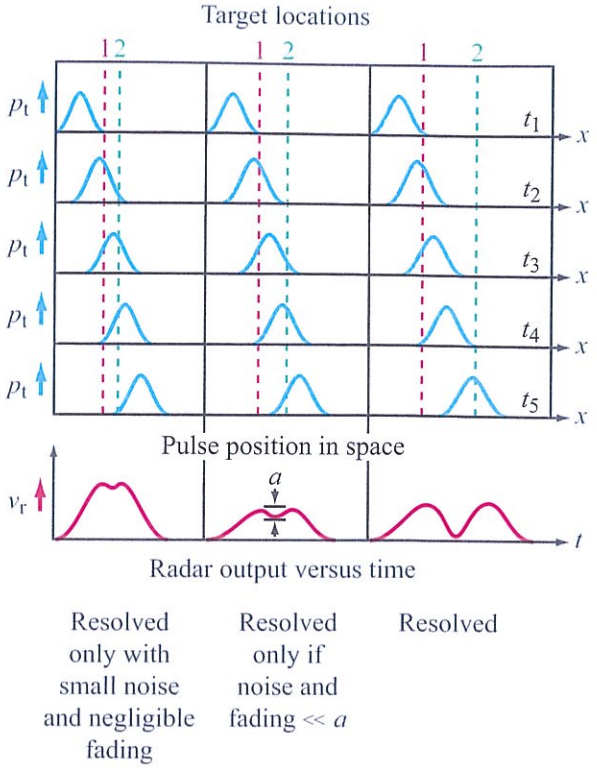

Figure 13-9: Examples of range resolution and target discrimination with a windowed pulse.

of constant range. These ***isorange lines*** define regions of the surface that generate return signals received by the radar at the same time.

Different areas of the antenna illumination pattern in Fig. 13-10 have different ranges, corresponding to different time delays. The return signals from these different regions within the footprint can be separated by ***time-filtering*** the data; i.e., only looking at the data within a short ***time window*** or ***gate***. Such filtering is known as ***range gating***. Range gating enables the radar to resolve (discriminate between) targets at different ranges.

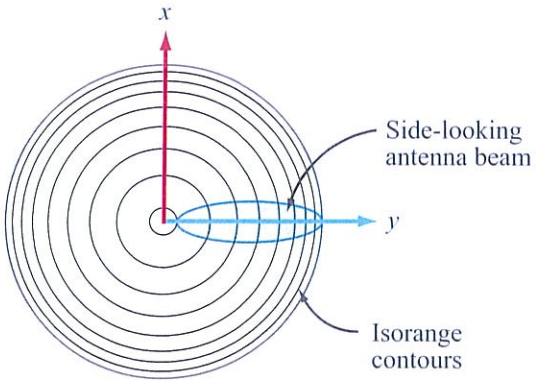

Figure 13-10: Isorange contours over a plane surface. The oval represents the surface illumination area of the mainlobe of an antenna for a side-looking radar traveling along the x direction. Isorange contours are equally spaced, but ground-range contours are not.

13-3 Range and Doppler Resolution

► In microwave sensing, ***resolution*** is the spacing (expressed in terms of angle, range, or speed as appropriate) between the points at which the response power is half the peak-power response. ◄

That is, the resolution is defined as the half-power width of the response. This is illustrated in Fig. 13-11, where the resolution w is shown as the width between the half-power points in the response from the target sensed.

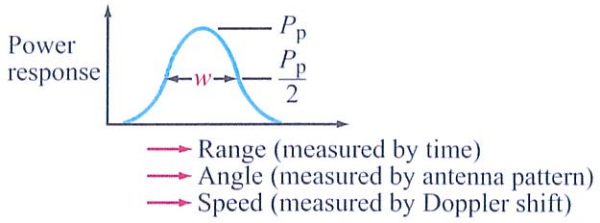

Figure 13-11: Radar definition of resolution—the half-power width.

The microwave system obtains ***discrimination*** and, hence, resolution by measurement of one or more of the three quantities: *angle, range,* and *speed.* Angular discrimination is defined by the beamwidth of the antenna. If the antenna has a narrower beam, the discrimination is better and the resolution distance on the ground is smaller: we say the resolution is ***finer***. Essentially, the ***angle resolution*** is set by the 3 dB (one-half power) beamwidth of the antenna illumination pattern on the surface.

Range resolution or distance resolution, is obtained through discrimination of time delay, which is equivalent to a range discrimination because of the known constant speed of the electromagnetic wave. Many different kinds of time delay techniques may be used in radar. The most common is pulsed operation as indicated in the examples shown in Figs. 13-8 and 13-9. ***Pulse compression*** or ***range compression***, discussed later, is an extension of this idea and can result in finer range discrimination.

Doppler frequency resolution and discrimination capability arise because the received frequency is proportional to the relative speed between the object sensed and the radar system. Thus, a filter discriminating the different frequencies received is capable of discriminating the different speeds. Different points on the earth have different relative speeds, so filters that distinguish relative speeds may be used to discriminate between signals from different parts of the surface of the earth.

Figure 13-12 illustrates the different techniques and their combinations for a microwave system carried on an aircraft traveling horizontally above the surface of the earth. In Fig. 13-12(a) angle measurement alone is used; that is, the beamwidth of the antenna establishes the resolution. The dark area on the ground lies within the half-power contours of the antenna pattern and therefore is defined as the resolvable area or ***resolution cell*** for an angle-only system. Passive microwave (radiometer) systems depend on angle resolution defined by the antenna pattern. Because both the range and speed measurement are based on comparison of the received signal with modulation imposed at a transmitter, and

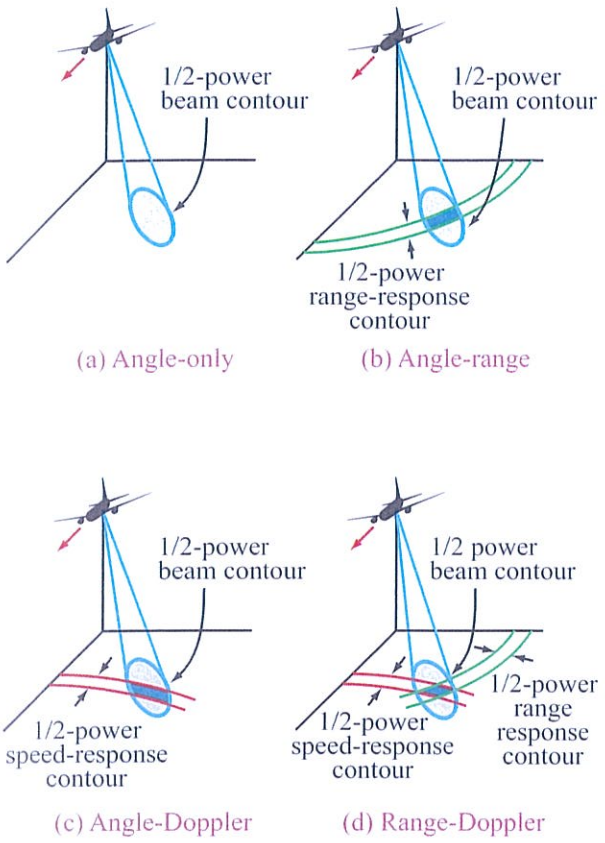

Figure 13-12: Methods for resolution in microwave sensing: (a) angle only, (b) angle and range, (c) angle and Doppler, (d) range and Doppler.

since the radiometer has no transmitter, these methods are not available to it.

In Fig. 13-12(b) the ***combination of range (distance) and angle*** resolution techniques is shown. If only range measurement is used (i.e., if the antenna beam illuminates the entire surface of the ground), the resolution cell is a ring lying between the two half-power range response contours. By combining the angle measurement and range measurement, the resolvable region or resolution cell is limited to the smaller dark area. In this case the antenna pattern is narrow in one direction and wide in the other direction. Range resolution allows breaking up the wide direction of the illuminated ground into smaller segments. The narrow direction of the antenna beam is used for resolution in angle.

Figure 13-12(c) shows a ***combination of angle and Doppler*** measurements used for resolution. Here, half-power Doppler response contours are illustrated on the surface. As previously noted, for horizontal motion above a plane surface, these contours are hyperbolas, so the resolution cell is a hyperbolic-shaped strip like that shown in the figure. By combining the angular and Doppler responses, a smaller resolvable area, as illustrated by the dark area, can be obtained. This method has been widely used in airborne and spaceborne scatterometer systems.

Figure 13-12(d) shows a ***combination of range and Doppler*** discrimination to establish the small resolution cell shown by the dark area as the intersection of the isorange and iso-Doppler contours.

► Since the half-power Doppler-response and half-power range-response contours may be made closer together than the antenna beamwidth, the resolution obtained by combining range and Doppler techniques is usually much finer than that obtained when an angle measurement is used. This idea is the basis for ***synthetic-aperture radar*** (discussed in Chapter 14) and provides the finest possible resolution. ◄

Since passive radiometers must generally depend on angular resolution alone, their ability to obtain a small resolution cell on the ground is limited. Hence, when fine resolution is required, radar is needed. For some applications where fine resolution is not required the selection between the sensor classes (active versus passive) may be made on the basis of the ability of one or the other (or a combination) to best determine the parameters of interest.

13-4 Frequency-Modulated Radar

A CW radar has no range- or timing-discrimination capability. This can be understood intuitively by noting that the time resolution of a CW radar is equivalent to

an infinitely long pulse length. However, if ***frequency modulation*** (FM) of the transmit signal is employed, range resolution can become possible. In this section we examine the operational principles of FMCW and pulsed-FM radar.

In an ***FMCW radar*** the signal is continuously transmitted and received, but the signal frequency is varied as a function of time. While other modulation schemes are possible, ***linear FM*** (LFM) is most commonly used. Figure 13-13(a) illustrates the instantaneous transmit signal frequency for an LFMCW radar. The transmit signal is linearly swept across a band B of frequencies, from f_1 to f_2, in a time $T_R/2$, where T_R is the ***modulation period***. In this figure, the sweep or ***ramp rate*** α, which is the same for both rising and falling portions of the signal modulation, is

$$\alpha = \frac{2B}{T_R} \quad \text{(Hz/s)}. \tag{13.37}$$

The upward or downward varying LFM signals are sometimes termed ***chirps***.

The echo from a point target is a time-delayed, attenuated copy of the transmit signal just as in the cases previously considered. Usually the swept bandwidth is much larger than the maximum Doppler; i.e., $B \gg f_{D0}$. Due to the time delay, the received signal lags the transmitted signal and as a result the two signals have different frequencies with the ***intermediate frequency difference*** f_I being directly proportional to the range to the target R, as indicated in Fig. 13-13(b). From the geometry of the similar triangles in Fig. 13-13(a), it is evident that the ratio of the time delay T to $T_R/2$ is the same as the ratio of f_I to B. Thus,

$$\frac{T}{T_R/2} = \frac{f_I}{B}. \tag{13.38}$$

Upon replacing T with $2R/c$ and solving for the frequency difference f_I, we have

$$f_I = \left(\frac{4B}{cT_R}\right) R = \frac{2\alpha}{c} R, \tag{13.39}$$

where α is the ramp rate defined by Eq. (13.37). Note the direct relationship between the intermediate frequency difference f_I and the range R; the proportionality

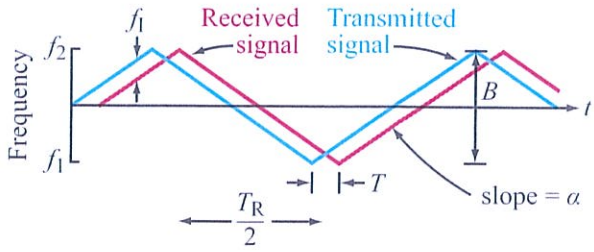

(a) Instantaneous frequencies for point target with delay T

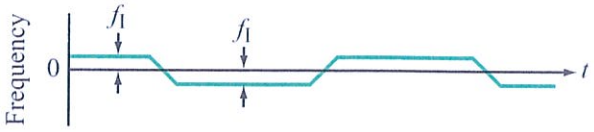

(b) Instantaneous frequency of output

(c) Expanded view of part of sweep

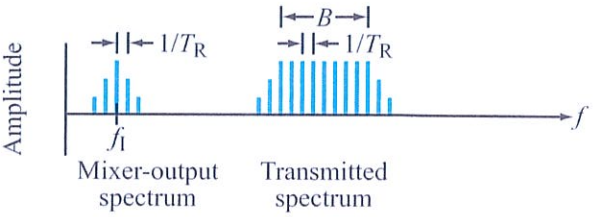

(d) Spectrum of received and transmitted signal

Figure 13-13: Operation of an LFMCW radar.

constant consists of the velocity of light c and two system constants, the modulation bandwidth B and the modulation period T_R. Upon mixing the received signal with a copy of the transmitted signal and lowpass-filtering the mixer output signal, an LFMCW radar generates a signal whose frequency is f_I. The mixing process is known as ***dechirping***. Measuring f_I by a

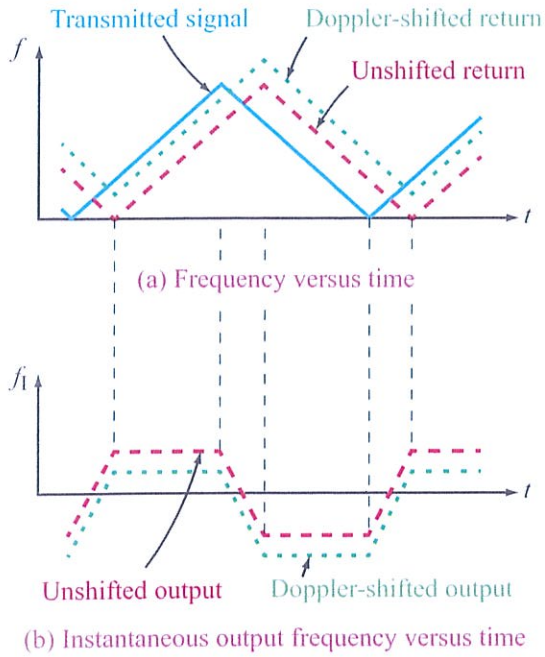

Figure 13-14: Effect of Doppler shift on an LFMCW radar: (a) frequency versus time; (b) instantaneous output frequency versus time. Note that the effect of Doppler is to shift the center frequency upward or downward depending on the sign of the Doppler shift.

frequency counter or a similar technique provides a measurement of R.

If the signal includes a Doppler shift, the time variation of f_I becomes unsymmetrical during the two halves of the modulation period T_R (Fig. 13-14). This asymmetry can provide an advantage through a processing circuit that can measure both the Doppler shift and the equivalent unshifted f_I, and then the latter is used to compute the range R.

We note that because the sweep is of finite length, the spectrum of the received signal is spread in frequency. The spectrum of a single, continuous sweep of finite duration is also continuous. However, the spectrum of the repetitive sweep is a line spectrum as illustrated in Fig. 13-13(d). So long as the sweep is of sufficient duration, the line spectrum closely approximates samples of the continuous spectrum. Mixing the transmit and receive signals and lowpass-filtering results in a signal spectrum centered at the difference frequency f_I, as shown in Fig. 13-13(d).

Over the time period of a single sweep and ignoring the transition periods at the beginning and end of the sweep, the ideal mixer output baseband signal $v_b(t)$ is

$$v_b(t) = K\cos(2\pi f_I t + \phi), \tag{13.40}$$

where ϕ is a target-dependent phase shift. When multiple targets at different ranges are present, the baseband mixer output is

$$\begin{aligned} v_b(t) &= \sum_n K_n \cos(2\pi f_{I_n} t + \phi_n) \\ &= \sum_n K_n \cos\left(\frac{8\pi B R_n t}{cT_R} + \phi_n\right), \end{aligned} \tag{13.41}$$

where we used Eq. (13.39) to relate f_{I_n} to range R_n. Note that targets at different ranges are at different frequencies. Thus, targets at different ranges can be discriminated by narrowband bandpass filters at different center frequencies corresponding to different ranges. The minimum bandwidth such filters can achieve determines the effective range resolution of the LFMCW radar.

At baseband, the signal return during a single frequency sweep is essentially a constant-amplitude cosine wave.

▶ From basic signal processing theory, the effective 3 dB bandwidth of a finite-duration CW signal of length $T_R/2$ is $2/T_R$. ◀

Hence, the effective frequency resolution Δf_I of the baseband signal is $2/T_R$; i.e., one frequency resolution element Δf_I extends from $f_a = f_0' - 1/T_R$ to $f_b = f_0' + 1/T_R$, where f_0' is the center of the resolution element bandwidth. In effect, targets must be separated by at least Δf_I to be able to discriminate between them.

From Eq. (13.39), the conversion from baseband frequency to range is

$$R = \frac{cf_I T_R}{4B}. \tag{13.42}$$

The range resolution ΔR of the LFMCW system corresponds to $\Delta f_{\mathrm{I}} = 2/T_{\mathrm{R}}$:

$$\Delta R = \frac{cT_{\mathrm{R}}}{4B}\,\Delta f_{\mathrm{I}} = \frac{cT_{\mathrm{R}}}{4B}\cdot\frac{4}{T_{\mathrm{R}}} = \frac{c}{2B}. \qquad (13.43)$$

(LFMCW range resolution)

► Thus, the effective range resolution depends only on the bandwidth of the LFMCW signal. It does not depend on the sweep length.‡ ◄

By implementing a bank of bandpass filters (or their digital equivalents), the LFMCW return signal can be resolved into multiple resolution elements. The result is that an LFMCW can have a range discrimination capability similar to pulsed radars.

We note that because the signal is continuously transmitted and received, the total signal energy is maximized compared with a pulsed radar with the same parameters. As discussed later, this maximizes the effective signal-to-noise ratio.

13-5 Matched Filtering

When processing the received signal, a radar filters the signal prior to detection. The filter that maximizes the ***signal-to-noise ratio*** (SNR) is derived from the waveform of the echo of the transmitted signal and is known as the ***matched filter***. The matched filter defines the radar's response, and hence its resolutions in time and Doppler frequency, or equivalently in range and speed. In this section we show that the matched filter indeed maximizes the measurement SNR.

A general filter can be described in terms of its ***impulse response***, which is the output of the filter for an impulse input, or its ***frequency response***, which is the Fourier transform of the impulse response. The frequency response describes the magnitude and phase of the filter output as a function of frequency. Figure 13-15 illustrates the notation for analyzing the matched filter.

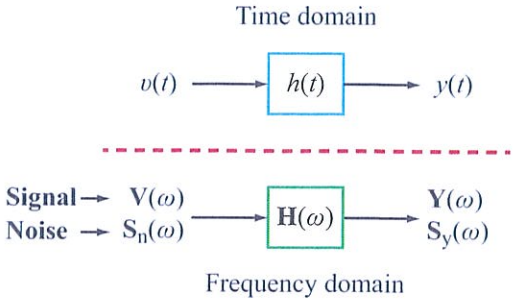

Figure 13-15: Filter inputs and outputs in the time and frequency domains.

The ***Fourier transform*** of a general continuous signal $v(t)$ is defined as

$$\mathbf{V}(\omega) = \int_{-\infty}^{\infty} v(t)\, e^{-j\omega t}\, dt \equiv \mathcal{F}\{v(t)\}, \qquad (13.44)$$

where $\omega = 2\pi f$, while the ***inverse Fourier transform*** of $\mathbf{V}(\omega)$ is

$$v(t) = \frac{1}{2\pi}\int_{-\infty}^{\infty} \mathbf{V}(\omega)\, e^{j\omega t}\, df \equiv \mathcal{F}^{-1}\{\mathbf{V}(\omega)\}. \qquad (13.45)$$

The ***spectrum*** of a signal is defined as the magnitude squared of the Fourier transform. The total signal energy $\mathcal{E}_v$ in the time and frequency domains are related by ***Parseval's theorem***,

$$\mathcal{E}_v = \int_{-\infty}^{\infty} |v(t)|^2\, dt = \frac{1}{2\pi}\int_{-\infty}^{\infty} |\mathbf{V}(\omega)|^2\, d\omega. \qquad (13.46)$$

When the signal $v(t)$ is passed through a linear time-invariant filter with an impulse response $h(t)$, the output $y(t)$ is the time-domain convolution of $h(t)$ and $v(t)$; i.e.,

$$y(t) = v(t) * h(t) = \int_{-\infty}^{\infty} v(t')\, h(t-t')\, dt'. \qquad (13.47)$$

Using the properties of the Fourier transform, it can be shown that convolution in the time domain is equivalent

‡We note that this result holds for LFM signals for time-bandwidth products greater than about 10, i.e., $T_{\mathrm{R}}B > 10$. For lower time-bandwidth products, a more precise analysis may be required.

to multiplication in the frequency domain (Ulaby and Yagle, 2013). Thus, the output signal in the frequency domain $\mathbf{Y}(\omega) = \mathcal{F}\{y(t)\}$ can be written as

$$\mathbf{Y}(\omega) = \mathbf{H}(\omega)\,\mathbf{V}(\omega), \tag{13.48}$$

where the ***filter frequency response*** $\mathbf{H}(\omega) = \mathcal{F}\{h(t)\}$ is the Fourier transform of the filter's impulse response. The signal energy $\mathcal{E}_y$ at the output of the matched filter is

$$\begin{aligned}\mathcal{E}_y &= \int_{-\infty}^{\infty} |y(t)|^2\,dt = \frac{1}{2\pi}\int_{-\infty}^{\infty} |\mathbf{Y}(\omega)|^2\,d\omega \\ &= \frac{1}{2\pi}\int |\mathbf{H}(\omega)\,\mathbf{V}(\omega)|^2\,d\omega.\end{aligned} \tag{13.49}$$

Frequency analysis for random signals has to be treated somewhat differently by using the concept of ***power spectral density*** (PSD). The PSD of a random signal, such as noise, is the Fourier transform of the signal correlation function. For a wide-sense stationary random signal $n(t)$, the ***autocorrelation function*** $R_n(t')$ is defined as

$$\begin{aligned}R_n(t') &= \langle n(t)\,n^*(t+t')\rangle \\ &= \int_{-\infty}^{\infty} n(t)\,n^*(t+t')\,dt,\end{aligned} \tag{13.50}$$

where t' is the time shift and the brackets indicate the time average, which in this case is the same as the expected value. The signal PSD is then

$$\mathbf{S}_n(\omega) = \mathcal{F}\{R_n(t')\}. \tag{13.51}$$

Note that the average random signal power is

$$\langle |n(t)|^2\rangle = R_n(0) = \frac{1}{2\pi}\int_{-\infty}^{\infty} \mathbf{S}_n(\omega)\,d\omega. \tag{13.52}$$

When a random signal $n(t)$ with PSD $\mathbf{S}_n(\omega)$ is passed through the filter $\mathbf{H}(\omega)$, the output signal's PSD $\mathbf{S}_y(\omega)$ is given by

$$\mathbf{S}_y(\omega) = |\mathbf{H}(\omega)|^2\,\mathbf{S}_n(\omega). \tag{13.53}$$

The random signal power P_y is then

$$P_y = \frac{1}{2\pi}\int \mathbf{S}_y(\omega)\,d\omega = \frac{1}{2\pi}\int |\mathbf{H}(\omega)|^2\,\mathbf{S}_n(\omega)\,d\omega, \tag{13.54}$$

while the random signal energy over a time period τ is

$$\mathcal{E}_y = \tau P_y. \tag{13.55}$$

The received signal observed by the radar includes not only the echo of the transmitted signal, but also the noise-like signal emitted by the scene and generated in the radar hardware. For the radar, this is undesired noise. The total received signal $x(t)$ can be written as

$$x(t) = v(t) + n(t), \tag{13.56}$$

where $n(t)$ is the noise component and $v(t)$ is the radar signal. As described in Chapter 7, the power associated with noise is given by

$$P_{\mathrm{n}} = kT_{\mathrm{SYS}}B, \tag{13.57}$$

where T_{SYS} is the system noise temperature and B is the system noise bandwidth. Over practical microwave bandwidths, the radiometric signal can be treated as narrow-band Gaussian white noise. Over the bandwidth B (in Hz) centered at ω_0, the noise has a constant power spectral density (PSD) of $N_0 = kT_{\mathrm{SYS}}$. Hence, the noise PSD $\mathbf{S}_{\mathrm{n}}(\omega)$ is given by

$$\mathbf{S}_{\mathrm{n}}(\omega) = \begin{cases} N_0, & \omega_0 - \pi B \le \omega_0 \le \omega_0 + \pi B, \\ 0 & \text{otherwise.}\end{cases} \tag{13.58}$$

For a radar, the noise and received signal can be treated as independent signals.

To derive the ***matched filter***, we want to determine the filter $h(t)$ (or, equivalently, $\mathbf{H}(\omega)$) that maximizes the SNR at the output of the filter. Since the filter is linear and signal and noise are independent, the matched-filtered signal and noise outputs are independent.

After filtering the noise with $\mathbf{H}(\omega)$, the noise output power P_{n} is given by

$$P_{\mathrm{n}} = \frac{1}{2\pi}\int_{-\infty}^{\infty} |\mathbf{H}(\omega)|^2\,\mathbf{S}_{\mathrm{n}}(\omega)\,d\omega. \tag{13.59}$$

Note that since the useful signal bandwidth *must* be contained within the receiver bandwidth, the integral is over the receiver bandwidth. Since the noise is assumed to be white; i.e., $\mathbf{S}_n(\omega) = N_0$ over the receiver bandwidth,

$$P_n = \frac{N_0}{2\pi} \int_{-\pi B}^{\pi B} |\mathbf{H}(\omega)|^2 \, d\omega. \tag{13.60}$$

At a time delay t_d, the matched filter output is

$$y(t_d) = \frac{1}{2\pi} \int \mathbf{H}(\omega)\, \mathbf{V}(\omega)\, e^{j\omega t_d} \, d\omega, \tag{13.61}$$

so the power of the matched filter is given by

$$|y(t_d)|^2 = \left| \frac{1}{2\pi} \int \mathbf{H}(\omega)\, e^{j\omega t_d}\, \mathbf{V}(\omega)\, d\omega \right|^2. \tag{13.62}$$

The matched filter output noise power at a particular time is given by Eq. (13.60). Thus, at the time delay t_d, the matched filter output SNR is

$$\mathrm{SNR}_{\mathrm{out}} = \frac{|y(t_d)|^2}{P_n} = \frac{\left| \frac{1}{2\pi} \int \mathbf{H}^*(\omega)\, e^{j\omega t_d}\, \mathbf{V}(\omega)\, d\omega \right|^2}{\frac{N_0}{2\pi} \int |\mathbf{H}(\omega)|^2 \, d\omega}. \tag{13.63}$$

To proceed, we use the ***Schwartz inequality*** given by

$$\left| \int f(x)\, g^*(x)\, dx \right|^2 \leq \left(\int |f(x)|^2 \, dx \right) \left(\int |g(x)|^2 \, dx \right). \tag{13.64}$$

Note that equality is achieved only when $g(x) = af(x)$ for some constant a.

The numerator of the SNR expression in Eq. (13.63) is then bounded by

$$\begin{aligned} &\left| \int \mathbf{H}(\omega)\, e^{j\omega t_d}\, \mathbf{V}(\omega)\, d\omega \right|^2 \\ &\quad \leq \left(\int \left| \mathbf{H}(\omega)\, e^{j\omega t_d} \right|^2 d\omega \right) \left(\int |\mathbf{V}(\omega)|^2 \, d\omega \right) \\ &\quad = 2\pi \mathcal{E}_\upsilon \int |\mathbf{H}(\omega)|^2 \, d\omega, \end{aligned} \tag{13.65}$$

where $\mathcal{E}_\upsilon$ is the signal energy prior to matched filtering. Note that $|\mathbf{H}(\omega)\, e^{j\omega t_d}|^2 = |\mathbf{H}(\omega)|^2$. The SNR is thus bounded by

$$\mathrm{SNR}_{\mathrm{out}} \leq \frac{\mathcal{E}_\upsilon \int |\mathbf{H}(\omega)|^2 \, d\omega}{N_0 \int |\mathbf{H}(\omega)|^2 \, d\omega} = \frac{\mathcal{E}_\upsilon}{N_0}. \tag{13.66}$$

Based on the Schwartz inequality, this bound, which gives the maximum signal-to-noise ratio, is achieved only when

$$\mathbf{H}(\omega) = a\, \mathbf{V}^*(\omega)\, e^{-j\omega t_d}, \tag{13.67}$$

where a is an arbitrary complex constant. In the time domain this means that the optimum matched filter for time delay t_d is

$$h(t) = a\, \upsilon(t_d - t). \tag{13.68}$$

► That is, the matched filter impulse response is a time-reversed copy of the signal waveform with the specified delay. ◄

We pause to note that this result applies to the signal after bandpass filtering by the receiver. If the receiver bandwidth (including any possible Doppler shift) is less than the transmit bandwidth, the matched filter corresponds to the receiver-filtered signal. Thus, the matched filter should correspond to the expected received signal rather than merely to the transmitted signal.

A matched filter can be implemented in a variety of ways. It can be implemented as an analog filter or a digital filter after sampling the data. Recalling the filter convolution relation in Eq. (13.47) and using $h(t) = a\upsilon(t_d - t)$ as the matched filter, the output of the matched filter is

$$y(t) = a \int_{-\infty}^{\infty} \upsilon(t')\, \upsilon(t' + t_d - t) \, dt'. \tag{13.69}$$

This is recognized as the autocorrelation of $\upsilon(t)$ evaluated at the lag time $(t_d - t)$ [compare with the autocorrelation expression in Eq. (13.50)]. Thus, the matched filter can be computed by ***correlating*** the received signal with a time-delayed copy of the

transmitted signal. This is typically done causally so that the matched filter output at time delay t_d can be written as

$$y(t_d) = \int_0^{t_d} v(t)\, p_t(t - t_d)\, dt, \tag{13.70}$$

where $p_t(t)$ is the voltage waveform of the transmit signal modulation.

For an ***interrupted continuous wave*** (ICW) radar, $p_t(t)$ is a rectangular pulse given by Eq. (13.31). After removing the carrier, the matched filter impulse response is given by $h(t) = p_t(-t)$. Since this leads to a noncausal filter, we modify the matched filter by implementing a fixed time delay T_p and setting $h(t) = p_t(T_p - t)$. The time shift has the effect of shifting time of maximum SNR from $t = 0$ to $t = T_p$.

Note that for this simple case of a rectangular pulse, the matched filter is also a rectangular pulse,

$$h(t) = \begin{cases} 1, & 0 \le t \le T_p, \\ 0 & \text{otherwise.} \end{cases} \tag{13.71}$$

Such a matched filter can be implemented as a gated integrator; i.e., the signal is integrated for a period T_p at which point the output of the integrator is the matched filter output corresponding to the signal. In this case, the integrator acts like a lowpass filter on the received signal.

After removing the carrier, the received signal is a delayed, Doppler-shifted, attenuated copy of the transmit signal plus noise. Ignoring the Doppler shift and amplitude, the received signal is

$$v(t) = p_t(t - T) + n(t), \tag{13.72}$$

where $T = 2R/c$ is the signal time of flight and $n(t)$ is the noise. The matched filter output is then

$$y(t) = h(t) * v(t) = h(t) * p_t(t - T) + h(t) * n(t). \tag{13.73}$$

In the noise-free case, $y(t)$ is the convolution of two boxcar functions, which results in a triangle function at the output of the matched filter; i.e., the matched filter output is

$$y(t) = \begin{cases} (t - T - \tau), & T - 2\tau \le t \le T + \tau, \\ (T + \tau - t), & T + \tau \le t \le T + 2\tau, \\ 0 & \text{otherwise.} \end{cases} \tag{13.74}$$

At $t = T + \tau$, the matched filter output achieves maximum SNR. This corresponds to the desired time delay and is where the output should be sampled for reporting the signal power. If the signal time-of-flight changes, the delay in the optimum point of the matched filter must also be changed. For this case, in the frequency domain, the signal, matched filter, and output spectra are

$$\mathbf{P}(\omega) = \mathcal{F}\{p(t)\} = e^{-j\omega\tau}\left(\frac{\sin\omega}{\omega}\right) \tag{13.75}$$

and

$$\mathbf{H}(\omega) = \mathcal{F}\{h(t)\} = e^{j\omega\tau}\left(\frac{\sin\omega}{\omega}\right), \tag{13.76}$$

so that

$$\mathbf{Y}(\omega) = \mathcal{F}\{y(t)\} = \left(\frac{\sin\omega}{\omega}\right)^2. \tag{13.77}$$

What if the matched filter does not match the received signal? The consequence is that at the output, the signal-to-noise ratio is less than optimum. Filter mismatch is considered in the discussion of the radar ambiguity function in Section 13-9.

The ***time resolution*** or ***range resolution*** corresponds to the width of the output of the matched filter between half-power points. From Eq. (13.74) for a rectangular pulse of length τ, the time resolution is τ. This yields a range resolution ΔR for an ICW pulse of

$$\Delta R = \frac{c\tau}{2}. \tag{13.78}$$

Since the 3 dB bandwidth of a rectangular pulse is approximately $1/\tau$, this result demonstrates that the radar time (and therefore range) resolution is related to the inverse of signal bandwidth. This is true for all pulse modulation schemes. Amplitude modulating the pulse shape acts like a window on the pulse spectrum. This reduces sidelobes, but widens the mainlobe of the pulse spectrum. Thus in general, the range resolution of a pulsed radar system can be written as

$$\Delta R = \alpha_0 \frac{c\tau}{2}, \tag{13.79}$$

where $\alpha_0 \ge 1$ is a parameter that depends on the pulse shape.

13-6 Pulsed-FM Radar

Some of the advantages of pulsed and LFMCW operation can be combined by generating frequency modulated pulses. Such radars are sometimes termed ***chirp radars***. In a chirp radar, the transmit signal is modulated in amplitude, frequency, and/or phase.

► Usually, the received signal is passed through a ***matched filter*** to maximize the signal to noise ratio at the receiver output. ◄

The most common pulse modulation is probably linear FM (LFM), but binary-encoded phase modulation is also used. Many chirp radars also amplitude modulate or shape the pulse envelope to control the frequency content of the transmitted signal. Since the received signal is a function of the transmit signal, modulating the transmit signal also controls the received signal properties.

The general principle of an LFM chirp radar is illustrated in Fig. 13-16(a). The transmit signal consists of a sequence of LFM signals, in this case upward sweeps, separated by a time gap dedicated to receiving signals. The pulse duration is τ, and its bandwidth after LFM modulation is B. Note that B is larger than $1/\tau$. There are various ways to do the modulation, but one commonly used approach is to generate a linear FM baseband chirp such as that shown in Fig. 13-17 and mix it with a fixed-frequency carrier to generate each transmitted pulse. In many modern systems, the transmit modulation signal is digitally generated.

The received signal from a point target consists of a time-delayed, attenuated, Doppler-shifted copy of the transmitted pulse. Using the concepts introduced in the previous section, the signal can be processed by ***dechirping*** the signal and using a bandpass filter (Section 13-4). These two operations can be combined into a single operation by designing a bandpass filter that has a constant amplitude, but a frequency-varying time delay as illustrated in Fig. 13-16(b) and (c). The filter time delay is chosen so that the frequency transmitted (and received) first is delayed long enough so that it arrives at the output of the filter at the same time as the frequency transmitted last. All the frequencies in between also arrive at this time, so they are superimposed at a single instant of time at the filter output. Of course, because of the finite pulse length and bandwidth, the actual signal has a sinc-like envelope as illustrated in Fig. 13-16(b). With a bandwidth B, the approximate width of the output pulse is $1/B$, and if the transmitted amplitude is constant during the pulse, it takes the form of a $(\sin x)/x$ pulse.

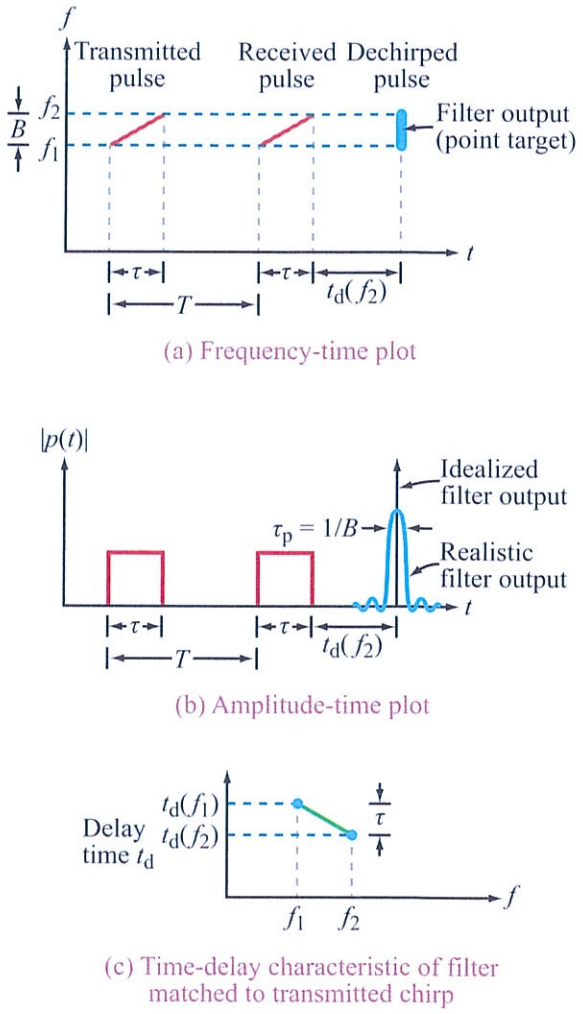

Figure 13-16: Principle of operation of an LFM chirp radar.

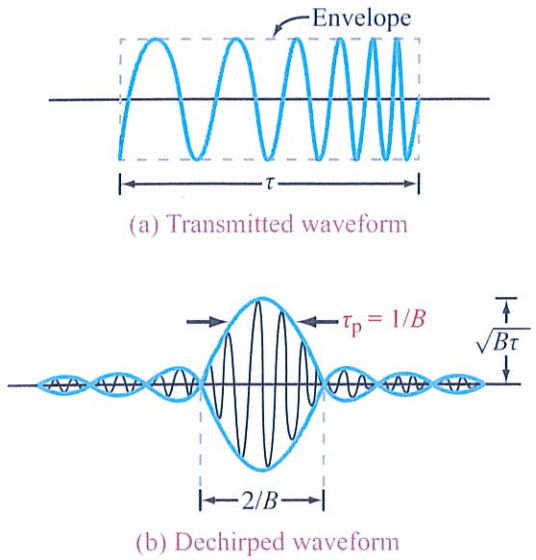

Figure 13-17: Waveforms for an LFM chirp radar with a point target. Note that the transmitted waveform has a boxcar envelope while the dechirped waveform has a sinc-function envelope.

Figure 13-16(c) shows the delay characteristics of the matched filter to the transmit pulse for the output shown in (b). Note that the filter time delay is the least for f_2, the last frequency transmitted, and most for f_1, the first frequency transmitted. The difference in time delay is just the duration of the pulse.

This time-delay filter is a particular implementation of the matched filter technique for this pulse. Other implementations are possible. For example, the signal can be digitized and the matched filter applied by multiplication (in the frequency domain) with the frequency response of the matched filter.

A key observation from Fig. 13-16(b) is that the matched filter "compresses" the pulse from length τ to a shorter effective length of $\tau_p = 1/B$. For this reason, matched-filter processing of the pulse signal is often termed ***pulse compression*** or ***range compression***. The ***compression ratio*** is

$$C = \frac{\tau}{\tau_p} = \tau B. \tag{13.80}$$

Note that the compressed pulse length τ_p only depends on the signal bandwidth B and not on the pulse length τ. The pulse length does, however, affect the signal-to-noise ratio of the matched filter output.

As previously shown, the signal-to-noise ratio of the matched filter output for white noise is given by Eq. (13.66); i.e., the output SNR is the ratio of the signal energy to the noise power spectral density:

$$\text{SNR}_{\text{out}} = \frac{\mathcal{E}_v}{N_0}. \tag{13.81}$$

On the other hand, the SNR at the input of the matched filter is given by the ratio of the signal power to the noise power prior to matched filtering:

$$\text{SNR}_{\text{in}} = \frac{P_v}{\int \mathbf{S}_n(\omega)\, d\omega} = \frac{\mathcal{E}_v}{N_0 \tau B}, \tag{13.82}$$

where $P_v = \mathcal{E}_v/\tau$ is the average signal power. The ***pulse compression gain*** G_{comp} is the ratio of the signal-to-noise ratio at the output of the matched filter to that at the input to the matched filter:

$$G_{\text{comp}} = \frac{\text{SNR}_{\text{out}}}{\text{SNR}_{\text{in}}} = \tau B. \tag{13.83}$$

Thus, the pulse compression gain for matched filtering is equal to the signal ***time-bandwidth product***. This means that the matched filter output signal SNR can be increased by lengthening the transmit pulse. Note that SNR_{out} depends only on the signal energy, not the details of the signal waveform, so the results can be applied to any pulse waveform.

Figure 13-17 shows the waveforms for the point-target response of the chirp radar. The transmitted waveform shown in (a) is modulated in frequency from a low frequency to a high frequency. In this example,

its amplitude is constant throughout its duration. The ***dechirped*** waveform is shown in Fig. 13-17(b), where the familiar $(\sin x)/x$ shape appears. The null-to-null width for this case is $2/B$, but the effective 3 dB width is approximately $1/B$. The amplitude is increased from 1 for the input signal to $\sqrt{B\tau}$ for the dechirped waveform.

A convenient way to analyze a linear FM pulse signal is to use complex notation. Consider the upsweep chirp transmit pulse waveform shown in Fig. 13-17(a). This is the real part of the complex pulse waveform $p_{\text{LFM}}(t)$ that can be written as

$$p_{\text{LFM}}(t) = \begin{cases} e^{j2\pi\alpha t^2/2}, & |t| \le \tau/2, \\ 0 & \text{otherwise}, \end{cases} \tag{13.84}$$

where α is the ***chirp rate*** $df/dt = B/\tau$. For a downsweep, the sign of α is negative. The exponential in Eq. (13.84) is a phase function of the form ωt, where ω is the angular frequency. The instantaneous frequency $f(t)$ of $p_{\text{LFM}}(t)$ can be computed by dividing the phase function by 2π and taking its time derivative. This gives the time-varying frequency $f(t)$ as

$$f(t) = \frac{1}{2\pi}\frac{d}{dt}(\pi\alpha t^2) = \alpha t, \tag{13.85}$$

which is a linear function of time. For the transmitted pulse plotted in Fig. 13-16(a), the minimum frequency $(-B/2)$ of the pulse modulation occurs at $t = -\tau/2$ while the maximum frequency $(B/2)$ occurs at $\tau/2$, so the bandwidth is B. A plot of the chirp spectrum for several different time-bandwidth products is shown in Fig. 13-18. In this plot the frequency axis for each plot has been normalized to simplify comparison. Note that as the time-bandwidth product increases, the spectrum becomes more and more like a boxcar function. The envelope of the Fourier transform $\mathbf{P}'_{\text{LFM}}(f)$ of $p_{\text{LFM}}(t)$ is approximately

$$\mathbf{P}'_{\text{LFM}}(f) = \begin{cases} 1, & 0 \le f \le \alpha\tau, \\ 0 & \text{otherwise}. \end{cases} \tag{13.86}$$

An approximation for the Fourier transform of this LFM chirp with a time-bandwidth product of $\tau B > 0$ is given by (Richards et al., 2010)

$$\mathbf{P}_{\text{LFM}}(f) \approx \mathbf{P}'_{\text{LFM}}(f)\, e^{-j[(\pi\tau/B)f^2 + \pi/4]}. \tag{13.87}$$

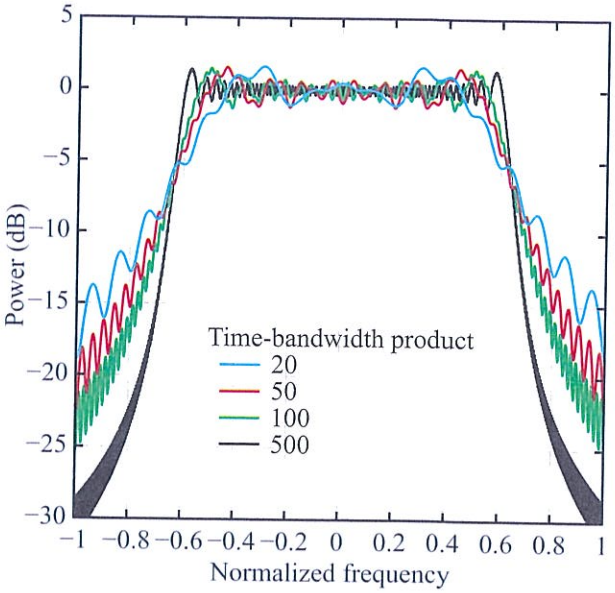

Figure 13-18: Comparisons of the spectra of linear FM chirps with different time-bandwidth products.

The normalized matched filter $h_{\text{LFM}}(t)$ corresponding to $p_{\text{LFM}}(t)$ has an impulse response that is the complex-conjugate time-reversed version of $p_{\text{LFM}}(t)$; i.e.,

$$h_{\text{LFM}}(t) = \begin{cases} e^{-j\alpha t^2/2}, & |t| \le \tau, \\ 0 & \text{otherwise}. \end{cases} \tag{13.88}$$

The normalized matched filter output $y(t)$ is obtained by convolving $h_{\text{LFM}}(t)$ and $p_{\text{LFM}}(t)$, which leads to

$$y(t) = \left(1 - \frac{|t|}{\tau}\right) \frac{\sin\left[\left(1 - \frac{|t|}{\tau}\right)\pi Bt\right]}{\left(1 - \frac{|t|}{\tau}\right)\pi Bt}, \quad |t| \le \tau. \tag{13.89}$$

This is the product of a triangle function (first term on the left) and a $(\sin x)/x$ function where x is

$$x = \left(1 - \frac{|t|}{\tau}\right)\pi Bt = \pi B\left(t + \frac{t^2}{\tau}\right). \tag{13.90}$$

Note that x is dominated by the quadratic function of time, which leads to a linear phase versus frequency, particularly near the peak of the $(\sin x)/x$ function.

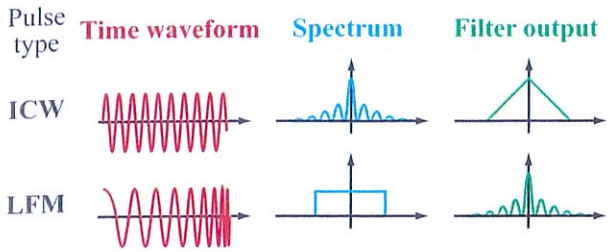

Figure 13-19: Comparison of ICW and pulsed linear FM waveforms, spectra and match filter outputs.

An intuitive explanation for the $(\sin x)/x$ function can be seen by examining the envelope of the Fourier transform of the LFM chirp given in Eq. (13.86). Assuming that the Doppler shift of the return signal is small compared with the chirp bandwidth, the envelope of the Fourier transform of the received signal is similar to the transmit signal. Thus, the matched filter output spectrum is approximately $|\mathbf{P}_{\text{LFM}}(f)|^2$, which is a boxcar function in frequency. The corresponding time-domain matched filter output is a $(\sin x)/x$ function. The width of the mainlobe is approximately $1/B$, while the peak height is τB. The peak occurs at the time delay corresponding to the pulse time-of-flight plus the time offset employed to ensure causality of the matched filter. When the received signal includes a Doppler shift the matched filter output includes a phase shift at the peak related to the Doppler shift.

For reference, Fig. 13-19 compares the properties of the ICW and pulsed LFM waveforms by displaying approximate spectra and matched filter outputs. Note that the pulsed LFM waveform has its power more uniformly spread in frequency than does the ICW pulse. For a given resolution, this enables more efficient spectrum utilization.

We note that the triangle function in Eq. (13.89) arises from the auto-convolution of the rectangular pulse envelope defined in Eq. (13.84) and acts as a window on the $(\sin x)/x$ function in the matched filter output. As previously noted, by amplitude modulating the pulse amplitude on transmit, the windowing function can be modified to control the matched filter output sidelobes. Shaping the pulse amplitude broadens the mainlobe, but suppresses the sidelobes. Because less power is transmitted during part of the pulse as a result of the pulse modulation, less total energy is transmitted and the effective SNR is reduced. Thus amplitude modulating the transmit pulse allows a trade-off between resolution (mainlobe width), SNR, and sidelobes. This trade-off applies for all pulse modulation schemes.

13-7 Pulsed Radar, General Modulation

So far, we have considered CW, ICW, pulsed, and LFM-chirp transmit modulation schemes. A variety of other modulation schemes can be used, including ***binary-coded phase modulation*** and ***frequency-hopping***. The former very rapidly varies the phase of the transmit signal according to a binary sequence, while the latter rapidly sequences through a set of frequencies in deterministic, usually cyclic order. Both approaches can be analyzed as special cases of more general pulsed signal modulation and both can be used with matched filtering to "compress" the pulse to improve the time or range resolution as well as improve the SNR.

For ***binary phase modulation***, the carrier phase is switched between 0 and π based on a binary sequence. Amplitude modulation is introduced by varying $p_{\text{t}}(t)$ to control sidelobes. A phase change of π is equivalent to changing the sign of $p_{\text{t}}(t)$. However, the phase shifts need not be limited to 0 and π.

For binary-sequence and frequency hopping modulation, $p_{\text{t}}(t)$ consists of a general amplitude term that multiplies a signal consisting of a sequence of much shorter signals called ***chips***. For binary phase modulation each chip is a complex constant, often $+1$ and -1, in a particular sequence. For frequency-hopping, each chip is a short complex sinusoid with the desired frequency offset for that chip. For example, the pulse waveform may have the functional form

$$p_{\text{t}}(t) = p_{\text{amp}}(t) \sum_{i=1}^{N_{\text{c}}} p_{\text{chip}}(i; t - iT_{\text{c}}), \qquad (13.91)$$

Table 13-1: Barker codes.

Code length	Code	Sidelobe level (dB)
2	−+, ++	−6.0
3	−−+	−9.5
4	−−+−, −−−+	−12.0
5	+++−+	−14.0
7	−−−++−+	−16.9
11	−−−+++−++−+	−20.8
13	−−−−−+++−−+−+−	−22.3

where N_c is the ***number of chips per pulse***, $T_c = \tau/N_c$, $p_{amp}(t)$ is the amplitude modulation term defined over $t = 0$ to τ, and $p_{chip}(i;t)$ is the chip term for the ith chip.

Consider the binary phase modulation sequence with $N_c = 7$ and $p_{chip}(i;t) = a_i\, p_c(t)$ where

$$p_c(t) = \begin{cases} 1, & 0 < t < T_c \\ 0 & \text{otherwise,} \end{cases}$$

with $a_i = -1,-1,-1,1,1,-1,1$. This is a particular example of a ***Barker code*** and the corresponding $p_c(t)$ chip sequence is illustrated in Fig. 13-20(b). Other Barker codes are shown in Table 13-1. ***Polyphase Barker codes*** that use more than two phase states also exist (Borwein and Ferguson, 2005).

For this binary modulation scheme the phase modulation is limited to 0° or π (180°) based on a binary sequence by multiplying by one or negative one. The matched filter for this waveform is, in essence, a cross-correlator between a stored sample of the transmitted code and the received signal. This can be implemented as suggested in Fig. 13-20 (alternate approaches can be used). If the transmitter uses a pulsed oscillator to produce pulses of duration τ, the binary code generator switches in and out a 180° phase shift, and the resulting signal is amplified and transmitted. This 180° phase shift can be inserted, as shown, in the RF chain ahead of an amplifier, or it can also be inserted between the amplifier and the antenna. The received signal comes in through the usual low-noise preamplifier and is mixed down to an IF signal. At the IF, a tapped delay line with total delay of τ is used to range compress the data. The outputs of the different taps are summed with or without phase shifting. The taps associated with the 180° phase shift on transmission have their output phase shifted by 180° on receive (in other words, the outputs are inverted). The taps with zero phase are sent directly to the adder and detector. When the time delay associated with reception is such that the first bit has just reached the end of the delay line, all of the taps in the delay line are (after suitable phase-shifting) producing signals that are in phase; hence the output of the adder is the coherent sum of the N_c chip signals. For any other position of the received pulse in the delay line, some of the pulse outputs add in phase while others add out of phase, so that the output of the summer is significantly less than N_c times the output of a single tap. This is illustrated in Fig. 13-20(d).

Table 13-2: Truth table for multiplier with +1 and −1 inputs and no carry.

Input 1	Input 2	Output
−	−	+
−	+	−
+	−	−
+	+	+

A simple algorithm for computing the output of Fig. 13-20(d) is shown here. Note that when the target is properly lined up so the chip signals add in phase, the output of the 7-bit summer is

$$(-1)(-1)+(-1)(-1)+(-1)(-1)$$
$$+1+1+(-1)(-1)+1=7.$$

In effect, the outputs for the individual bits are the same as for a multiplier with +1 and −1 inputs, as indicated by the truth table of Table 13-2. Shown below are the results of applying this to different delays for the received pulse. On the top line is the adder phase. On the second and other even lines are the phases for the received signal, and on the third and other odd lines are the outputs for the individual bits, with the sums at the right (see Table 13-3).

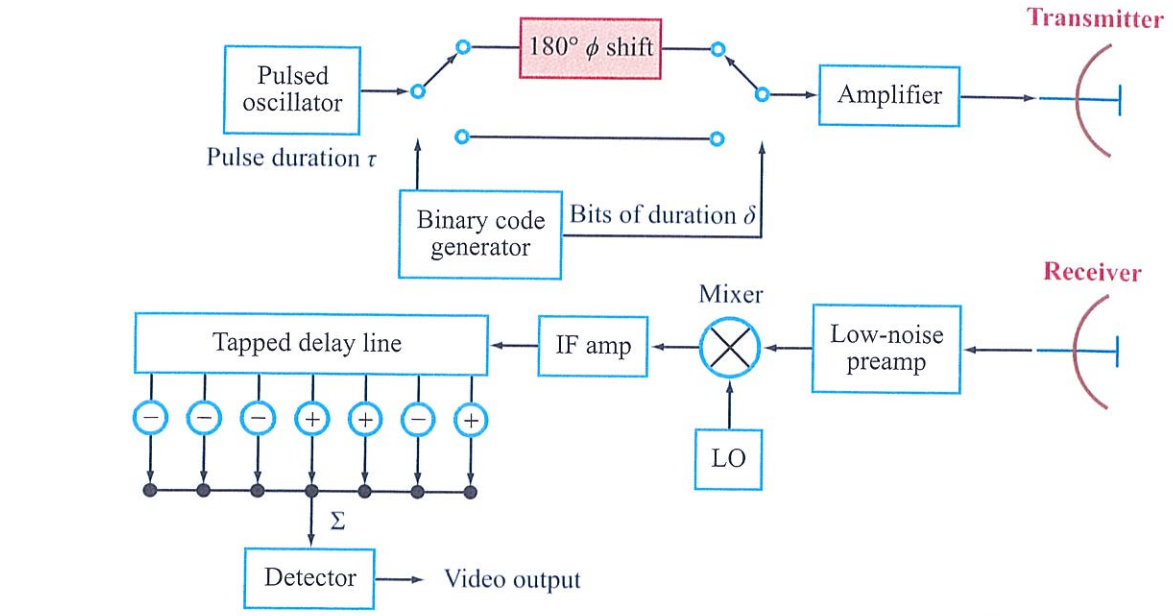

(a) System block diagram

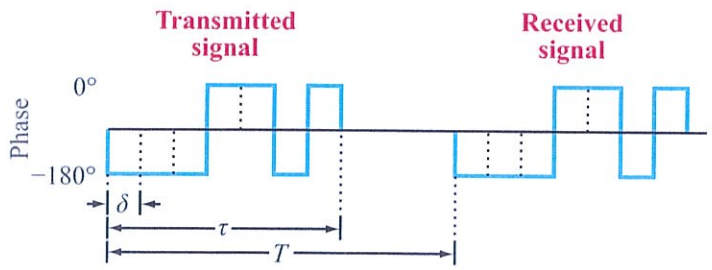

(b) Phase of signal: point target

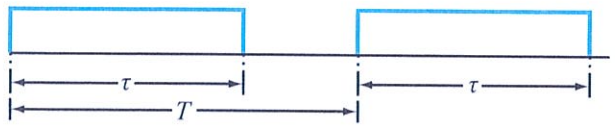

(c) Amplitude of signal: point target

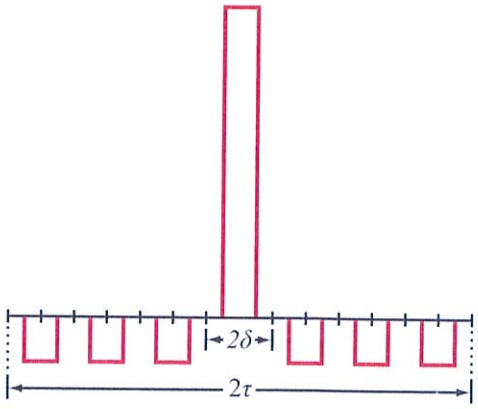

(d) Amplitude of output, showing point-target compression

Figure 13-20: Example of 7-bit binary phase-code modulation and demodulation.

Table 13-3: Processing sequence.

Adder phase	−	−	−	+	+	−	+	
1. Properly aligned	−	−	−	+	+	−	+	
Output	1	1	1	1	1	1	1	$\Sigma = 7$
2. Misaligned by T_c		−	−	−	+	+	−	
Output		1	1	−1	1	−1	−1	$\Sigma = 0$
3. Misaligned by $2T_c$			−	−	−	+	+	
Output			1	−1	−1	−1	1	$\Sigma = -1$
4. Misaligned by $3T_c$				−	−	−	+	
Output				−1	−1	1	1	$\Sigma = 0$
5. Misaligned by $4T_c$					−	−	−	
Output					−1	1	−1	$\Sigma = -1$
6. Misaligned by $5T_c$						−	−	
Output						1	−1	$\Sigma = 0$
7. Misaligned by $6T_c$							−	
Output							−1	$\Sigma = -1$

For longer codes, one of the more common types used is the ***maximal-length sequence*** (Cook and Bernfield, 1967, pp. 247–251). These also are known as m-sequences and pseudorandom sequences. They may be readily generated using an n-stage shift register, as illustrated by the example of Fig. 13-21, which generates the same code used in the example, but with pluses instead of minuses. The shift register is connected with feedback to the input. The source of the feedback in this case is two inputs from different blocks in the shift register (here block 2 and block 3) to a modulo-two adder. The modulo-two adder has the truth table shown in the figure.

In the example illustrated in Fig. 13-21, we start with the shift register loaded with all pluses. The first output is a plus when the shift command is given, but the combination of the pluses in positions 2 and 3 gives a minus as the input (at that time) into position 1. The next shift also gives a negative input to position 1 and a positive output, but for the third shift, block 2 contains a minus and block 3 a plus, so that the feedback is positive, as shown. The first of the minus inputs has now been shifted to the output. This process continues as indicated, but in the seventh shift (eighth setting of the register) the sequence begins to repeat.

Maximal-length sequences have the following properties for an n-stage shift register:

(1) Length $= 2^n - 1$.

(2) Number of pluses and minuses equal within 1 unit (balance property).

(3) Last stage must be in feedback loop.

(4) Number of feedback taps must be even.

Maximal-length sequences have been extensively studied, and the results are available in the literature. The sequences are widely used not only in radar, but in secure communication systems and for generating pseudorandom numbers for computational purposes.

Table 13-4 gives examples of maximal-length sequences. Because the length of the sequence is $2^n - 1$, a

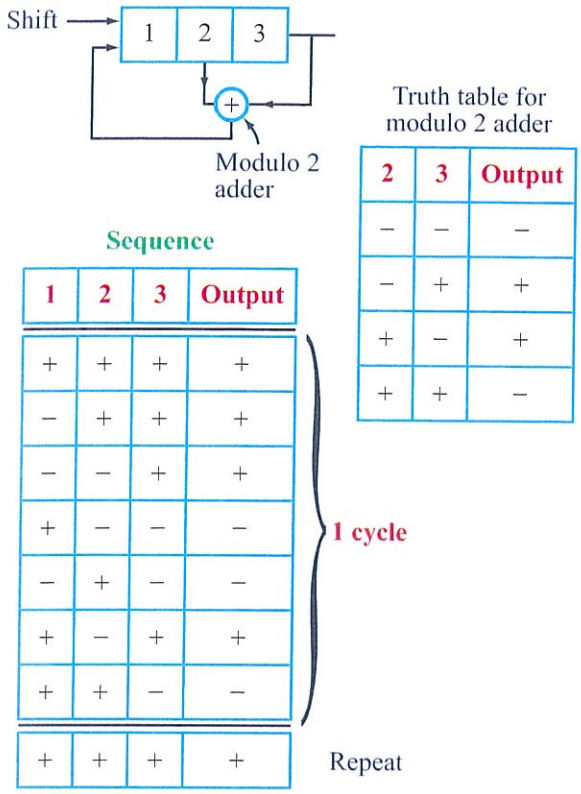

Figure 13-21: Example of generation of maximal-length sequence.

relatively short shift register may be used to obtain quite a long code. For instance, the ten-stage shift register achieves a 1023-bit code. The number of maximal sequences listed in the table depends upon the number of feasible feedback connections that will generate maximal-length sequences. Examples of feedback connections with just two connections are shown in the table. However, some of the codes are generated by use of feedback from 4, 6, or more of the blocks in the shift register.

Even though binary phase modulation is perhaps the most common discrete-step technique used for pulse compression, it is, of course, possible to use other techniques; for instance, amplitude modulation may be used, in which case the pluses represent a signal that is turned on, and the minuses a signal that is turned off.

Table 13-4: Number of binary maximal-length sequences with an n-stage shift register.

Number of stages n	Length of sequence $2^n - 1$	Number of maximumal sequences	Example of feedback connections
3	7	2	3, 2
4	15	2	4, 3
5	31	6	5, 3
10	1023	60	10, 7

Frequency modulation may also be used, in which the plus represents one frequency and the minus another. The binary phase code is used so commonly because both the modulation and the pulse compression are very easy to achieve with this method.

Nonbinary phase modulation schemes also exist. These are widely used in communication but not in radar. For example, a quaternary rather than a binary system may be used in which four 90°-phase-shifted positions represent the numbers 0, 1, 2, and 3. The subject of such codes has also been extensively studied.

Discrimination in range can be achieved with short pulses, with frequency modulation, and with longer pulses that are modulated with either FM or binary phase codes. The binary-coded system may be used on a continuous basis like the FM system, and one may use nonlinear modulation techniques. In general, however, the time resolution of a well-designed system is always approximately $1/B$.

13-8 Measurement Precision

13-8.1 Effective Number of Samples

When a random signal is measured continuously, or when the samples of the random signal are very close together relative to the spacing between independent samples, Rice (1944–45) has shown that the variance s_T^2 of the signal integrated over a time T is given by

$$s_T^2 = \frac{2}{T}\int_0^T \left(1 - \frac{x}{T}\right) R_{vf}(x)\, dx \qquad (13.92)$$

where $R_{vf}(x)$ is the autocovariance function,

$$R_{vf}(\tau) = R_v(\tau) - \overline{P_v}^2, \tag{13.93}$$

derived from the autocorrelation function $R_v(\tau)$ of the voltage $v(t)$

$$R_v(\tau) = \lim_{T\to\infty} \frac{1}{T} \int_0^T v(t)\, v(t+\tau)\, dt, \tag{13.94}$$

and the average signal power $\overline{P_v}$ is defined by

$$\overline{P_v} = \lim_{T\to\infty} \frac{1}{T} \int_0^T v^2(t)\, dt. \tag{13.95}$$

The ***effective number of independent samples*** or ***number of looks*** may be obtained by relating the expression for the signal variance in Eq. (13.92) to the expression for the variance of N independent samples; i.e.,

$$s_T^2 = \frac{\overline{P_v}^2}{N}. \tag{13.96}$$

Then, the effective number of independent samples is given by

$$N = \frac{\overline{P_v}^2 T}{2\displaystyle\int_0^T \left(1 - \frac{x}{T}\right) R_{vf}(x)\, dx}. \tag{13.97}$$

The autocovariance function may be obtained either from the known signal or from the inverse Fourier transform of the signal PSD. For noise-like signals, the latter method is the more appropriate.

An important example is band-limited white noise, which has a power spectrum given by Eq. (13.58). The autocovariance function corresponding to this power spectrum is given by

$$R_{vf}(\tau) = \overline{P_v}^2 \left(\frac{\sin \pi B\tau}{\pi B\tau}\right)^2. \tag{13.98}$$

For this case, the integration in the variance expression in Eq. (13.92) can be approximated by

$$s_T^2 = \frac{2\overline{P_v}^2}{T} \int_0^T \left(\frac{\sin \pi Bx}{\pi Bx}\right)^2 dx, \tag{13.99}$$

since x/T varies slowly over the region where the integrand has a significant value. This expression can be integrated to obtain

$$s_T^2 = \frac{\overline{P_v}^2}{\pi BT} \left[\frac{\cos \pi BT - 1}{\pi BT} + 2\int_0^{2\pi BT} \frac{\sin t}{t}\, dt\right]. \tag{13.100}$$

Note that if the time-bandwidth product BT is much greater than one, the first term in the square brackets is negligible, while the second term is approximately π. Hence, if $BT \gg 1$

$$s_T^2 \approx \frac{\overline{P_v}^2}{BT}. \tag{13.101}$$

It follows from Eq. (13.96) that for band-limited noise with $BT \gg 1$

$$N \approx BT. \tag{13.102}$$

A more exact evaluation of Eq. (13.97) is plotted in Fig. 13-22 along with some other quantities of interest. In this figure the value of the normalized standard deviation is shown and compared with $1/\sqrt{BT}$. The ***normalized standard deviation*** is the standard deviation divided by the mean. Clearly, as BT approaches 10 the approximation $N \approx BT$ becomes fairly good.

Also shown in Fig. 13-22 is the approximation $N = BT$ compared with the result of evaluating Eq. (13.97) for this case. Note that the effective number of independent samples is always somewhat larger than BT. The effective number of independent samples must start with 1 because any measurement corresponds to at least one sample. It quickly approaches a line almost parallel with the BT line and displaced from it by about 0.6. Therefore, the effective number of independent samples for large BT is about 0.6 more than BT, a difference that is unimportant for large BT but may be significant for the smaller values, as indicated by the difference between the normalized-standard-deviation curve and the curve of $1/\sqrt{BT}$. Similar curves could be derived for other spectra and autocovariance functions, but this result is illustrative of what can be expected in most cases.

When discrete signal samples spaced in time by τ are collected, a summation rather than an integration is used.

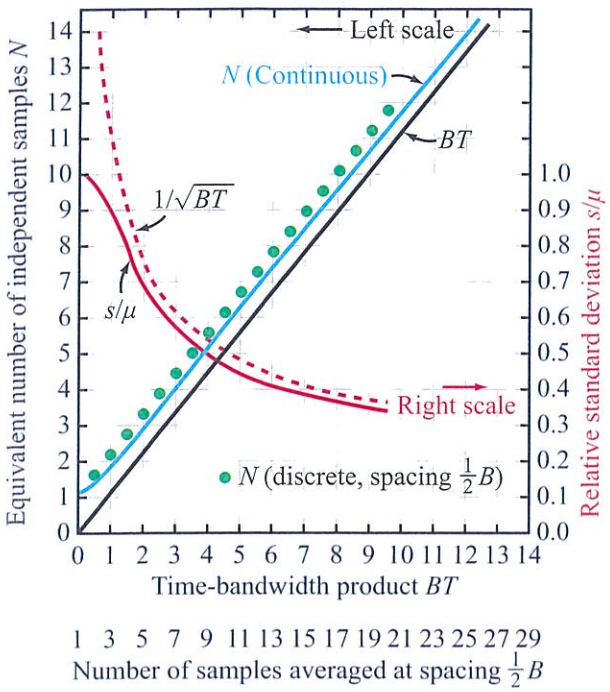

Figure 13-22: Equivalent number N of independent samples and normalized standard deviation as a function of time-bandwidth (BT) product.

In this case the variance of the sum can be shown to be (Davenport and Root, 1958, p. 80)

$$s_T^2 = \frac{1}{N_p^2}\left\{\sum_{i=1}^{N_p} s_i^2 + 2\sum_{k=1}^{N_p-1}(N_p-k)\,R_{vf}(kT_p)\right\}, \tag{13.103}$$

where s_i^2 is the standard deviation for a single sample, T_p is the time spacing between adjacent samples, and N_p is the total number of signal samples or pulses. Since for a stationary process all the s_i's are the same, we may replace s_i by just s. The signal correlation coefficients $\rho_{vf}(n)$ are then

$$\rho_{vf}(kT_p) = \frac{R_{vf}(kT_p)}{s^2}. \tag{13.104}$$

Substituting this value into Eq. (13.103) yields

$$s_T^2 = \frac{s^2}{N_p^2}\left\{N_p + 2\sum_{k=1}^{N_p-1}(N_p-k)\,\rho_{vf}(kT_p)\right\}. \tag{13.105}$$

Since the effective number of independent samples N is just the ratio of the variance for one sample to the variance of N_p samples for measurement over a time interval $T = N_pT_p$, it is given by

$$N = \frac{s^2}{s_T^2} = \frac{N_p}{1 + 2\sum_{k=1}^{N_p-1}(N_p-k)\,\rho_{vf}(kT_p)}. \tag{13.106}$$

Since the second term in the denominator is always positive, the maximum value of N is obtained when this term is zero. For the rectangular-spectrum signal, this happens when

$$T_p = 1/B,\ 2/B,\ 3/B,\ldots$$

because in this case

$$\rho_{vf}(kT_p) = 0$$

for all k, because

$$\sin k\pi BT_p = 0.$$

Then, for this case we have

$$N = N_p = BT + 1.$$

For any spacing except a multiple of $1/B$, the second term in the denominator of Eq. (13.106) is positive and N is less than the value given above. For example, consider a spacing of one-half the reciprocal of the bandwidth, that is,

$$T_p = \frac{1}{2B}.$$

The variance for different values of N_p is plotted in Fig. 13-22 as points. It is interesting to note that the number of independent samples obtained this way is larger than that obtained by continuous integration, also shown on the graph. For the larger values

of N_p, the discrete sum variance is about 0.3 larger than the continuous-integration equivalent number of independent samples and about 0.9 larger than BT.

This is an interesting result, since it shows that the variance may be reduced better by taking samples at a spacing between $1/2B$ and $1/B$ than by taking samples closer together, which would approach the continuous case. Numerical calculation for samples at smaller spacing substantiates this; there is no particular advantage, and in fact some small disadvantage, if the PRF of the radar is made higher than $1/B$. For radiometers this never turns out to be a problem, because the time-bandwidth product is invariably very large.

13-8.2 Radiometric Precision

For radiometers, the radiometric precision is quantified by ΔT, the standard deviation of the brightness-temperature measurement. How do we best quantify the power measurement accuracy of a radar?

> ► The primary goal of a scatterometer is to make an accurate measurement of the signal amplitude or power. This need not require a high signal-to-noise ratio. ◄

Note that radiometers operate with a signal-to-noise ratio that may be much less than unity since the desired component of the radiometric signal is only a small part of the total received signal due to thermal noise added in the receiver and other parts of the signal path. Radiometers overcome the low signal-to-noise ratio by averaging large numbers of independent samples. This can be done for radar as well, which reduces the noise variance, but what about the signal variance?

We again note that when the target geometry remains fixed with respect to the radar (so there is no range variation and no Doppler shift), the radar obtains only a single look and no amount of averaging can reduce the signal variance because all of the samples are identical. Hence, averaging only reduces the noise variance. As previously noted, with multiple targets and changing range and/or Doppler, the signal varies with time (fading). In this case, averaging the signal in time can reduce the signal variance and thereby reduce the variance of estimates of the surface backscatter as well as reducing the noise variance.

A very useful approach to recording radar measurements of the signal power in the presence of noise is to make separate measurements of the radar signal power and the noise power. The latter can be collected by not transmitting pulses at some times, or by making power measurements over bandwidths outside of the radar echo bandwidth. Assuming the radar signal and the noise signal are independent, the mean value of the received power $\overline{P_r}$ is the sum of the mean values of the signal and the noise power because the signal and noise cross-terms average out. Thus we can write

$$\overline{P_r} = \overline{P_s} + \overline{P_n}, \tag{13.107}$$

where $\overline{P_s}$ is the mean signal power and $\overline{P_n}$ is the mean power of the noise. The received mean power can be expressed in terms of the mean signal power and the ***signal-to-noise ratio*** S_n as

$$\overline{P_r} = \overline{P_s}\left(1 + \frac{\overline{P_n}}{\overline{P_s}}\right) = \overline{P_s}\left(1 + \frac{1}{S_n}\right), \tag{13.108}$$

where

$$S_n = \frac{\overline{P_s}}{\overline{P_n}}. \tag{13.109}$$

As given in Section 5-7.3, if the receiver uses a square-law detector to measure the signal power, the standard deviation s_r of the signal without averaging (1 independent sample) is proportional to the mean and can be expressed as

$$s_r = \overline{P_r} = \overline{P_s}\left(1 + \frac{1}{S_n}\right). \tag{13.110}$$

$(N_r = 1)$

When N_r independent samples of the received signal are averaged, the standard deviation s_{rN_r} for the average is given by

$$s_{rN_r} = \frac{\overline{P_s}}{\sqrt{N_r}}\left(1 + \frac{1}{S_n}\right). \tag{13.111}$$

$(N_r \geq 1)$

The estimate of the received signal power is obtained by taking the difference between the estimate of the combination of signal-and-noise $\hat{\overline{P}}_r$ and the estimate of the noise alone $\hat{\overline{P}}_n$:

$$\hat{\overline{P}}_s = \hat{\overline{P}}_r - \hat{\overline{P}}_n, \tag{13.112}$$

where the $\hat{}$ denotes an estimate. The estimate of the noise is obtained by averaging a set of N_n samples of the noise from separate measurements of the noise. The variance $s^2_{nN_n}$ of this noise estimate is

$$s^2_{nN_n} = \frac{\overline{P}_n}{\sqrt{N_n}}. \tag{13.113}$$

The variance for either the sum or the difference of two independent random variables is the sum of the variances of the individual components; hence the variance for the signal estimate is the sum of the variances of the two measurements, namely the signal-plus-noise and noise-only powers, i.e.,

$$s_s^2 = s^2_{rN_r} + s^2_{nN_n} = \frac{\overline{P}_s^2}{N_r}\left(1+\frac{1}{S_n}\right)^2 + \frac{\overline{P}_n^2}{N_n}. \tag{13.114}$$

Using

$$\overline{P}_n = \overline{P}_s\left(\frac{\overline{P}_n}{\overline{P}_s}\right) = \frac{\overline{P}_s}{S_n}, \tag{13.115}$$

Eq. (13.114) becomes

$$s_s^2 = \frac{\overline{P}_s^2}{N_r}\left(1+\frac{1}{S_n}\right)^2 + \frac{\overline{P}_s^2}{N_n}\left(\frac{1}{S_n}\right)^2. \tag{13.116}$$

The ***normalized standard deviation***, K_p, of the estimate of the signal power is then

$$K_p = \frac{s_s}{\overline{P}_s} = \sqrt{\frac{1}{N_r}\left(1+\frac{1}{S_n}\right)^2 + \frac{1}{N_n}\left(\frac{1}{S_n}\right)^2}. \tag{13.117}$$

When the signal and noise estimates use the same number of samples, Eq. (13.117) simplifies to

$$K_p = \frac{1}{\sqrt{N_r}}\sqrt{\left(1+\frac{1}{S_n}\right)^2 + \left(\frac{1}{S_n}\right)^2}. \tag{13.118}$$

Note that K_p is a function of both the signal-to-noise ratio of the measurements and the number of pulses used, which enables a trade-off between the number of pulses, the signal time-bandwidth product, and the signal-to-noise ratio. It may be easier to increase the number of independent looks by improving the signal time-bandwidth product than to increase the signal-to-noise ratio in a particular design. A general approach to computing K_p when filtering and detection are intermixed is given by Yoho and Long (2004).

Radiometers can obtain separate signal and noise measurements by alternately measuring (1) the output of a calibrated noise source of known temperature, combined with the noise in the receiver, and (2) the output of the antenna, also combined with the noise in the receiver. By suitable comparison of these, the effect of the receiver noise is calibrated out with a precision comparable to that indicated by Eq. (13.117). In some radar scatterometers used for oceanographic wind observation, noise measurements are obtained by skipping some transmit pulses. The resulting noise-measurement periods are interleaved with the measurements of the signal and noise.

As an example of the type of standard deviation that may be obtained with different signal-to-noise ratios for radar, consider a radar time-bandwidth product of 100, which means $N_r \approx 100$. If $S_n = 1$, the relative standard deviation is $K_p = \sqrt{5/100} = 0.22$. If $S_n = 10$, the normalized standard deviation is reduced by a factor of two to 0.11, and if S_n approaches infinity the normalized standard deviation (now due to fading alone) is 0.10. Therefore, almost no advantage is gained in having a signal-to-noise ratio exceeding ~10, and relatively little advantage is obtained in having it much greater than unity. However, increasing the time-bandwidth product (or, equivalently, the number of independent looks) by 100 reduces the relative standard deviation at $S_n = 1$ from 2.2 to 0.22.

Consider, for example, a passive system such as a radio telescope with a bandwidth $B = 10^8$ Hz and an observation time $T = 100$ s. The equivalent number of independent samples is $N_r = BT = 10^{10}$. For unity signal-to-noise ratio, the relative standard deviation is $\sqrt{5/10^{10}} = 2.2 \times 10^{-5}$. For a much weaker signal-to-

noise ratio, say $S_n = 0.001$, the normalized standard deviation is 1.4×10^{-2}, which still provides quite a precise measurement.

13-9 Ambiguities in Radar

Ambiguities can exist with pulse radars for both range and speed measurements. For pulse radars the ambiguity is often associated with the pulse repetition frequency (PRF) f_p.

13-9.1 Range Ambiguity

> ▶ Ambiguity in range measurement occurs at high PRF when the echo from a more-distant target appears to be the echo from a nearer target. ◀

Figure 13-23 illustrates the problem graphically by showing ambiguous range returns resulting from transmitting pulses too close together; i.e., the PRF f_p is too high. The transmitted pulses are shown at the top of the figure, and the next three lines illustrate returns associated with the first transmitted pulse for each of three targets whose spacings are such that the range delay is T_1 from the start of the first pulse for target 1, $T_1 + T_p$ for target 2 and $T_1 + 2T_p$ for target 3, where T_p is the pulse period. That is, $T_p = 1/f_p$. The first "return" line is for target 1 at a range corresponding to T_1; the second return line is for target 2 at a range corresponding to $T_p + T_1$, which places it just T_1 after the start of the second pulse. The third return line contains a comparable return that arrives a time T_1 after the start of the transmission of the third pulse. On the display all of these pulses appear together. That is, on the fifth line the return from target 1 appears at a time T_1 after the transmission of the first pulse. The returns from both target 1 and target 2 appear at a time T_1 after transmission of the second pulse, and the returns from all three targets are superimposed after the time of transmission of the third pulse and from then on. In the usual display, which shows the returns only for one interpulse period, as indicated in the sixth line, one

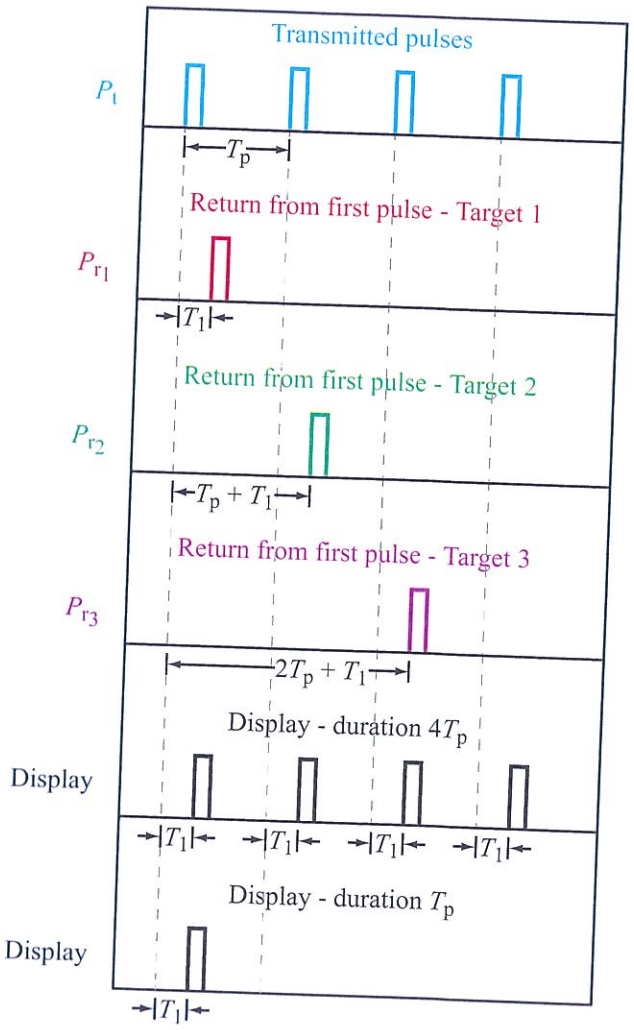

Figure 13-23: Ambiguous range returns.

cannot tell whether there are one, two, three, or even more targets present, and one cannot establish the range to the farther targets because one does not know which pulse caused the return. Thus, if the maximum range of the radar is the range to the third target, the pulse repetition period should be $4T_p$ or thereabouts, to assure that this ambiguity in interpretation of the returns does not exist. Increasing T_p results in a lower PRF, but this may be inconsistent with the requirement for a high

enough PRF to meet Nyquist sampling requirements for the Doppler frequency.

13-9.2 Speed Ambiguity

► Ambiguity in speed measurement occurs when the sampling rate (PRF) is too low to satisfy the Nyquist sampling criterion, resulting in aliasing. ◄

When a single Doppler frequency is received, that is, when a single target is observed, one can see the ambiguity problem associated with the Nyquist sampling theorem by considering the waveforms in Fig. 13-24. In the second line, a single Doppler-frequency return is shown sampled at the Nyquist rate by the pulses transmitted in accordance with the first line. In the third line, however, a Doppler frequency three times that of the second line, that is, a Doppler frequency corresponding to a speed three times that associated with the first line, is shown, and the samples are identical with those for the second line; thus there is an ambiguity in the frequency of the waveform. One cannot tell from the samples whether the Doppler frequency is associated with the speed u_1 or with any odd multiple of u_1. If we are to avoid this ambiguity, and the maximum Doppler frequency is that shown in the third line, we must sample three times as often. That is, we must have a PRF three times that illustrated in the figure.

One way to resolve the ambiguities is illustrated in Fig. 13-25. Here the transmitted pulses are not emitted at a constant interpulse period. Rather, their spacing is ***jittered*** about a rate that allows adequate Doppler sampling, but would normally give range ambiguities. Note that a strong return occurs when all the pulses at appropriate delays are added together, but the other pulses appear to come from weaker targets at incorrect ranges. Unfortunately, with this type of system, the extra returns provide spurious artifacts and ***clutter***, which may or may not be tolerable, depending upon other system considerations.

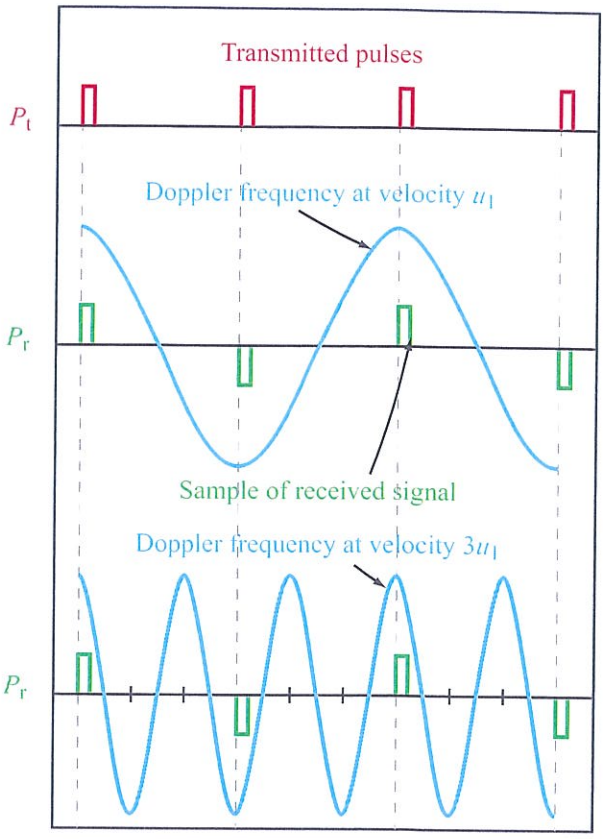

Figure 13-24: Ambiguous Doppler returns when sampling at the Nyquist rate.

13-9.3 Radar Ambiguity Function

► Ambiguity in timing or range measurement occurs when the PRF is too high so that the signal from a previous pulse appears during the expected return of the desired signal echo. ◄

Single-pulse ambiguity

The simple cases treated thus far illustrate the importance of Doppler and timing ambiguity in radar. Ambiguity also arises due to mismatch between the received signal and the reference matched filter used to process the signal. Choosing the appropriate transmit

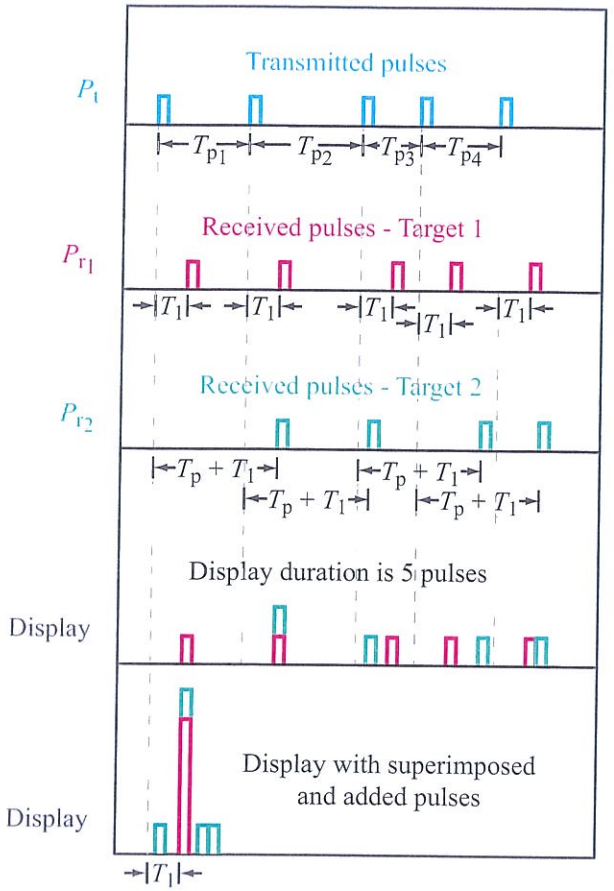

Figure 13-25: Reduction of ambiguous range returns by jittered pulse intervals.

waveform, PRF, and matched filter helps minimize ambiguity. A useful tool for this purpose is the ***radar ambiguity function***, which is derived from the matched filter for a single pulse, but which can also be used for analyzing coherent processing of multiple pulses. The ambiguity function is particularly useful for analyzing the properties of the system when different waveforms are used; however, a detailed study of waveform design is beyond the scope of this book, but is treated in other texts (e.g., Skolnik, 1980; Richards et al., 2010). In the following we illustrate the radar ambiguity function for several waveforms.

Consider the complex transmit function

$$v_t(t) = u(t)\, e^{j2\pi f_c t} \tag{13.119}$$

where $u(t)$ is the baseband complex modulated transmit waveform and f_c is the carrier frequency. Ignoring the amplitude and removing the carrier, the expected received signal is a time-delayed, Doppler-shifted replica of the of transmit signal and is given by

$$v_R(t) = u(t-\tau')\, e^{j2\pi f'_D(t-\tau')}, \tag{13.120}$$

where τ' is the time delay due to the time of flight and f'_D is the Doppler shift.

The matched filter output $y(t)$ is the convolution of the received signal with the filter impulse response given by the time-reversed complex conjugate of the reference signal $v_{REF}(t)$,

$$y(t) = \int_{-\infty}^{\infty} v_R(t')\, v^*_{REF}(t'-t)\, dt'. \tag{13.121}$$

In the ideal case, the reference function is $v_{REF}(t) = v_R(t)$ so that the matched filter output is

$$\begin{aligned} y(t) &= \int_{-\infty}^{\infty} u(t'-\tau')\, u^*(t'-t-\tau') \\ &\quad \cdot e^{j2\pi f'_D(t'-\tau')} e^{-j2\pi f'_D(t'-t-\tau')}\, dt' \\ &= e^{j2\pi f'_D t} \int_{-\infty}^{\infty} u(t'-\tau')\, u^*(t'-t-\tau')\, dt'. \end{aligned} \tag{13.122}$$

The output of the matched filter at time $t+\tau'$ is obtained by replacing t with $(t+\tau')$ and also t' with $(t'+\tau')$:

$$y(t+\tau') = e^{j2\pi f'_D t(t+\tau')} \int_{-\infty}^{\infty} u(t')\, u^*(t'-t-\tau')\, dt'. \tag{13.123}$$

We recognize the integral as the autocorrelation function of the signal modulation (Richards, 2005).

Let us examine what happens if the wrong reference function is used; i.e., what does the output of the matched filter change to when the filter and signal are mismatched? Suppose the reference function $v_{REF}(t)$ were to use a time delay τ_0 (instead of the time delay τ')

and a Doppler shift f_{D0} (instead of the true Doppler shift f'_D),

$$v_{REF}(t) = u(t-\tau_0)\, e^{j2\pi f_{D0}(t-\tau_0)}. \tag{13.124}$$

The output of the matched filter is then

$$y(t) = \int_{-\infty}^{\infty} u(t'-\tau')\, u^*(t'-t-\tau_0) \cdot e^{j2\pi f'_D(t'-\tau')} e^{-j2\pi f_{D0}(t'-t-\tau_0)}\, dt'. \tag{13.125}$$

Using the substitutions $t'' = t' - \tau'$, $\tau = \tau' - \tau_0$, and $f_D = f'_D - f_{D0}$, the matched filter output can be written as

$$y(t) = e^{j2\pi f_{D0}(t-\tau)} \int_{-\infty}^{\infty} u(t'')\, u^*(t''-t+\tau)\, e^{j2\pi f_D t''}\, dt''. \tag{13.126}$$

The output of the matched filter at time $t+\tau$ is thus

$$y(t+\tau) = e^{j2\pi f_{D0} t} \int_{-\infty}^{\infty} u(t'')\, u^*(t''-t)\, e^{j2\pi f_D t''}\, dt'', \tag{13.127}$$

which is similar in form to Eq. (13.123) but with Doppler frequency terms.

Note that now $\tau = \tau' - \tau_0$ is the ***error in the time delay*** between the actual delay and the time delay assumed in the reference function, and $f_D = f'_D - f_{D0}$ is the ***error in the Doppler shift*** between the received signal and the reference function. The magnitude of the matched filter output is maximized when the received and reference signals match, which occurs when $\tau = 0$ and $f_D = 0$, and falls off when they are mismatched. Thus, the magnitude of the matched filter output can be used to evaluate how well matched the received signal and the matched filter reference signal are.

To assist in this evaluation we define the generalized radar ambiguity function as

$$\chi(\tau, f_D) = \left| \int_{-\infty}^{\infty} u(t)\, u^*(t-\tau)\, e^{-j2\pi f_D t}\, dt \right|^2 \tag{13.128}$$

or

$$\chi(\tau, f_D) = \left| \int_{-\infty}^{\infty} \mathbf{U}^*(f-f_c)\, \mathbf{U}(f-f_c-f_D)\, e^{-j2\pi f\tau}\, df \right|^2. \tag{13.129}$$

where $\mathbf{U}(f)$ is the Fourier transform of $u(t)$. Some authors do not include the square in the definition of χ. Note that $\chi(0,0)$ corresponds to the total signal energy and that

$$\chi^2(\tau, f_D) \le \chi(0,0). \tag{13.130}$$

The radar ambiguity function can be viewed as the convolution of the Doppler-shifted echo with a filter matched to an unshifted echo. *The variables f_D and τ describe the mismatch in Doppler and time delay, respectively,* between the actual signal and the signal that the matched filter is designed for. At $f_D = 0$ and $\tau = 0$ the signal and filter are matched, which produces the highest signal-to-noise ratio. Signal and filter mismatch reduces the signal-to-noise ratio primarily by reducing the signal output power.

Figure 13-26(a)–(c) illustrates the ambiguity function for several single-pulse modulation schemes, including a simple pulse, an LFM-pulse, and a binary phase-modulated pulse. Fig. 13-26(a) illustrates the ambiguity function for an ICW pulse. Note that for zero Doppler ($f_D = 0$) in Eq. (13.128), the ambiguity function has the form of the autocorrelation of the pulse. For an ICW pulse, this is triangular as derived in Eq. (13.74). If the time delay $\tau = 0$, the ambiguity function is a $|(\sin x)/x|^2$ function. A corresponding diagram of the region for which the ambiguity diagram for an ICW pulse exceeds the 1/2 power point is shown in Fig. 13-26(d). Everything within the red ellipse is essentially ambiguous; i.e., there is not enough information to "resolve" the signal any finer. Thus, this region defines the effective resolution in time delay and Doppler for a single pulse. The indicated size corresponds to the effective temporal and Doppler resolution of the pulse previously derived. Computation of the ambiguity function is thus an effective way of determining the temporal and frequency resolution of a particular transmit signal or pulse modulation scheme.

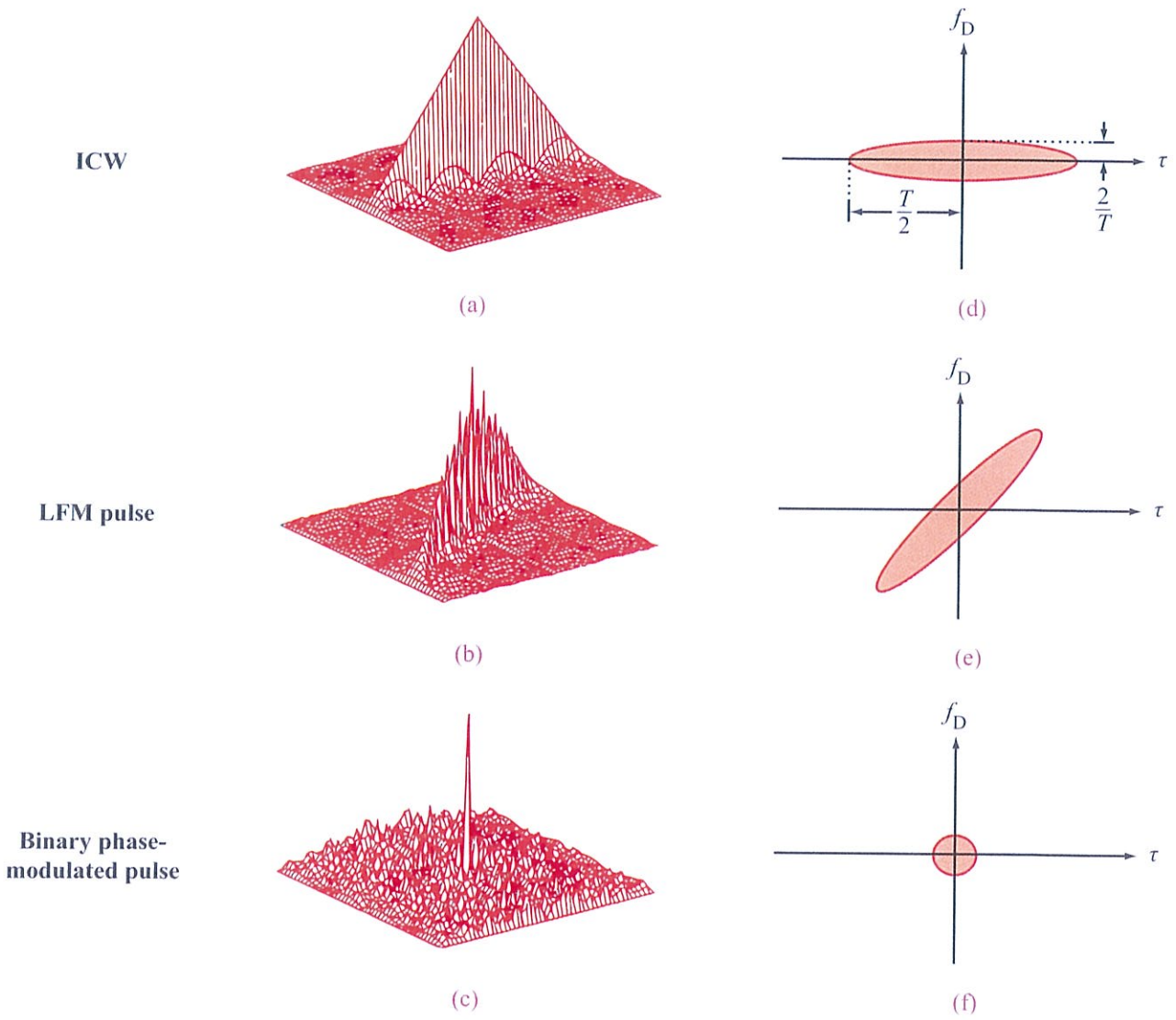

Figure 13-26: Examples of single-pulse ambiguity functions: (a) rectangular ICW pulse, (b) LFM pulse, (c) binary phase-modulated pulse and diagrams of their 1/2-power regions in time-Doppler space.

For the LFM pulse shown in Fig. 13-26(b) and (e), the "blade-like" shape of the ICW pulse is rotated at an angle. This couples the Doppler and range ambiguity. The LFM and ICW pulse shapes have very low "floors" off the side of the main peak. This means that the area resolved by the pulse is nicely isolated from the surrounding area and that strong signal returns from outside the resolved area have less impact on the measured power.

The ambiguity function shown in Fig. 13-26(c) and (f) for the binary phase-modulated pulse has the smallest central peak, and therefore potentially the finest resolution of the ambiguity functions shown. However, the ratio of the height of the central peak

to the surrounding "floor" is much lower than for the other modulation schemes, which suggests that this modulation scheme is more susceptible to interference from strong signals near the desired resolution element. It can be shown that the total squared ambiguity function is fixed no matter what the shape of the modulation; i.e.,

$$\iint \chi^2(\tau, f_D)\, d\tau\, df_D = \chi^2(0,0). \tag{13.131}$$

Thus, as the peak is narrowed by changing the pulse modulation the floor comes up to compensate. The ambiguity function is a useful tool for evaluating the sensitivity of the resolution element to the surrounding area.

Multiple-pulse ambiguity

The ambiguity function can be computed by coherently combining multiple pulses. Figure 13-27 illustrates the ambiguity function for a train of N pulses of length T and pulse repetition interval T_0. The total duration of the pulse train is NT_0. The plot illustrates numerous spikes of various heights (the height is suggested by the diameter of the circles). These correspond to possible time and frequency ambiguities. Combinations of delay and Doppler frequency that correspond to one of the spikes can be confused (i.e., they are ambiguous) with one another. Note that the peaks along the horizontal time axis are at the pulse spacing T_0, which give the ambiguities in range. Along the frequency axis the peaks are spaced $1/T_0$ apart. These are the ambiguities between the different Doppler frequencies associated with the sampling that occurs during pulsed operation. The width of the individual spikes in the Doppler domain is proportional to the reciprocal of the duration of the burst of pulses. By combining multiple pulses, the individual spikes are narrower, which yields higher resolution, but the existence of multiple spikes indicates multiple ambiguities. We note that a narrow antenna beam could resolve the ambiguities in Fig. 13-27 if the mainlobe illuminates only the area corresponding to one of the peaks.

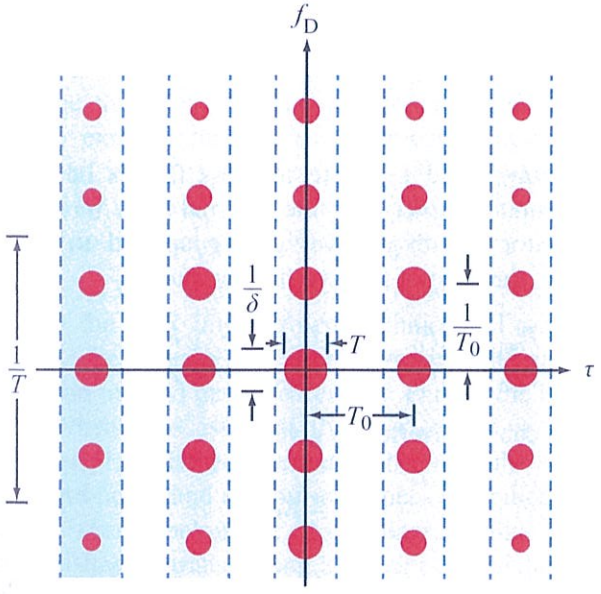

Figure 13-27: Ambiguity diagram for multiple pulses.

The subject of ambiguity functions is quite complex, and a detailed study of the different waveforms is beyond the scope of this book. Waveform design has been the subject of many papers and books or chapters in books on radar signals. For a more complete analysis, the reader is referred to Cook and Bernfield (1967), DiFranco and Rubin (1968), Berkowitz (1965), Skolnik (1980), and Richards et al. (2010).

13-10 Radar Calibration

▶ Internal calibration of a scatterometer system permits determination of *relative* scattering coefficients (or scattering amplitude S if the scatterometer is polarimetric), whereas external calibration permits absolute determination of the scattering coefficient σ^0 or the scattering amplitude S. ◀

13-10.1 Internal Calibration

Two different methods for internal calibration can be used—the method of independent or separate calibrations of different parts of the system, and the ***ratio method***, in which a sample of the transmitted signal is

passed through the receiver and data-handling system. The latter is definitely a superior approach, because there is less chance for error and it may be conducted at very frequent intervals, whereas separate calibrations require interrupting the measurement series to a much greater degree. Furthermore, the calibration of each part separately results in many errors that can add up to decrease the precision of the overall calibration.

Recall from Eq. (5.37) that the scattering coefficient σ^0 of a distributed target is directly proportional to the received-to-transmitted power ratio, P^r/P^t. That is,

$$\sigma^0 = \left[\frac{P^r}{P^t}\right]\left[\frac{(4\pi)^3 R_0^4}{\lambda^2 G_0^2 A}\right]. \tag{13.132}$$

Internal calibration allows us to measure (P^r/P^t), which includes all system gains and losses except for the antenna gain G_0.

The general concept of the ratio calibration method is illustrated by Fig. 13-28. A directional coupler is shown in the line from the transmitter to the antenna, and another in the line from the antenna to the receiver. Between the two is a path of known attenuation L_c so that a sample of the transmitter signal may be fed through to the receiver. Depending on the type of radar system, this may be done continuously or on an alternating basis, with the receiver sometimes connected to the incoming signal from the external target and sometimes connected to the calibration signal. In Fig. 13-28, the transmitter power at the antenna is P^t, and at the directional coupler, it is

$$P_0^t = L_t P^t, \tag{13.133}$$

where L_t is the loss factor of the transmitter directional coupler. The received power at the receiver directional coupler is either

$$P_0^r = \frac{P^r}{L_r}, \quad \textbf{during target reception} \quad \text{(both switches in Position 1)} \tag{13.134a}$$

or

$$P_0^c = \frac{P_0^t}{L_c L_{DC_t} L_{DC_r}} = \frac{L_t P^t}{L_c L_{DC_t} L_{DC_r}}, \quad \textbf{during calibration} \quad \text{(both switches in Position 2)} \tag{13.134b}$$

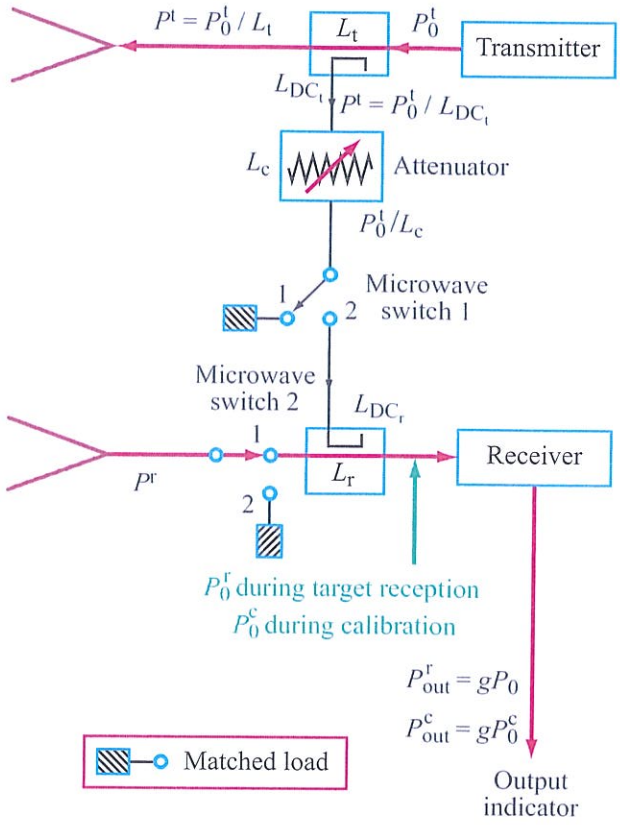

Figure 13-28: Ratio calibration technique. Switches 1 and 2 are synchronized.

where L_{DC_t} and L_{DC_r} are the loss factors of the two directional couplers for the internal path through the attenuator. With receiver gain g applied to both P_0^r and P_0^c, the ratio of the two final outputs is

$$\frac{P_{out}^r}{P_{out}^c} = \frac{gP_0^r}{gP_0^c} = \left(\frac{L_c L_{DC_t} L_{DC_r}}{L_r L_t}\right)\frac{P^r}{P^t}, \tag{13.135}$$

which can be inverted to give

$$\frac{P^r}{P^t} = K_s \frac{P_{out}^r}{P_{out}^c}, \tag{13.136}$$

where K_s is an ***overall calibration constant*** given by

$$K_s = \frac{L_r L_t}{L_c L_{DC_t} L_{DC_r}}. \tag{13.137}$$

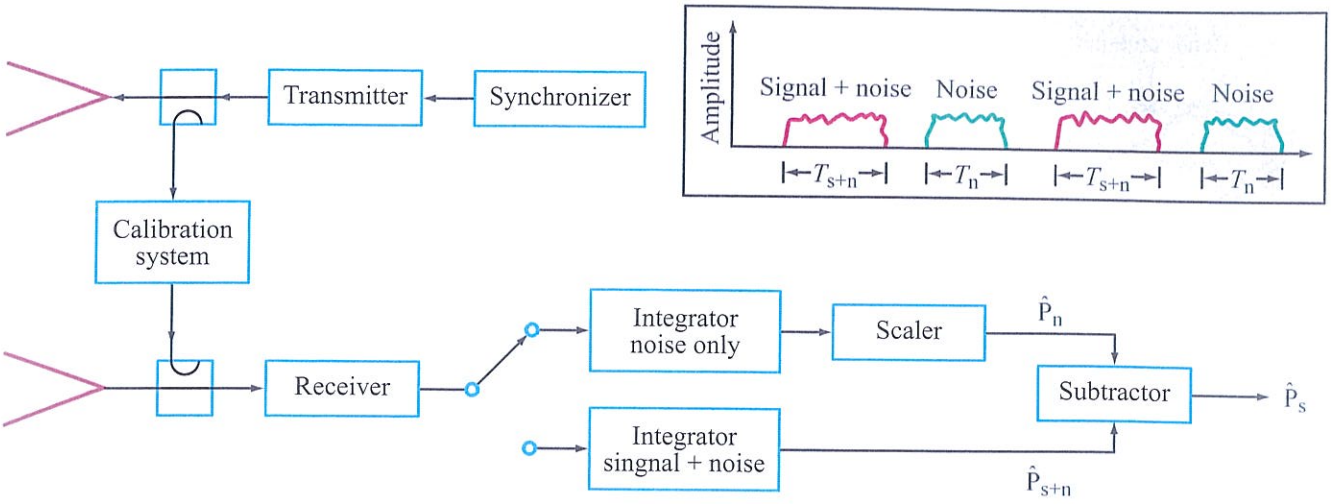

Figure 13-29: Noise measurements to allow radars to measure σ^0 at low SNRs.

Radars can be made very sensitive by using the same technique that is applied in radiometers. In most radiometer receivers, alternate measurements are made of the external scene viewed by the antenna beam and of a reference noise source. As discussed in Section 13-8, upon subtraction of the two measurements and then integrating the difference signal, much of the receiver noise is eliminated. When the concept is applied to a radar, the first measurement corresponds to the return from an external target plus the receiver noise, and the second signal is receiver noise alone. Subtraction followed by integration leads to significant improvement in signal-to-noise ratio (SNR) and K_p.

Figure 13-29 illustrates a switched system for realizing the SNR improvement technique. From time to time, the system is calibrated using the internal calibration method described earlier. During the interim period when it is assumed that the system is stable, the system is switched alternately between the sum of signal-and-noise and the noise alone. As indicated in the time sketch below the block diagram, this can be accomplished by transmitting a signal of finite duration, integrating the value received from this signal, and then integrating the noise during a waiting period before the receipt of the next signal. Since, as indicated in the sketch, the integration times for noise and the sum of signal-and-noise may be different, a scaler is required for one of the signals before they are subtracted to obtain the estimate of the signal alone. This type of system has been widely used in wind scatterometer systems. In the case of the Seasat scatterometer a precision of about 5 percent in the measurement was achieved with a signal-to-noise ratio of the order of -10 dB (Johnson et al., 1980).

13-10.2 External Calibration

The degree of success of the internal calibration techniques discussed in the preceding subsection depends in part upon the accuracy with which the antenna gain pattern and other system functions are known. It is often desirable to calibrate a radar imager or scatterometer by measuring the return power from a target of known radar cross section. Figure 13-30 illustrates calibration arrangements for ground-based and airborne scatterometers using a "hard" target (such as a corner reflector) to provide the necessary calibration level. As shown later, measurement precision is determined by the magnitude of the radar cross section of the calibration target relative to the radar cross section of the

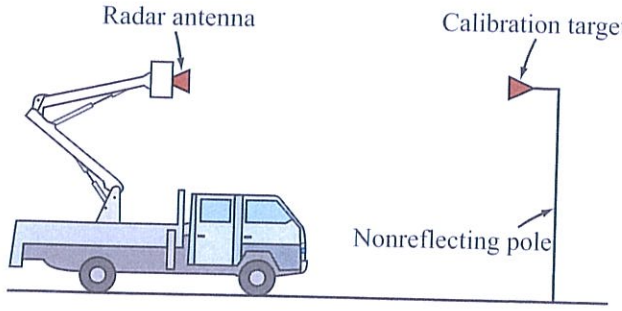

(a) Calibration of truck-mounted radar

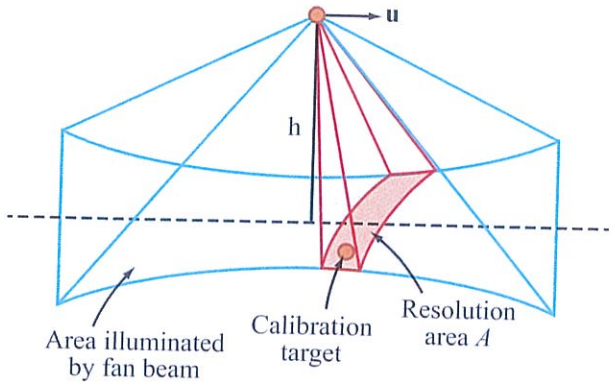

(b) Calibration of fan-beam Doppler scatterometer

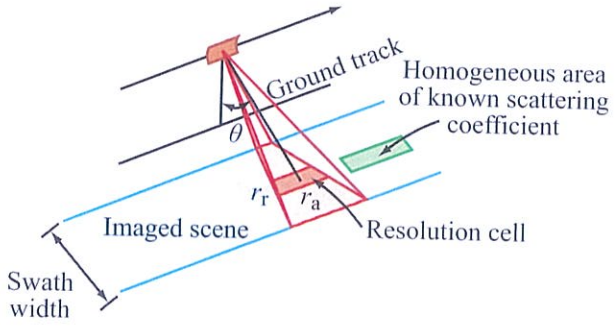

(c) Use of a homogeneous area of known scattering coefficient to calibrate an imaging radar

Figure 13-30: Configurations for calibrating (a) a ground-based (truck- or tower-mounted) scatterometer and (b) an airborne scatterometer or imager (here a fan-beam Doppler scatterometer) using a manmade calibration target, or (c) using a natural surface of known scattering properties.

background; in the case of Fig. 13-30(b), the background is the resolution area A. Alternatively, a "homogeneous" extended target of known scattering coefficient $\sigma^0(\theta)$ may be used [Fig. 13-30(c)]. This latter approach is particularly attractive for airborne and spaceborne systems because the background is itself the calibration target. Thus, the need for hard targets with large radar cross sections is avoided. The azimuth and range dimensions of the extended target should be much larger than the corresponding spatial resolutions of the radar, so that sufficient averaging can be performed to reduce the effects of signal fading. Ideally, the extended target should have a time-invariant scattering behavior (i.e., its dielectric properties and surface roughness remain constant over an extended period of time), and its $\sigma^0(\theta)$ should be a smooth, slowly varying function of θ over the angular range of the antenna elevation beamwidth (range direction). An example of an extended target is a concrete airport runway; its dimensions are suitable for a high-resolution imaging radar and its surface scattering characteristics remain essentially constant with time, as long as it remains dry. The major drawback of the (electromagnetically) smooth concrete surface, however, is that its scattering coefficient $\sigma^0(\theta)$ exhibits a strong dependence on θ, which means that the calibration accuracy becomes critically dependent on the accuracy with which θ can be determined and on the accuracy of $\sigma^0(\theta)$. It is assumed that $\sigma^0(\theta)$ is measured by a calibrated, truck-mounted or airborne scatterometer. A more suitable calibration surface is an artificially prepared or naturally existing, relatively flat, rough surface located in an arid region. If the dimensions of the extended target are on the order of kilometers, an airborne imaging radar may be calibrated over several segments of its full angular range (in elevation) by flying the system several times so that the extended target is positioned at different ranges within the image swath width. For a spaceborne scatterometer or modest-resolution imager, the Amazon rain forest is the most homogeneous such target (Johnson et al., 1980; Kennett and Li, 1989; Long and Skouson, 1996; Tsai et al., 1999), and its σ^0 is more nearly independent of θ than that of a desert target.

13-10.3 Measurement Precision

When a calibration target of radar cross section σ_c is illuminated by a radar antenna, the backscattered electric field at the receiver is a combination of the desired field from the calibration target and the fields scattered by the background. Thus, in terms of the polarization components of those fields that are parallel to the polarization vector of the receiving antenna,

$$\mathbf{E}_m = \mathbf{E}_c + \mathbf{E}_b = \mathbf{E}_c \left[1 + \frac{\mathbf{E}_b}{\mathbf{E}_c}\right] = \mathbf{E}_c \left[1 + \left|\frac{\mathbf{E}_b}{\mathbf{E}_c}\right| e^{j\phi}\right], \tag{13.138}$$

where $\mathbf{E}_m$, $\mathbf{E}_c$, and $\mathbf{E}_b$ are respectively the receiver (measured) electric field, the electric field due to the calibration target, and the net electric field due to the background, and ϕ is the relative phase angle between $\mathbf{E}_b$ and $\mathbf{E}_c$. The measured radar cross section (RCS) σ_m is proportional to the received power:

$$\begin{aligned}\sigma_m = K|\mathbf{E}_m|^2 &= K|\mathbf{E}_c|^2 \left(1 + \frac{|\mathbf{E}_b|^2}{|\mathbf{E}_c|^2} + 2\left|\frac{\mathbf{E}_b}{\mathbf{E}_c}\right| \cos\phi\right) \\ &= \sigma_c \left(1 + \frac{\sigma_b}{\sigma_c} + 2\sqrt{\frac{\sigma_b}{\sigma_c}} \cos\phi\right),\end{aligned} \tag{13.139}$$

where K is a proportionality constant and σ_c and σ_b are the RCSs of the calibration target and background, respectively. If $\sigma_b \ll \sigma_c$, Eq. (13.139) reduces to $\sigma_m \approx \sigma_c$. In the general case, however, the measured radar cross section may differ from σ_c by a factor equal to the quantity inside the brackets in Eq. (13.139). In a measurement setup, ϕ is an unknown quantity that may take on any value between 0 and π. The corresponding ***calibration error*** falls between the maximum limits given by

$$\frac{\sigma_m - \sigma_c}{\sigma_c} = \frac{\sigma_b}{\sigma_c} \pm 2\sqrt{\frac{\sigma_b}{\sigma_c}} = S_{bc}^2 \pm 2S_{bc}, \tag{13.140}$$

where

$$S_{bc}^2 = \frac{\sigma_b}{\sigma_c} \tag{13.141}$$

is defined as the ***background-to-calibration-target radar-cross-section ratio***. Plots of the upper and lower limits of Eq. (13.140) are shown in Fig. 13-31 as a function of S_{bc}. Alternatively, σ_m and σ_c may be expressed in decibels, in which case the error limits are given by

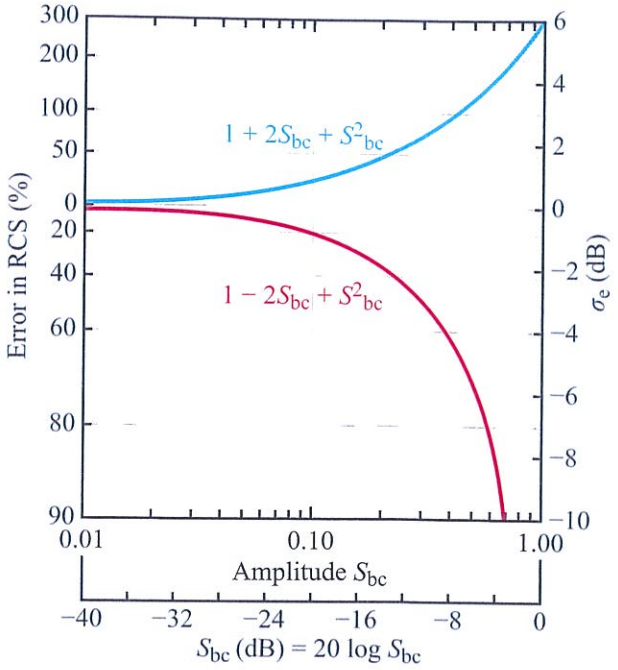

Figure 13-31: Maximum and minimum error bounds (in percent on left-hand scale and in dB on right-hand scale) associated with the measurement of a target with radar cross section σ_c against a background with radar cross section σ_b, plotted as a function of $S_{bc} = \sqrt{\sigma_b/\sigma_c}$ (or $S_b(\text{dB}) = 20\log S_b$) [adapted from Blacksmith et al., 1965].

$$\begin{aligned}\sigma_e(\text{dB}) &= \sigma_m(\text{dB}) - \sigma_c(\text{dB}) \\ &= 10\log(1 + S_{bc}^2 \pm 2S_{bc}).\end{aligned} \tag{13.142}$$

As can be seen from Fig. 13-31, in order to insure that the error is bounded within the ±20 percent interval (±1 dB), we must have $\sigma_b/\sigma_c \leq 10^{-2}$ (= −20 dB). For an airborne radar viewing a ground-resolution cell of area A and average scattering coefficient σ_b^0, in which a calibration target of RCS σ_c is located, the preceding measurement-precision requirement of ±1 dB translates

into

$$A\sigma_b^0 \le \frac{\sigma_c}{100}. \tag{13.143}$$

To illustrate this requirement with an example, consider a (fairly) high-resolution radar system with $A = 100$ m^2, and a bare soil background characterized by a $\sigma_b^0 = 0.1$. According to Eq. (13.143), the calibration target should have an RCS of $\sigma_c \ge 10^3$ m^2, or

$$\sigma_c(\text{dB}) \ge 30 \text{ dBsm},$$

where ***dBsm*** stands for the dB scale referred to a radar cross section of 1 m^2.

Obviously, calibration of ground-based radars [Fig. 13-30(a)] is a much easier task because the calibration target can be positioned at the top of a low-reflectivity structure (such as a pole whose surface is covered with absorbing material), thereby avoiding most of the backscattering from the ground. In that case, the background RCS is much smaller than for the ground-viewing case, and consequently, calibration targets with smaller RCS are required for a given level of measurement precision.

13-11 Passive Calibration Targets

A wide variety of calibration targets may be used in a laboratory environment, but for field operations where high directional accuracies are difficult to achieve, the calibration target should not only have a high RCS, but its RCS should also be insensitive to orientation (relative to the radar) over a wide range of angles. This characteristic may be described in terms of the half-power beamwidths of the RCS directional pattern, as discussed next for individual types of calibration targets. Calibration targets are of two types: (a) passive calibrators and (b) active calibrators. We summarize the properties of both types in this and the following sections.

13-11.1 Flat Rectangular Plate

When viewed from direction (θ, ϕ), the perfectly conducting rectangular plate shown in Fig. 13-32 exhibits a radar cross section $\sigma(\theta, \phi)$ given by Kerr and

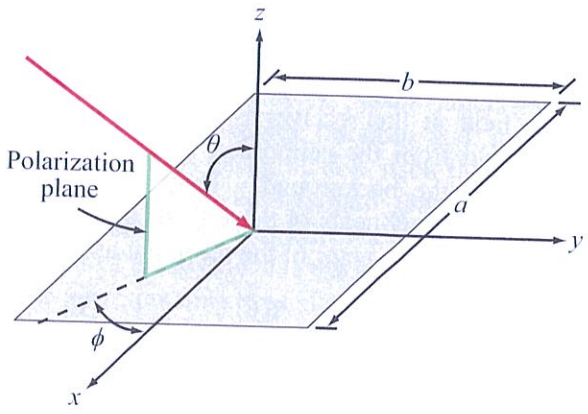

Figure 13-32: Plane of polarization of incident wave.

Goldstein (1951) as

$$\sigma(\theta,\phi) = \frac{4\pi A^2}{\lambda^2}\left[\frac{\sin(ka\sin\theta\cos\phi)}{ka\sin\theta\cos\phi}\,\frac{\sin(kb\sin\theta\sin\phi)}{kb\sin\theta\sin\phi}\right]^2\cos^2\theta, \tag{13.144}$$

where a and b are the plate dimensions, $A = ab$ is its area, and $k = 2\pi/\lambda$. The above expression, which is polarization-independent, is in good agreement with experimental measurements (Fig. 13-33) for θ in the 0–30° range.

The maximum value of $\sigma(\theta, \phi)$ occurs at normal incidence ($\theta = \phi = 0°$) and is given by

$$\sigma_{\max} = \frac{4\pi A^2}{\lambda^2}, \tag{13.145}$$

and the ***half-power beamwidths*** may be computed using the procedure discussed in Section 3-5 for a rectangular antenna,

$$\beta \approx \begin{cases} 0.44\lambda/a & \text{in } xz \text{ plane } (\phi = 0), \\ 0.44\lambda/b & \text{in } yz \text{ plane } (\phi = \pi/2). \end{cases} \tag{13.146}$$

As may be observed from Fig. 13-33, the flat plate has very narrow beamwidths; in this case, $a = b = 16.5$ cm, $\lambda = 3.25$ cm, $\sigma_{\max} = 8.8$ m^2 ($= 9.4$ dBm^2), and $\beta \approx 0.086$ rad ($\approx 5°$).

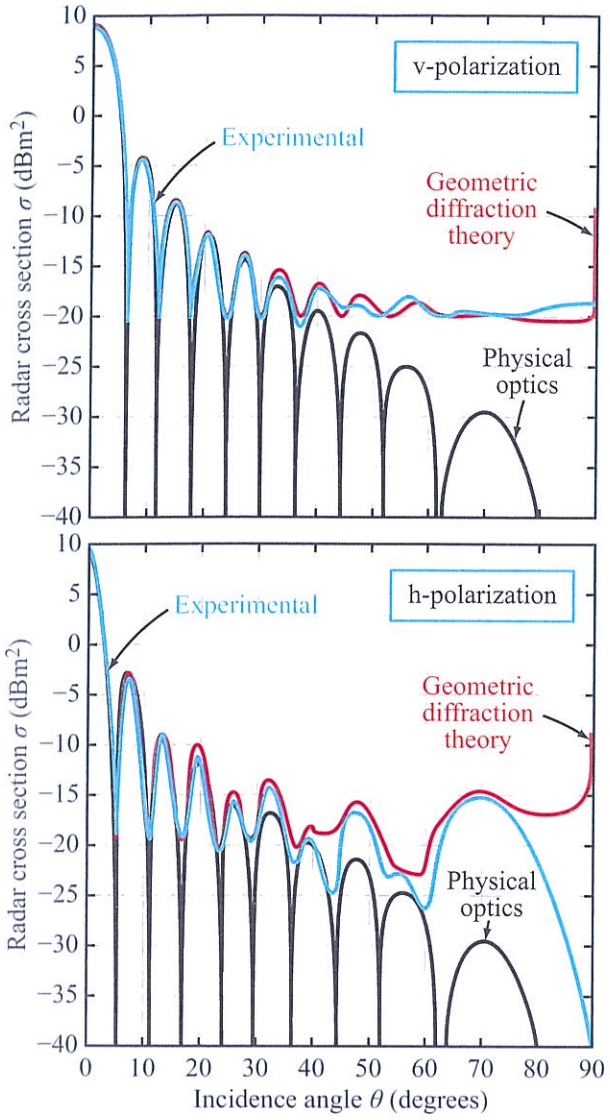

Figure 13-33: Radar cross section of a 16.5 cm by 16.5 cm flat plate at $\lambda = 3.25$ cm [from Ross, 1966].

13-11.2 Flat Circular Plate

The radar cross section of a circular disc of radius r is given by Kerr and Goldstein (1951) as

$$\sigma(\theta) = \frac{4\pi A^2}{\lambda^2}\left[2\,\frac{J_1(2kr\sin\theta)}{2kr\sin\theta}\right]^2 \cos^2\theta, \qquad (13.147)$$

where A is the area of the plate and $J_1(\ )$ is the Bessel function of the first kind. Its maximum RCS σ_{max} is given by Eq. (13.145), and

$$\beta \approx \frac{\lambda}{4r} = \frac{\lambda}{2d}, \qquad (13.148)$$

where d is the disc diameter.

13-11.3 Sphere

Expressions for the backscattering cross section of a sphere are given in Section 8-5, and the frequency dependence of the backscattering efficiency of a metal sphere is plotted in Fig. 8-21. Above the Mie region ($r \geq \lambda$)

$$\sigma \approx A = \pi r^2. \qquad (13.149)$$

The most attractive feature of the metal sphere as a calibration target is the angular symmetry of its radar cross section [σ is independent of the observation direction (θ, ϕ)]. The magnitude of σ, however, is considerably smaller than the maximum radar cross section of a metal plate with the same physical cross section as the sphere. For example, if $r = 2\lambda$ is the radius of a metal sphere and also the radius of a circular metal plate, Eqs. (13.145) and (13.149) lead to

$$\frac{\sigma_{max}(\text{plate})}{\sigma(\text{sphere})} \approx 160 \qquad (r = 2\lambda).$$

13-11.4 Corner Reflector

A ***dihedral corner reflector*** is an assembly consisting of two flat metal plates arranged at right angles to each other, as shown in Fig. 13-34(a). The process of reflection by a dihedral reflector may be considered in terms of ray theory; if a ray enters the corner reflector in a direction that is perpendicular to the line of intersection of the two plates, it experiences a specular reflection by one of the plates towards the other one, then reflects again off the second one, and finally returns in the direction of the transmitting source. This property results in a much wider beamwidth in the horizontal plane (perpendicular to the line of intersection of the two plates) than for a single plate, but has the same narrow-beamwidth limitation in the elevation plane.

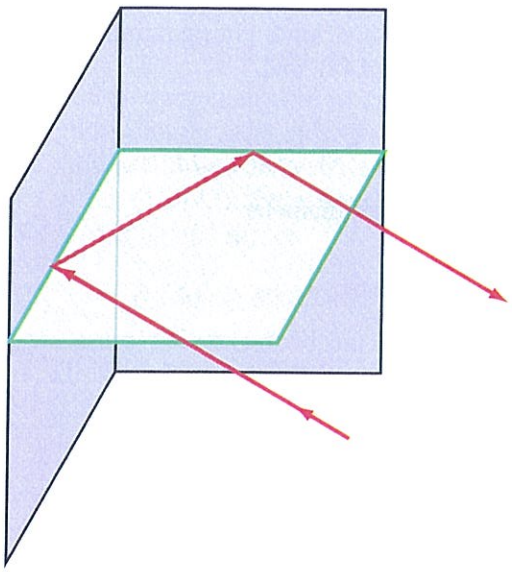

(a) Dihedral corner reflector

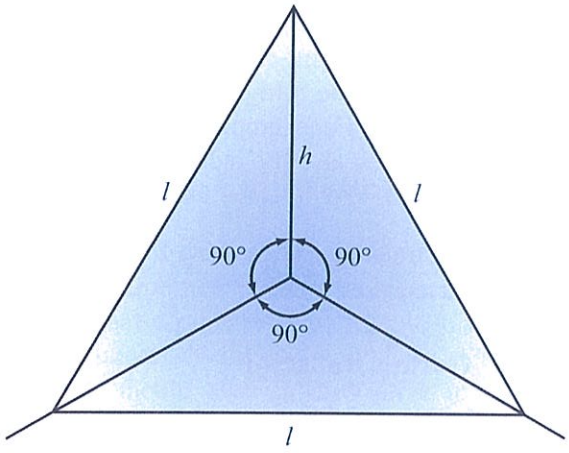

(b) Trihedral corner reflector

Figure 13-34: Dihedral and trihedral corner reflectors.

This restriction may be removed by adding a third plate that is orthogonal to the other two, as shown in Fig. 13-34(b). Such a reflector is called a ***trihedral corner reflector***. The directional variation of the radar cross section of the trihedral corner reflector is described in terms of the angles θ and ϕ, defined as the angles in the elevation and azimuth planes between the axis of symmetry of the reflector and the radar direction.

In Fig. 13-35(a), the plane containing the radar line of sight (line connecting radar to common corner of trihedral reflector) and the intersecting line connecting the reflector corner to point c is called the elevation plane. The reference plane is orthogonal to the elevation plane and contains the radar line of sight. The angle θ is measured between the radar line of sight and the projection of the reflector axis of symmetry onto the reference plane, and ϕ is the angle between the axis of symmetry and its projection onto the reference plane.

The size of the trihedral reflector is defined in terms of the length of its edges, l, or its height $h = l/\sqrt{2}$, as shown in Fig. 13-35(a). One of the attractive features of the trihedral corner reflector is that its RCS has broad patterns in both the azimuth and elevation planes. Examples of experimental measurements made at 9.5 GHz for a trihedral with 45 cm long edges (or equivalently, $h = 10\lambda$) are shown in Fig. 13-35(b) and (c). The half-power beamwidth is on the order of 30° in both planes.

The maximum RCS of the trihedral corner reflector occurs along its axis of symmetry ($\theta = 0$ and $\phi = 0$), and is given by

$$\sigma_{\max} = \frac{4\pi}{\lambda^2} A_{\text{eff}}^2, \tag{13.150}$$

where A_{eff}, the effective area of the trihedral reflector, is related to l and h by

$$A_{\text{eff}} = \frac{l^2}{\sqrt{12}} = \frac{h^2}{\sqrt{3}}. \tag{13.151}$$

Because of the relatively broad beamwidth of its RCS in both the azimuth and elevation planes, the trihedral corner reflector has been the calibration target of choice for many radars, from marine radars used on ships to satellite imaging SARs flown in space. However, the trihedral corner reflector is vulnerable to the possible interaction between the reflector and its ground background. At incidence directions close to boresight, only a portion of each plate contributes to backscattering; for the incident ray to return to the radar,

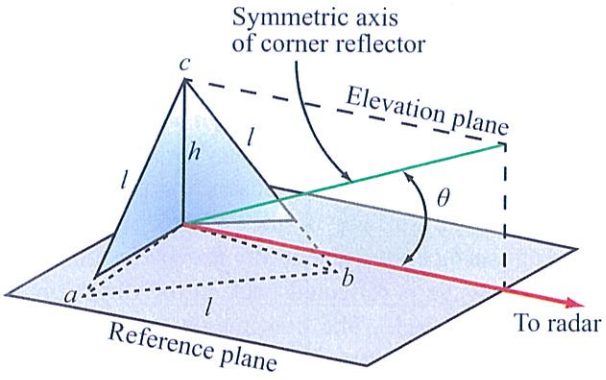

(a) Coordinate system for $\phi = 0$

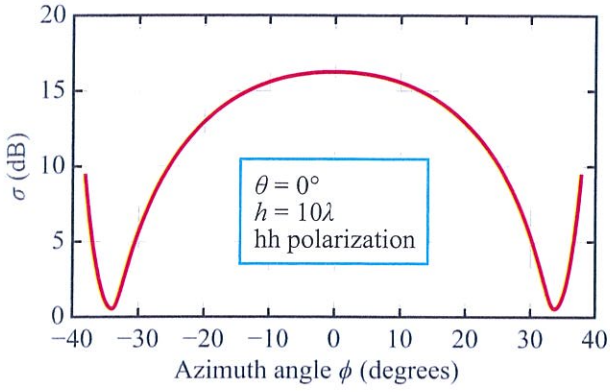

(b) Azimuth pattern

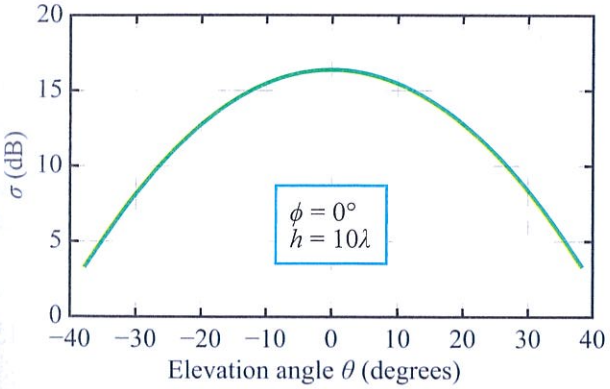

(c) Elevation pattern

Figure 13-35: Trihedral corner reflector: (a) coordinate system showing the angle θ, and (b) and (c) are measured scattering patterns for $h = 10\lambda$ at 9.5 GHz [Sarabandi and Chiu, 1996].

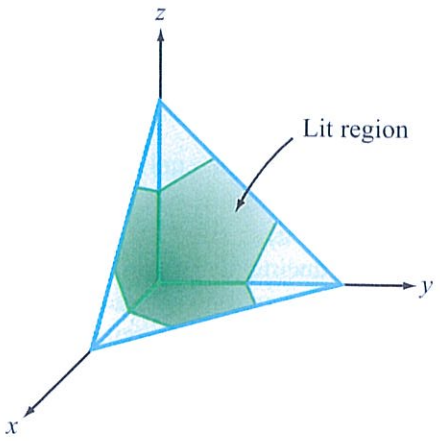

(a) Geometry of the lit region of a trihedral corner reflector

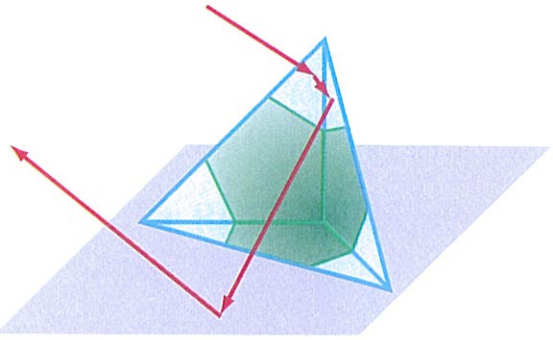

(b) Interaction between the reflector and the ground surface

Figure 13-36: Diagrams of the lit region of the trihedral reflector and of how undesirable components involving reflections by the unlit regions and the ground surface can occur.

it has to be reflected by all three plates. The part of each plate that satisfies this condition is called the ***lit region***. Ray analysis reveals that only 2/3 of the area of each plate satisfies the lit condition (Robertson, 1947; Knott, 1993; Sarabandi and Chiu, 1996), as illustrated in Fig. 13-36(a). This means that the unlit region can be eliminated without reducing the maximum RCS. By eliminating the unlit region, we avoid undesirable scattering contributions involving the combination of

reflection by the unlit region and reflection by the ground [Fig. 13-36(b)]. These undesirable interactions between the reflector and the ground introduce uncertainties that end up compromising the quality and accuracy of the calibration process. In practice, instead of totally eliminating the unlit regions, they are replaced with light-weight absorbing material, thereby maintaining the physical shape of the trihedral, while simultaneously reducing its weight by about 30% and suppressing reflector-ground interactions. Sarabandi and Chiu (1996), who call such a reflector a ***pentagonal corner reflector***, have developed theoretical models for computing its RCS and have verified their results with experimental observations.

13-11.5 Luneburg-Lens Reflector

A spherical Luneburg lens is a dielectric sphere whose index of refraction $n(r)$ varies as a function of r, the distance from the center of the sphere (Fig. 13-37), according to the form defined by Luneburg (1964):

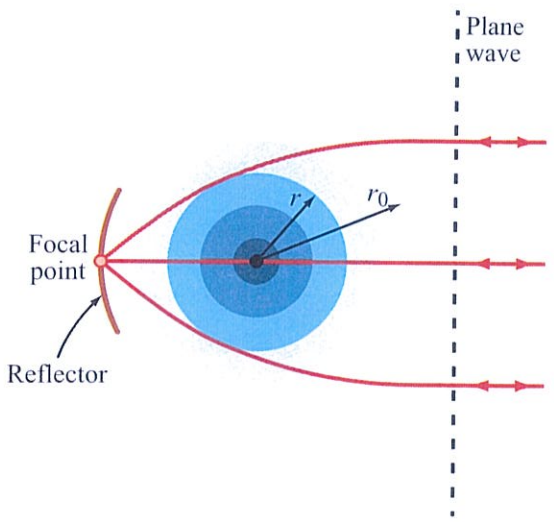

Figure 13-37: A Luneburg lens consists of many concentric dielectric shells, with the relative permittivity increasing from slightly greater than 1 for the outermost shell to 2 at the center. The permittivity variation causes an incident plane wave to refract towards the focal point.

$$n(r) = \sqrt{\varepsilon(r)} = \left[2 - \left(\frac{r}{r_0}\right)^2\right]^{1/2}. \qquad (13.152)$$

In other words, $n(r)$ varies between $n = \sqrt{2}$ at the center ($r = 0$) and $n = 1$ at the periphery ($r = r_0$). A plane wave incident upon such a lens is focused to a point on the opposite surface of the sphere. If a metallic reflecting surface is present on the back side of the sphere, the wave is reflected back in the direction from which it originated. The continuous variation of $n(r)$ is approximated in practice with discrete changes of $n(r)$; typically, 10 or more concentric spherical shells are used, with the outermost shell having a dielectric constant of about 1.1 (Buckley, 1960; Croney and Delany, 1963).

The angular coverage provided by a Luneburg-lens reflector is governed by the geometry of the reflecting surface, as illustrated by Fig. 13-38. Comparisons of measured angular patterns at 9.375 GHz are shown in Fig. 13-38(b) for three types of Luneburg-lens reflectors, in addition to a circular metal plate, and a metal sphere, all with the same diameter (12 inches $\approx$ 30 cm). Also shown is the pattern for a circular corner reflector whose dimensions are such that it can barely be contained within a 12-inch-diameter sphere. The Luneburg-lens reflector provides much wider beamwidths than the flat plate, yet it has approximately the same level of σ_{max}. It is superior also to the corner reflector, in terms of both absolute level (for comparable dimensions) and angular coverage. Its disadvantages are its greater weight and much higher fabrication cost.

In the central angular region, σ_{max} of the Luneburg-lens reflector is equal (theoretically) to that of a circular plate of the same physical cross sectional area,

$$\sigma_{max} = \frac{4\pi A^2}{\lambda^2} = \frac{4\pi^3}{\lambda^2} r_0^4, \qquad (13.153)$$

where r_0 is the radius of the spherical lens. For the reflectors shown in Fig. 13-38(b), σ_{max} of the Luneburg-lens reflector is about 2 dB lower than its theoretical value (compared with the flat plate) and about 28 dB higher than σ of the metal sphere; i.e., larger by a factor of 630. Measured values of σ_{max} usually are slightly smaller than the theoretical value given by Eq. (13.153).

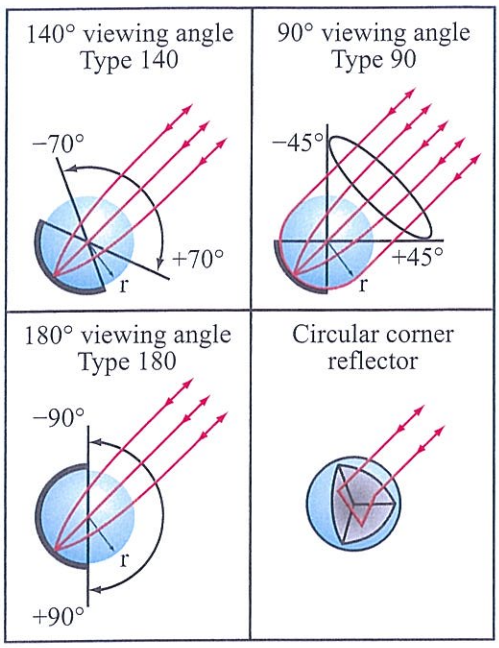

(a) Various types of Luneberg lens reflectors

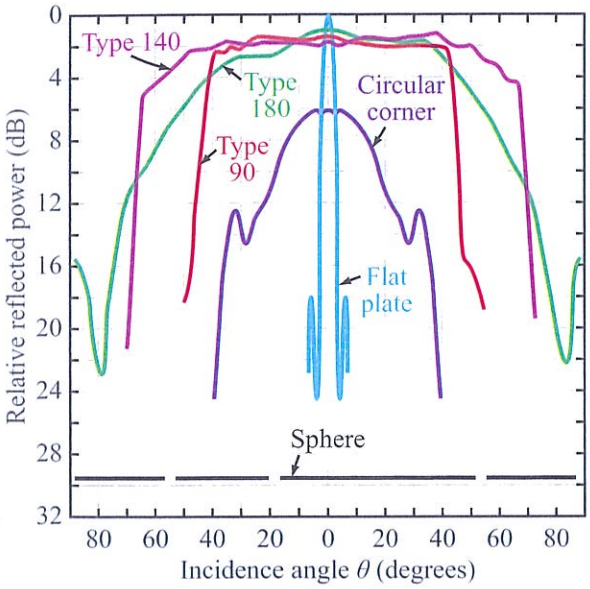

(b) Angular patterns

Figure 13-38: (a) Luneburg lens with three different metal reflector configurations, and (b) angular patterns of the radar cross sections of the three Luneburg reflectors, a circular metal plate and a metal sphere, all 12 inches in diameter, and the largest circular corner reflector that can be contained within a 12-inch-diameter sphere. All cross sections are relative to the peak value of the circular-plate radar cross section. Frequency is 9.375 GHz. [Courtesy of Emerson and Cumming, Inc.]

To account for this difference, σ_{max} of the Luneburg-lens reflector may be redefined as

$$\sigma'_{max} = \eta \frac{4\pi A^2}{\lambda^2}, \tag{13.154}$$

where η is an efficiency factor, $0 \leq \eta \leq 1$. The magnitude of η depends on the wavelength λ and on the number of discrete steps used in approximating the continuous dielectric variation given by Eq. (13.152). To illustrate with an example, measurements of σ'_{max} made over the 1 to 18 GHz region for a 23 cm diameter Luneburg-lens reflector showed that η decreases from about 0.99 at 1 GHz to 0.65 at 8 GHz and to 0.18 at 18 GHz (Stiles et al., 1979).

13-11.6 Comparison of Calibration Targets

Expressions for the maximum radar cross section, σ_{max}, and for the angular coverage, or beamwidth, are summarized in Table 13-5 for the calibration targets discussed in the preceding subsections.

13-12 Active Radar Calibrators (ARCs)

The calibration targets discussed in the preceding subsections are collectively called ***passive*** calibrators, in contrast to a second group of calibrators that use ***active*** electronic amplification of the incident radar signal to boost its level and reradiate it back to the radar. The need for ***active radar calibrators*** (ARCs) was prompted by size and weight considerations, as well as the need to calibrate the cross-polarized channel of a radar scatterometer or imager. Since its invention in the early 1980s (Brunfeldt and Ulaby, 1984b), the ARC has evolved into a highly sophisticated calibrator and has become the standard tool for external calibration of scatterometers and imagers, including polarimetric SAR systems.

To appreciate the attractive features of the ARC as a calibration device, let us consider the size requirements for a trihedral corner reflector. The maximum RCS of a trihedral with edges of length l is $\sigma_{max} = \pi l^4/3\lambda^2$. To build a trihedral with an RCS of 40 dBsm (i.e.,

Table 13-5: Characteristics of passive calibration targets.

Type of Target	σ_{max}[a]	Approximate Half-Power Beamwidth[b]	Comments
Rectangular plate	$4\pi A^2/\lambda^2$	$0.44\lambda/a, 0.44\lambda/b$	Large σ_{max}, very narrow beamwidths
Circular plate	$4\pi A^2/\lambda^2$	$0.25\lambda/r$	Large σ_{max}, very narrow beamwidths
Sphere	A	Omnidirectional	$r > 2\lambda$, small σ
Trihedral corner reflector	$\pi l^4/3\lambda^2$ $= 16\pi A_c^2/9\lambda^2$	$\approx 30°$–$40°$	σ_{max} about 3 dB lower than that of a flat plate with same aperture
Luneburg-lens reflector	$4\pi A^2/\lambda^2$	Up to 180° (140° in practice)	Large σ_{max}, wide beamwidth, efficiency decreases with frequency

[a] A = physical area for the flat plates and cross sectional area for the metal sphere and Luneburg lens. A_c = aperture area of corner reflector.
[b] a, b = sides of rectangular plate, r = radius of circular plate, and radius of sphere, l = edge of trihedral corner reflector.

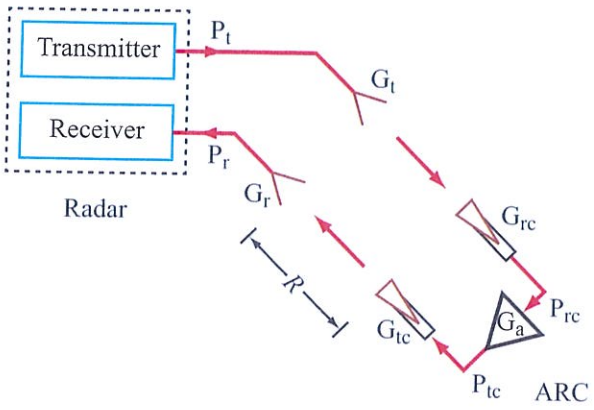

Figure 13-39: The active radar calibrator (ARC) consists of two antennas with an RF amplifier of gain G_a in between.

$\sigma_{max} = 10^4$ m^2) at 10 GHz, l should be 1.7 m, which makes such a trihedral fairly bulky and heavy. The problem is worse at lower frequencies; at 1 GHz, for example, l should be 5.4 m, and at UHF it should be larger still.

The basic concept of the active radar calibrator is very simple: it consists of two antennas separated by an RF amplifier (Fig. 13-39). To a radar, the ARC appears like a target with maximum RCS σ_{ARC} given by (Brunfeldt and Ulaby, 1984b)

$$\sigma_{ARC} = \frac{\lambda^2}{4\pi} G_{rc} G_{tc} G_a, \tag{13.155}$$

where G_{rc} and G_{tc} are the gains of the ARC's receive and transmit antennas and G_a is the ***loop gain***, which includes the gain of the RF amplifier as well as any mismatch or transmission line losses that may be present. The effective beamwidth of the ARC's RCS pattern is dictated by the size of its antennas relative to λ. To use the ARC to calibrate the hh-polarization channel of a scatterometer or imager, the ARC's antennas should have the same polarization orientation and they should be positioned such that their h-polarization direction matches that of the radar. To calibrate the hv-polarization channel, the ARC's receive antenna should be oriented such that its polarization vector is parallel to the v-polarized direction of the signal transmitted by the radar, and its transmit antenna should be oriented such that it radiates an h-polarized signal relative to the radar antenna.

Mutual coupling between the transmit and receive antennas of an ARC limits the maximum amplifier gain that can be used. If the product of the loop gain and coupling coefficient is comparable to or exceeds unity, the feedback system goes into oscillation, which is clearly undesirable. In practice, mutual coupling can

be reduced to an acceptable level by insuring sufficient spatial separation between the two antennas.

Figure 13-40(a) is a diagram of an ARC designed to operate at 5 GHz. It consists of two standard-gain horns, each with a 16 cm × 22 cm aperture and gain $G_{tc} = G_{rc} = 75$ (or 18.75 dB), and a loop gain of 30.5 dB (or $G_a = 1122$). Use of Eq. (13.155) leads to

$$\sigma_{ARC} = \frac{\lambda^2}{4\pi} G_{rc} G_{tc} G_a = \frac{(6 \times 10^{-2})^2}{4\pi} (75)^2 \times 1122$$
$$= 1808, \text{ or } 32.57 \text{ dBsm}.$$

In part (b) of Fig. 13-40, we show azimuthal patterns of the RCS measured for a 30 cm × 30 cm flat plate, a 23 cm diameter Luneburg lens, and the ARC of Fig. 13-40(a). The ARC provides a broad pattern with a maximum RCS larger than that of the metal plate by a factor of 63 (18 dB).

The advantage of the ARC over a trihedral corner reflector is illustrated by the following example. Consider an L-band ($f = 1.275$ GHz) airborne or spaceborne imaging radar with a spatial resolution of 25 m × 25 m. The system is to be calibrated by using a calibration target whose RCS is 20 dB greater than the RCS of the terrain background. From Eq. (13.141) and Fig. 13-31, this condition corresponds to $S_{bc} = 0.1$ and a maximum measurement uncertainty of ±1 dB. The terrain background has a backscattering coefficient $\sigma^0 = -16$ dB. Hence, to satisfy the stated conditions, the calibration target should have an RCS of

$$\sigma \text{ (dBsm)} = -16 \text{ dB} + 10\log(25 \times 25) + 20 \text{ dB}$$
$$= 32 \text{ dBsm} \quad (\text{or } \sigma = 1584.9 \text{ m}^2).$$

Use of Eqs. (13.150) and (13.151) leads to the requirement that a trihedral corner reflector with such an RCS at 1.275 GHz should have sides $l = 3$ m, and a corresponding triangular aperture $A_{eff} = 2.6$ m^2.

The same RCS can be realized by an ARC with a loop gain of 48 dB and two microstrip antennas each $\lambda/2$ on the side (≈ 15 cm). The elevation beamwidth of the RCS of the ARC is 74°, compared with only 40° for the trihedral corner reflector (Brunfeldt and Ulaby, 1984b).

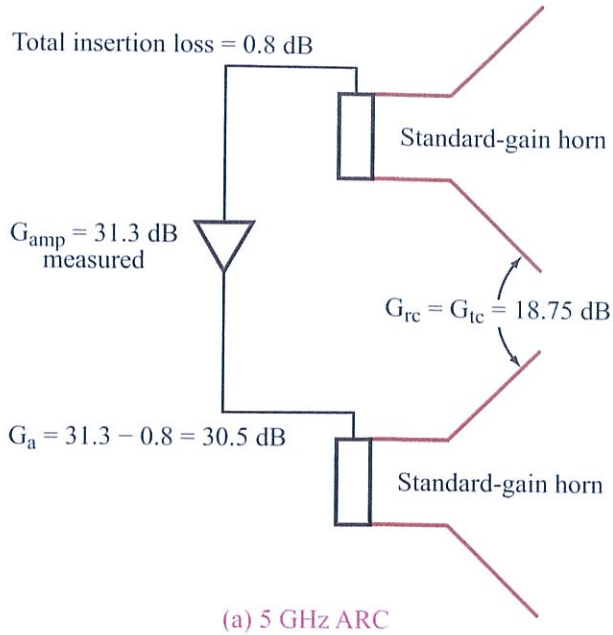

(a) 5 GHz ARC

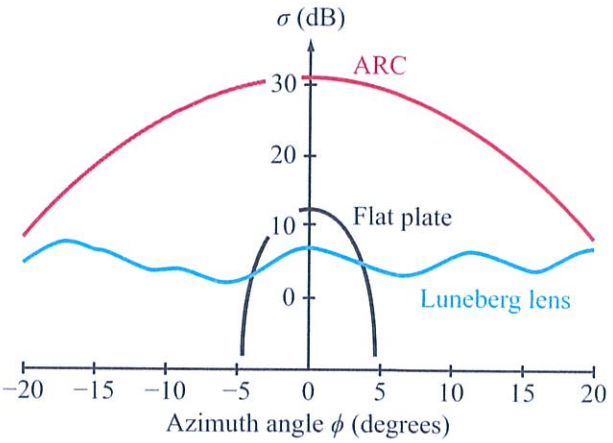

(b) Measured RCS patterns

Figure 13-40: Measured RCS patterns for ARC, 30 cm × 30 cm flat plate and 23 cm Luneburg lens. Measurement frequency is 5 GHz [Brunfeldt and Ulaby, 1984b].

13-13 Polarimetric Active Radar Calibrator

A polarimetric radar transmits a v-polarized signal and then measures the v- and h-polarization components of the backscattered signal using a dual-polarized receiving antenna. The process leads to measuring S_{vv} and S_{hv}, the vv and hv components of the scattering matrix of the target. Upon switching the polarization of the transmitted signal from v to h polarization, repetition of the measurement process leads to S_{hh} and S_{vh} (Fig. 13-41). To calibrate a polarimetric radar system, the calibration target needs to accommodate all four polarization combinations. This can be realized by using an ARC whose antennas are orthogonally polarized relative to one another and whose orientations are at 45° (or 135°) relative to the polarization axes of the radar. Consider the configuration shown in Fig. 13-42. The radar transmit antenna is v polarized and the polarization direction of the ARC receive antenna is at 45° (halfway between the $\hat{\mathbf{v}}$ and $\hat{\mathbf{h}}$ directions). Consequently, the ARC receive antenna extracts a signal whose electric field is only $E_v^t/\sqrt{2}$ of the field E_v^t of the incident wave. The corresponding power extracted by the ARC receive antenna is half of the power carried by the incident wave. After amplification by the RF amplifier, the signal is reradiated towards the radar by a transmit antenna whose polarization vector is oriented at 135° relative to the v-polarization direction. The radar uses two receive channels, one v polarized and the other h polarized. Each channel extracts one-half of the power carried by the reradiated signal. This allows calibration of the vv and hv channels. A similar process with a transmitted h-polarized wave E_h^t leads to calibration of the hh and vh channels. Hence, the 45°-tilted ARC with orthogonally polarized antennas can provide known signals to calibrate all four channels of a polarimetric radar. Such an ARC is called a ***polarimetric ARC***, or PARC for short.

To reduce the overall size and weight of the PARC, Sarabandi et al. (1992a, b) developed a ***single-antenna PARC***, or ***SAPARC***. A block diagram is shown in Fig. 13-43(a), and the physical assembly of the antenna part is shown in Fig. 13-43(b). A square-horn antenna

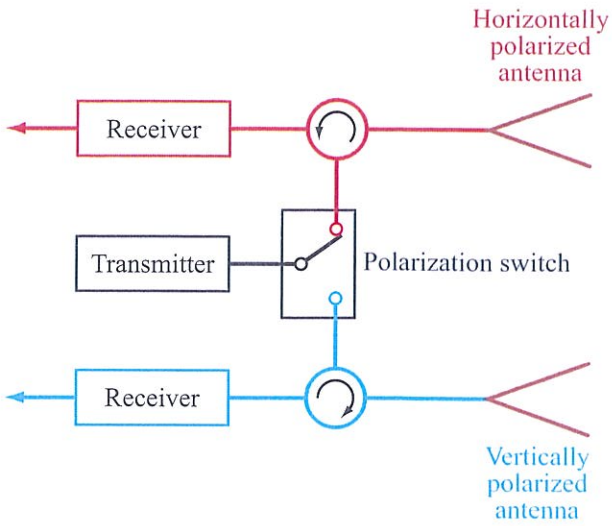

(a) Block diagram

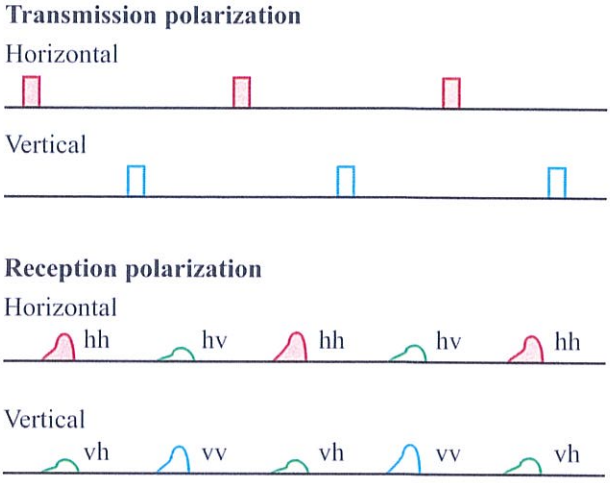

(b) Timing diagram

Figure 13-41: Calibration of polarimetric radar. A polarimetric radar is implemented by alternately transmitting signals out of horizontally and vertically polarized antennas and receiving at both polarizations simultaneously. Two pulses are needed to measure all the elements in the scattering matrix [van Zyl and Kim, 2011].

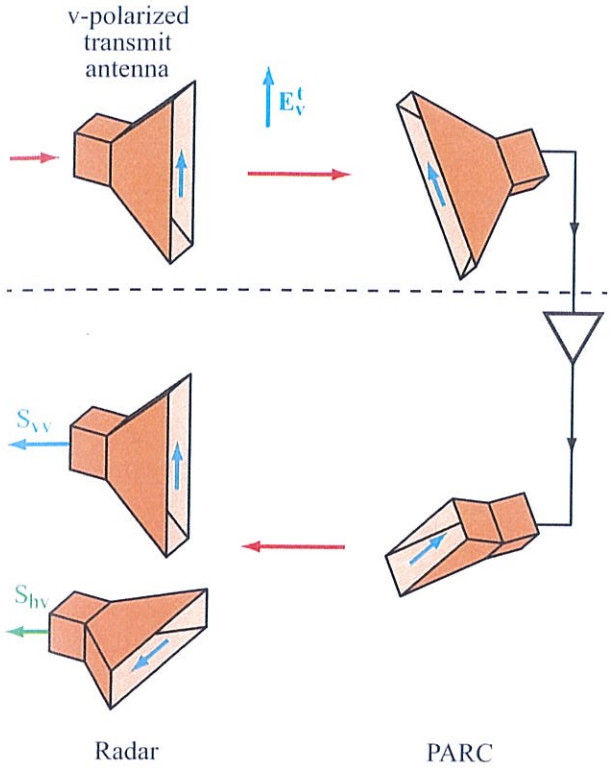

Figure 13-42: PARC with its antennas oriented at 45° relative to radar antennas.

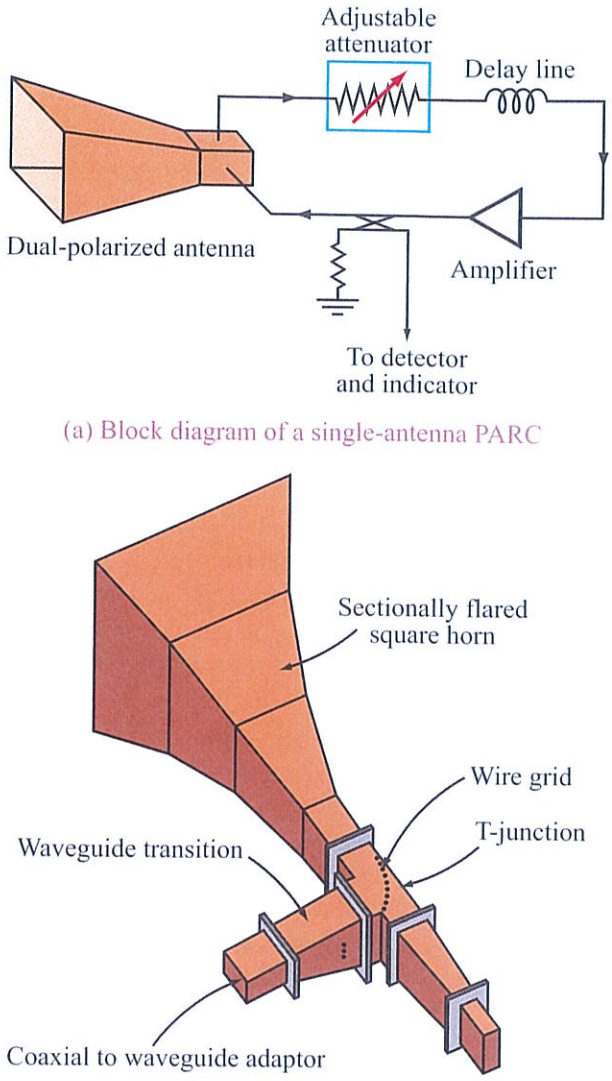

(a) Block diagram of a single-antenna PARC

(b) Antenna assembly of the L-band SAPARC

Figure 13-43: Block diagram and antenna assembly of a single-antenna PARC [Sarabandi et al., 1992b].

that can accommodate both v and h polarizations is connected to a waveguide orthomode transducer (OMT) that uses wire grids placed inside the waveguide section to isolate the v and h ports. The isolation realized using this technique is on the order of 40 dB (Sarabandi et al., 1992b; 1995).

13-14 Polarimetric Scatterometers

Until the mid-1980s, the primary function of a ***magnitude-only scatterometer*** system had been to measure the backscattering coefficient σ^0 of distributed targets, usually as a function of the incidence angle θ. Often, the measurements are made for various configurations of receiving and transmitting antenna polarizations, such as hh, hv, vv, RR, RL and LL. In all cases, however, the quantity measured by the scatterometer is the magnitude of the received signal, and no phase information is recorded. Recall that the first letter signifies the polarization of the receiving antenna and the second letter signifies the polarization of the transmitting antenna, with antenna polarization

always defined for both transmitting and receiving antennas as if the antenna were in a transmitting mode; the letters h, v, R, and L denote horizontal, vertical, right circular, and left circular, respectively. In contrast to such a magnitude-only scatterometer, a ***polarimetric scatterometer*** is configured to measure the complete scattering matrix **S** of the target by measuring the magnitude and phase of the scattered electric field for all linear polarization combinations. The attractive feature of the polarimetric approach lies in the fact that given a matrix **S**, we can use the polarization synthesis technique (Section 5-10) to compute the scattering coefficient of the target for any desired receive-transmit polarization configuration.

To measure the scattering matrix **S** of a target, a radar must be able to transmit and receive two orthogonal polarizations (usually vertical (v) and horizontal (h)) and to measure both the magnitude and phase of the received signals. Although polarimetric scatterometers may be operated from aircraft or satellite platforms, we focus our consideration in this section on short-range scatterometers that typically measure targets at ranges of 20 m or less. This corresponds to a two-way time delay of roughly 133 ns. Because the target is at such a close range, leakage signals that are multiply reflected due to mismatch within the system can appear at the target range as noise with a level well above that of thermal noise. This problem, which is specific to short-range radars, must be seriously considered in the scatterometer design.

In principle, it should be possible to address short-range and noise-related considerations in the design of FM, pulse, and other types of radar systems, but the versatility of vector network analyzers makes them a natural basic building block for short-range polarimetric scatterometers (Ulaby et al., 1988b; Whitt and Ulaby, 1988; Blanchard and Rochier, 1987; Riegger et al., 1987). Hence, this section is concerned with the design and operation of basic network analyzer-based polarimetric scatterometers.

13-14.1 Network Analyzer Principles of Operation

Vector network analyzers measure the magnitude and phase characteristics of linear networks relative to some standard or reference. This is accomplished by making both transmission and reflection measurements to obtain specific characteristics of the network (Fig. 13-44). For transmission measurements, the signal transmitted through the test network is compared with the incident signal, which serves as the reference. For reflection measurements, the signal reflected from the input port is compared with the incident signal. The output port, in this case, is usually terminated with a matched load to remove reflections that travel back through the network and contribute to the reflected signal.

A basic vector network analyzer system consists of (1) an RF source, (2) an RF to IF converter, (3) an IF signal detector and analog-to-digital (A/D) converter, and (4) a digital microprocessor and display. In the context of Fig. 13-44, the RF source is used to supply the incident signal to the test network. The transmitted or reflected RF signal and a sample of the incident signal are then mixed down to the IF range, maintaining the magnitude and phase relationships between the two signals. The IF signals are then detected, converted to digital form, and processed to obtain information about the test network. If a frequency-swept incident signal is used, the result is a measurement of the frequency response of the network, and Fourier transform techniques can be used to obtain the time-domain response.

As an example, Fig. 13-45 illustrates the basic components of an HP 8510 vector network analyzer system used for making transmission-reflection measurements. In general, the principles are the same for other vector network analyzer systems (HP 8753, HP 8720, Wiltron 360, and similar systems by other manufacturers). The system of Fig. 13-45 consists of three pieces of equipment: (1) a synthesized sweeper, which serves as the RF source; (2) a frequency converter, which serves as the RF to IF converter; and (3) a network analyzer and display processor, which serves as the IF detector, A/D converter, and digital processor.

The frequency converter has four ports to which signals can be applied. Of these ports, the a_1 and a_2 ports

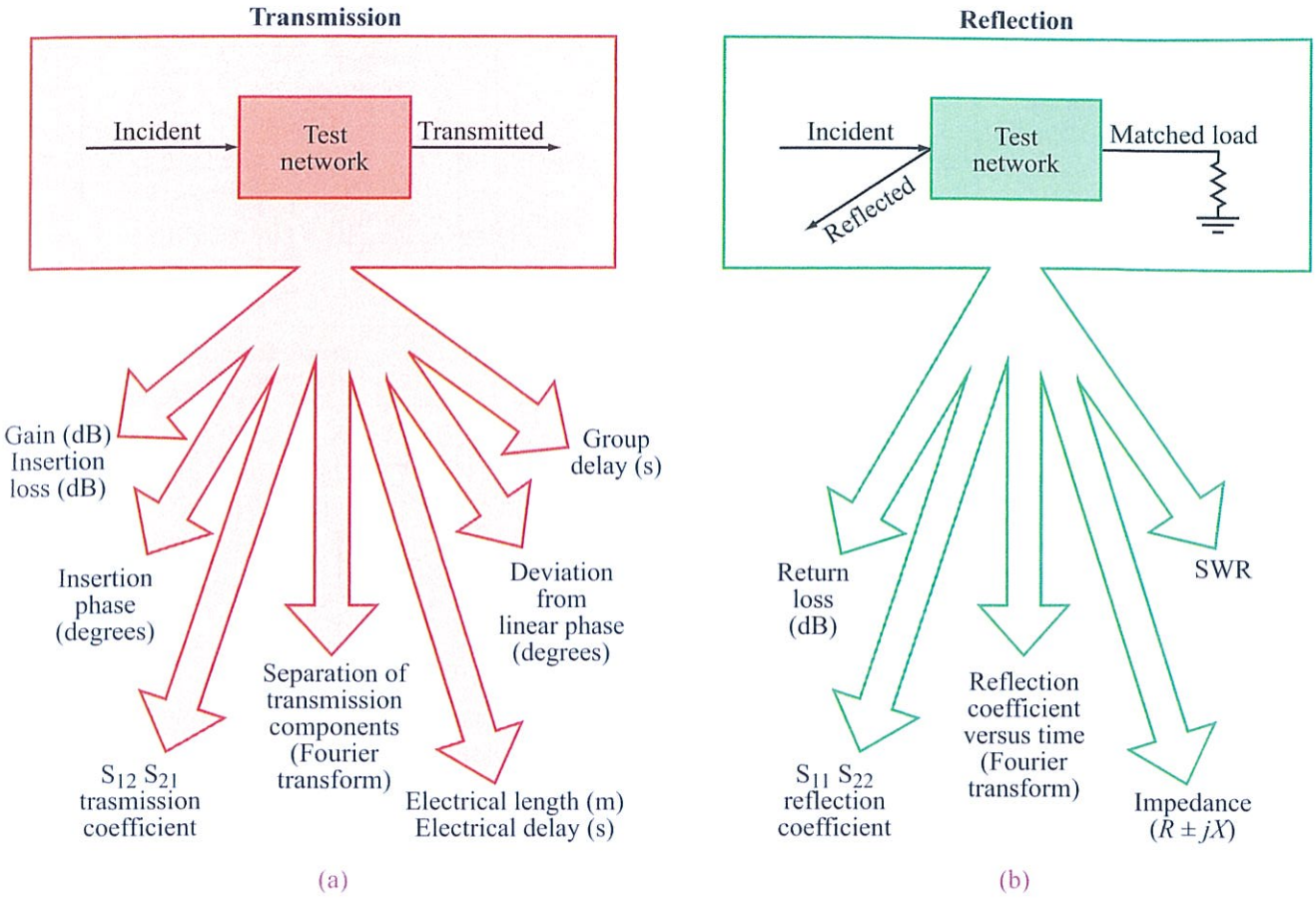

Figure 13-44: Transmission and reflection measurement capabilities of a vector network analyzer [Hewlett-Packard].

are used to input the reference signal, and the b_1 and b_2 ports are used to input the measurement signals. In the basic transmission-reflection configuration, a sample of the signal from the RF source is applied to the a_1 reference port, while the a_2 port is unused. The transmitted and reflected signals are then applied to the b_1 and b_2 measurement ports, respectively. The network analyzer can then provide the magnitude and phase of the reflected and transmitted signals relative to that of the incident signal by forming the ratios:

$$S_{11} = \frac{b_1}{a_1} \quad \text{and} \quad S_{21} = \frac{b_2}{a_1}, \tag{13.156}$$

respectively.

13-14.2 Network Analyzer Operation as a Scatterometer

The measurement system of Fig. 13-45 can be reconfigured to operate like a scatterometer. In the scatterometer configuration, the "test network" is simply some radar target separated from the measurement system by free space. In this case, the signal from the RF source is coupled to free space through an antenna and travels to the target (i.e., test network) through the air medium instead of a coaxial cable or waveguide. The signal reflected from the target is then received by another antenna and is compared with a sample of the transmitted signal from the RF source. The system

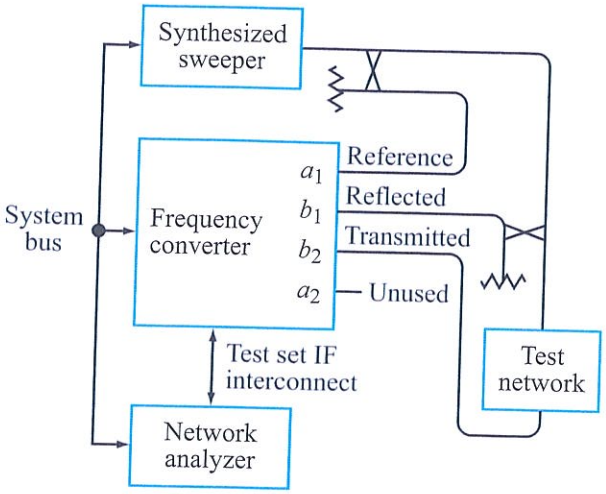

Figure 13-45: Configuration of a network analyzer for transmission and reflection measurements.

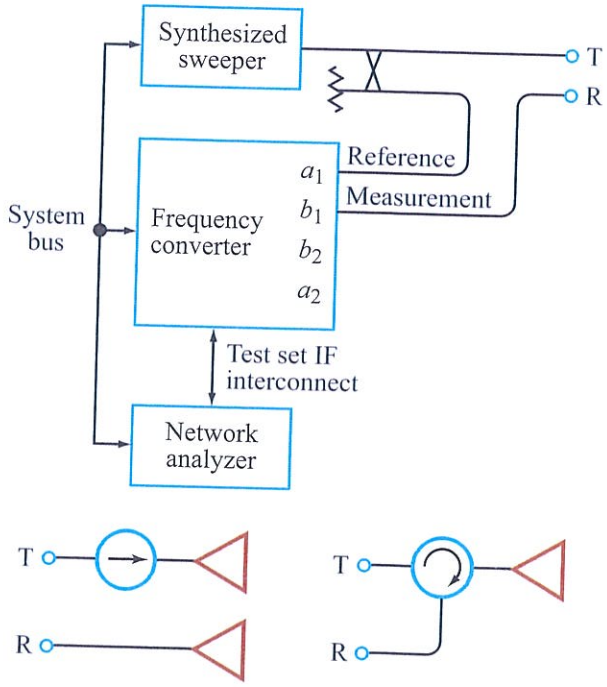

(a) Dual-antenna system (b) Single-antenna system

Figure 13-46: Configuration of a network analyzer for scatterometer measurements; (a) dual-antenna system, (b) single-antenna system.

can be configured as either a dual-antenna system or a single-antenna system (using a circulator to separate the transmitting and receiving channels) as shown in Fig. 13-46.

There is a major difference between the transmission-reflection configuration and the scatterometer configuration. When operating as a scatterometer, there is a relatively long time delay between the returned and transmitted signals due to propagation to the target and back. During this delay, the reference signal has changed frequency by an amount Δf, which corresponds to a phase shift in degrees of $\Delta\phi = 360\,\Delta f\,\tau$, where $\tau = 2R/c$ is the two-way time delay. If a synthesized source is used, the transmitted signal can be stepped in frequency so as to keep the reference signal at the same frequency as the received signal.

The system configuration in Fig. 13-46 represents a traditional (magnitude-only) scatterometer, so it must be modified in order to operate it as a polarimetric scatterometer. Because it measures the complete scattering matrix of a given target, a polarimetric scatterometer must be able to transmit and receive a set of orthogonal polarizations. While other polarization schemes can be used, v- and h-linear polarizations are used here for illustrative purposes to remain consistent with the rest of the text. For the single-antenna system, we add a second polarization channel and apply it to the b_2 port of the network analyzer. For the dual-antenna system, two options are available. An additional channel can be utilized, similar to the single-antenna system, or polarizers can be inserted before the antennas. These different configurations are shown in Fig. 13-47, where the network analyzer is assumed to be configured the same as in Fig. 13-46.

There are many advantages to using a vector network analyzer as the IF processor for a polarimetric scatterometer. The advantages all relate to the many features available with most network analyzers. One of these features is the ease with which the network analyzer can be programmed and controlled by computer over an interface bus. This feature is stressed because it reduces the hardware design to the

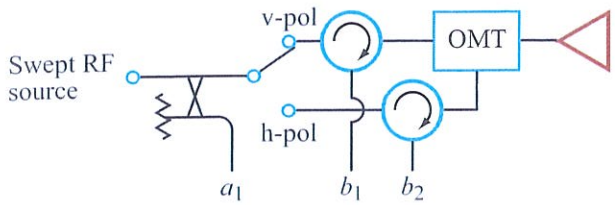

(a) Dual-polarized single-antenna system

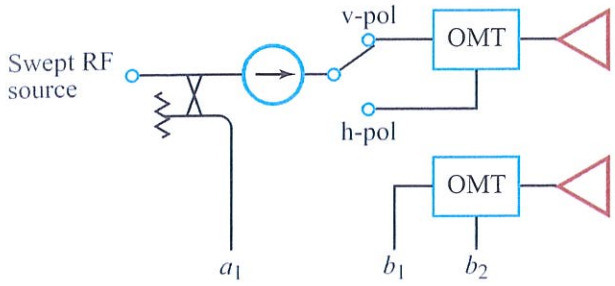

(b) Dual-polarized two-antenna system

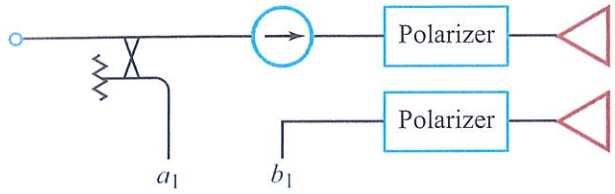

(c) Two-antenna system using polarizers

Figure 13-47: Polarimetric configurations of a network analyzer-based scatterometer: (a) dual-polarized single-antenna system, (b) single-antenna dual-polarized system, and (c) dual-antenna system using polarizers.

consideration of only RF components. The network analyzer supplies all the detection, processing, and data transfer options. To provide a complete description of all the options available with network analyzers is not possible, but we highlight some that are particularly useful in polarimetric scatterometer applications. One of the most useful processing options available with many network analyzers is time-domain operation. Because the returned signal is measured as a function of frequency, real-time Fourier transform techniques can be used to obtain the time-domain response. In scatterometer applications, the result is a measure of the radar return as a function of range. In addition, all other processing operations are available to both time and frequency domains. The signal, for example, may be displayed in the time domain where the data can be processed as a function of range. Time gating can then be used to isolate the return due to targets at a particular range. Suppose a measurement of the backscattered power is desired as a function of depth for a volume of scatterers. By using the time-domain option with time gating, the portion of the returned signal corresponding to a particular depth in the volume can be selected. The position and width of the time gate determines the range and range extent of the small volume within the entire volume of scatterers. The time-gated signal can then be transformed back to the frequency domain to obtain the frequency response of the small volume, as modified by the medium between it and the scatterometer. This process is illustrated in Fig. 13-48.

There are other features that can be used to remove nonvarying errors in the return signal. For example, scattering from objects other than the target can contribute to the noise of the measurement. Many network analyzers have data storage and complex math features that can remove these nonvarying errors. First, the response of the test setup without the target is stored and later subtracted from the response when the target is present, resulting in a measurement of the target response alone. The leakage signals caused by multiple reflections that appear at the target range can be removed in the same manner. An example illustrating this procedure is given in Fig. 13-49.

Another feature that is particularly useful in reducing random noise contributions is IF averaging. With this feature, a specified number of consecutive data traces are continuously averaged. The constant target signals add coherently, but the random noise adds incoherently, thereby improving the signal-to-noise ratio. This is similar to integration in traditional radar systems.

13-14.3 Microwave Polarimetric Scatterometers

Scatterometers must be able to measure targets over a wide range of radar cross sections. In practice, targets

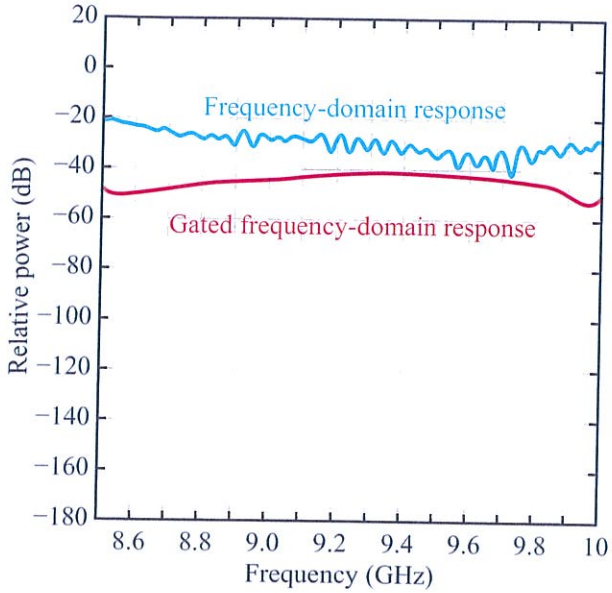

(a) Frequency- and gated frequency-domain response

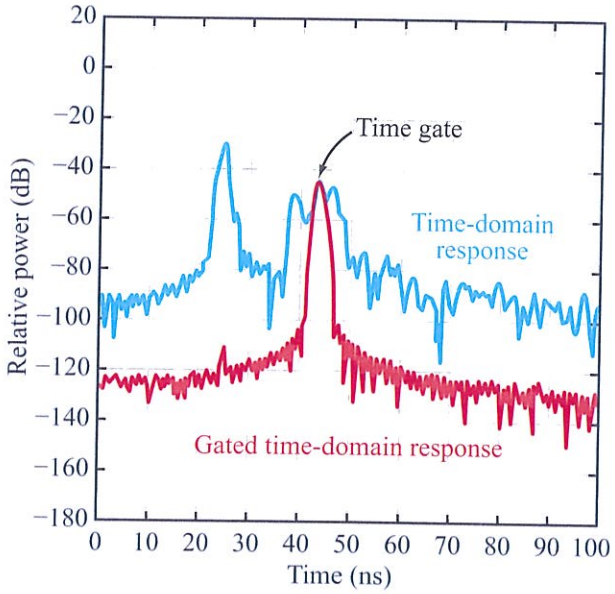

(a) Time- and gated time-domain response

Figure 13-48: Plots illustrating the use of gating with the time-domain option to measure the frequency response as a function of depth within a random medium: (a) frequency-domain response, (b) time-domain response.

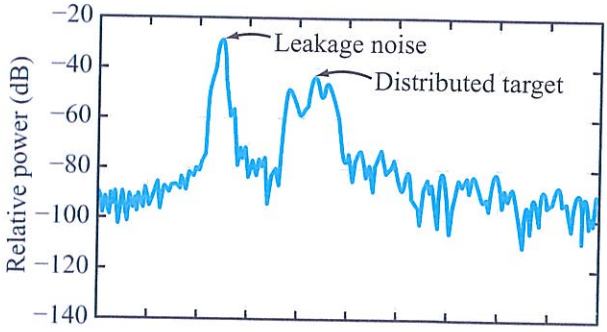

(a) Time-domain response with target

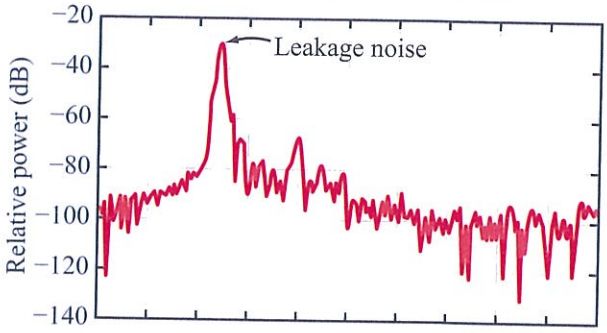

(b) Time-domain response without target

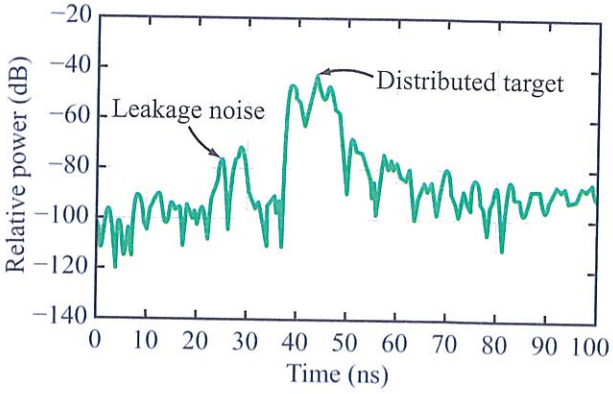

(c) Time-domain response of target alone

Figure 13-49: Plots illustrating the use of complex mathematical operations with trace storage to remove leakage signals: (a) time-domain response with target, (b) time-domain response without target, and (c) time-domain response after subtraction of (b) from (a).

with large radar cross sections are easy to measure, but there is a lower bound on the measurable RCS. This lower bound (***minimum detectable target***) for a given scatterometer at a fixed range from the target is limited by three major factors. The first factor is the thermal noise level, which is the absolute minimum detectable level and it is related to the system noise figure and the system bandwidth. The second limiting factor is the dynamic range of the receiver. This factor usually is dominant when a single antenna is used or if there is insufficient isolation between the transmitting and receiving antennas. In such cases, part of the transmitted signal returns to the receiver's sampler and sets the minimum detectable signal level. This minimum signal level can be determined by dividing the returned signal level by the dynamic range of the sampler. Finally, the third limiting factor is the effect of multiple internal reflections that appear at the target range. In a radar system, there usually exists impedance mismatches between different RF components and between the antenna and free space. A fraction of the transmitted signal corresponding to each mismatched interface returns to the receiver as noise. Multiple reflections between the mismatch interfaces also arrive at the receiver, but with different time delays corresponding to the total path length. The short-range reflections can be distinguished from the target signal in the time domain, but multiple reflections that appear at the target range cannot be separated from the target signal. Therefore, targets with a signal level that is less than the level of the multiple reflections are difficult to detect reliably.

13-15 Calibration of Polarimetric Radars

The advent of polarimetric scatterometers and imaging radars in the early 1980s led to the development of several techniques for calibrating them. The technique proposed by Barnes (1986) characterizes the errors introduced by the transmitter and receiver in terms of ***distortion matrices*** that alter the measured scattering matrix of the target. His calibration technique requires the use of three calibration targets with known radar cross sections, some of which must have zero elements in their scattering matrices. A technique similar to that of Barnes was used by Freeman et al. (1988) where the known target scattering matrices were realized by polarimetric active radar calibrators (PARCs). A technique introduced by Riegger et al. (1987) characterizes the system errors in terms of coupling coefficients between elements of the theoretical scattering matrix and elements of the measured scattering matrix. Riegger's is in essence the same model as that used by Barnes, except that Riegger has expanded the matrix product, which results in twice the number of unknowns. These techniques have been shown to be effective in practical applications, but are limited because the approaches require measurements of targets with a particular form of scattering matrix that is often difficult to realize.

Two additional polarimetric calibration techniques are of interest because they require only a single nondepolarizing target (such as a sphere or trihedral) to correct for co-polarized channel imbalance and absolute magnitude errors. The cross-polarization coupling (or crosstalk) errors are corrected by using targets with unknown scattering matrices. The first technique, proposed by Sarabandi et al. (1990) achieves calibration of the crosstalk errors by measuring any arbitrary depolarizing target. Knowledge of the scattering matrix of the arbitrary target is not required. A similar technique by van Zyl (1990) uses measurements of distributed natural targets to determine the crosstalk errors. The advantage of these techniques is their insensitivity to target positioning, which makes them particularly useful in field calibration.

In this section, we begin by introducing the concept of distortion matrices to model the errors introduced by polarimetric scatterometer systems. With this background, we then show how the technique by Sarabandi et al. (1990) can be used to calibrate polarimetric scatterometers if they have ***diagonal distortion matrices***. Two calibration targets, namely a metal sphere or trihedral reflector and any second target with strong cross-polarized RCS, are required to calibrate the scatterometer. The advantage of this method is that (1) it is relatively insensitive to orientation

of the calibration targets with respect to the antenna coordinate system and (2) theoretical values for the scattering matrix of the second target are not required. Therefore, the calibration requires only the knowledge of the theoretical scattering matrices for a metal sphere or trihedral reflector, which are well known. The applicability of the technique, however, is limited to radars with diagonal distortion matrices.

For systems where no assumptions can be made about the distortion matrices, the technique proposed by Whitt et al. (1991) can be used. The technique requires the measurement of three known targets to determine the distortion matrices that characterize the effect of the measurement system on the transmitted and received waves. The scattering matrices for the known targets can be of any form, provided that a limited set of constraints is satisfied.

13-15.1 System Distortion Matrices

According to Eq. (5.19), the electric field $\mathbf{E}^{bs}$ backscattered by a target is related to the electric field incident upon it, $\mathbf{E}^{i}$, by

$$\mathbf{E}^{bs} = \left(\frac{e^{-jkR_r}}{R_r}\right)\mathbf{S}\mathbf{E}^{i}, \qquad (13.157)$$

where $k = 2\pi/\lambda$, R_r is the range between the radar and the target, and $\mathbf{S}$ is the ***scattering matrix*** of the target in the backscattering alignment convention,

$$\mathbf{S} = \begin{bmatrix} S_{vv} & S_{vh} \\ S_{hv} & S_{hh} \end{bmatrix}. \qquad (13.158)$$

For a polarimetric scatterometer observing a distributed area, $\mathbf{S}$ is the scattering matrix of the area illuminated by the antenna pattern, and for a polarimetric imaging radar, each pixel has a scattering matrix $\mathbf{S}$. The function of either radar is to measure $\mathbf{S}$. Because of errors introduced by the radar system, the measured scattering matrix is a distorted version of the true scattering matrix. The purpose of polarimetric calibration is to determine the distortion errors, so as to obtain an accurate estimate of $\mathbf{S}$.

v-Polarized transmit mode

The calibration problem can be modeled in terms of the generalized schematic representation shown in Fig. 13-50. Figure 13-50(a) depicts the condition when the polarization switch of the transmit antenna is set to transmit a v-polarized wave of amplitude E_0. Because the system is nonideal, the transmitted field $\mathbf{E}^{t}$ consists of a v-polarized component $T_{vv}E_0$ and an unintended

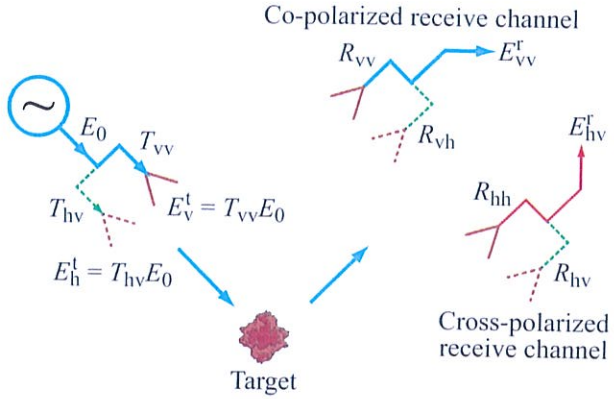

(a) v-polarized transmit configuration

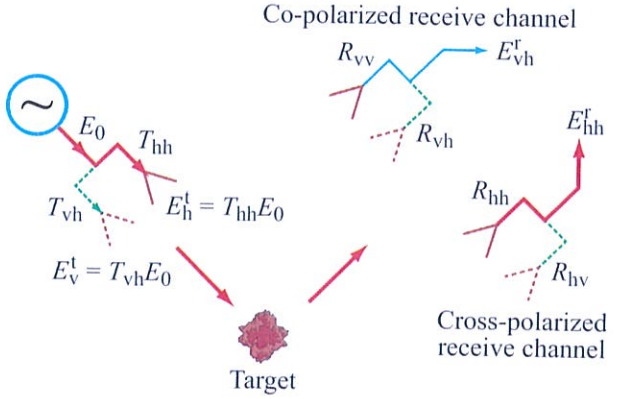

(b) h-polarized transmit configuration

Figure 13-50: Schematic representation of transmitting and receiving antennas; (a) v-polarized transmitting configuration, (b) h-polarized transmitting configuration. The dashed lines represent polarization coupling. For an antenna with perfect polarization isolation, the coupling coefficients would be zero.

h-polarized component $T_{hv}E_0$:

$$\mathbf{E}^t = E_0 \begin{bmatrix} T_{vv} \\ T_{hv} \end{bmatrix}, \tag{13.159}$$

where the deviation of T_{vv} from 1 is due to amplitude and phase errors in the transmitted signal, and T_{hv} represents the coupling between the v and h ports of the antenna. For an ideal transmit antenna, $T_{vv} = 1$ and $T_{hv} = 0$. The incident field $\mathbf{E}^i$ at the scatterer location is related to $\mathbf{E}^t$ by

$$\mathbf{E}^i = \left(\frac{G_t}{4\pi R_r^2}\right)^{1/2} e^{-jkR_r}\mathbf{E}^t, \tag{13.160}$$

where G_t is the nominal gain of the transmit antenna. Combining Eqs. (13.157), (13.159), and (13.160) leads to

$$\mathbf{E}^{bs} = \frac{1}{R_r^2}\left(\frac{G_t}{4\pi}\right)^{1/2} e^{-j2kR_r}\,\mathbf{S}\begin{bmatrix} T_{vv} \\ T_{hv} \end{bmatrix} E_0. \tag{13.161}$$

The receive antenna of a polarimetric radar has two channels, one intended to detect the v-polarized component of $\mathbf{E}^{bs}$ and the other to detect its h-polarized component. The receive antenna also may have distortions, so the received electric field $\mathbf{E}^r$ may be modeled as

$$\mathbf{E}^r = K_1\left(\frac{G_r\lambda^2}{4\pi}\right)^{1/2}\begin{bmatrix} R_{vv} & R_{vh} \\ R_{hv} & R_{hh} \end{bmatrix}\mathbf{E}^{bs}, \tag{13.162}$$

where K_1 is a conversion constant related to the effective area of the receive antenna and transmission-line losses. The receive antenna parameters R_{vv} and R_{hh} account for amplitude or phase distortions introduced by the receive antenna, and R_{vh} and R_{hv} account for cross-polarization coupling. For an ideal, distortion-free receive antenna, $R_{vv} = R_{hh} = 1$ and $R_{hv} = R_{vh} = 0$.

Combining Eqs. (13.161) and (13.162) leads to

$$\mathbf{E}^r = \begin{bmatrix} E_{vv}^r \\ E_{hv}^r \end{bmatrix} = e^{-j2kR_r}\frac{K}{R_r^2}\begin{bmatrix} R_{vv} & R_{vh} \\ R_{hv} & R_{hh} \end{bmatrix}\begin{bmatrix} S_{vv} & S_{vh} \\ S_{hv} & S_{hh} \end{bmatrix}\begin{bmatrix} T_{vv} \\ T_{hv} \end{bmatrix}$$

(v-pol transmit mode) (13.163)

with

$$K = K_1\left(\frac{G_tG_r\lambda^2}{(4\pi)^2}\right)^{1/2} E_0. \tag{13.164}$$

In Eq. (13.163), E_{vv}^r and E_{hv}^r are the electric fields measured by the v-polarized and h-polarized receive channels when the transmit antenna is set to transmit v polarization.

h-Polarized transmit mode

When the polarization switch of the transmit antenna is switched so that the antenna transmits a horizontally polarized wave, the applicable system configuration is as shown in Fig. 13-50(b). In this case, $\mathbf{E}^r$ is given by

$$\mathbf{E}^r = \begin{bmatrix} E_{vh}^r \\ E_{hh}^r \end{bmatrix} = e^{-j2kR_r}\frac{K}{R_r^2}\begin{bmatrix} R_{vv} & R_{vh} \\ R_{hv} & R_{hh} \end{bmatrix}\begin{bmatrix} S_{vv} & S_{vh} \\ S_{hv} & S_{hh} \end{bmatrix}\begin{bmatrix} T_{vh} \\ T_{hh} \end{bmatrix}.$$

(h-pol transmit mode) (13.165)

General form

Equations (13.163) and (13.165) can be combined into the compact form

$$\mathbf{E}^r = e^{-j2kR_r}\frac{K}{R_r^2}\,\mathcal{R}\,\mathbf{S}\,\mathcal{T}\,\mathbf{p}^t, \tag{13.166}$$

where

$$\mathbf{E}^r = \begin{bmatrix} E_{vv}^r \\ E_{hv}^r \end{bmatrix} \quad \text{and} \quad \mathbf{p}^t = \hat{\mathbf{v}} = \begin{bmatrix} 1 \\ 0 \end{bmatrix} \quad \textbf{(v-pol)} \tag{13.167a}$$

when the polarization switch of the transmitter is set to transmit vertical polarization, and

$$\mathbf{E}^r = \begin{bmatrix} E_{vh}^r \\ E_{hh}^r \end{bmatrix} \quad \text{and} \quad \mathbf{p}^t = \hat{\mathbf{h}} = \begin{bmatrix} 0 \\ 1 \end{bmatrix} \quad \textbf{(h-pol)} \tag{13.167b}$$

when it is set to transmit horizontal polarization. The ***receive*** and ***transmit distortion matrices*** $\mathcal{R}$ and $\mathcal{T}$ are given by

$$\mathcal{R} = \begin{bmatrix} R_{vv} & R_{vh} \\ R_{hv} & R_{hh} \end{bmatrix}, \tag{13.168a}$$

and

$$\mathcal{T} = \begin{bmatrix} T_{vv} & T_{vh} \\ T_{hv} & T_{hh} \end{bmatrix}. \tag{13.168b}$$

13-15.2 Distortionless Antennas

For an ideal radar with distortionless antennas, $\mathcal{R} = \mathcal{T} = \mathbf{I}$, where $\mathbf{I}$ is the identity matrix, in which case Eq. (13.166) reduces to

$$\mathbf{E}^{\mathrm{r}} = e^{-j2kR_{\mathrm{r}}} \frac{K}{R_{\mathrm{r}}^2} \mathbf{S}\,\mathbf{p}^{\mathrm{t}}. \tag{13.169}$$

The range R_{r} is proportional to one-half of the two-way-travel time delay measured by the radar, and K can be determined by calibrating the radar against a target of known RCS. By performing four measurements, one pair with $\mathbf{p}^{\mathrm{t}} =$ v polarized and the second pair with $\mathbf{p}^{\mathrm{t}} =$ h polarized, the four measurements of $\mathbf{E}^{\mathrm{r}}$ provide the four values of $\mathbf{S}$. This is the ideal case; the more realistic cases follow.

13-15.3 Reciprocal Distortion Matrices

With some single-antenna polarimetric radar systems, the transmit and receive distortion matrices are simply the transpose of one another. For such a ***reciprocal antenna*** system, $\mathcal{R} = \widetilde{\mathcal{T}}$, in which case Eq. (13.166) assumes the form

$$\mathbf{E}^{\mathrm{r}} = e^{-j2kR_{\mathrm{r}}} \frac{K}{R_{\mathrm{r}}^2} \widetilde{\mathcal{T}}\,\mathbf{S}\,\mathcal{T}\,\mathbf{p}^{\mathrm{t}}. \tag{13.170}$$

13-15.4 Matrix Inversion

Writing the components of $\mathbf{E}^{\mathrm{r}}$ and $\mathbf{p}$ in Eq. (13.166) explicitly for $\mathbf{p} = \hat{\mathbf{v}}$ and $\mathbf{p} = \hat{\mathbf{h}}$ gives

$$\begin{bmatrix} E_{\mathrm{vv}}^{\mathrm{r}} \\ E_{\mathrm{hv}}^{\mathrm{r}} \end{bmatrix} = e^{-j2kR_{\mathrm{r}}} \frac{K}{R_{\mathrm{r}}^2} \mathcal{R}\,\mathbf{S}\,\mathcal{T} \begin{bmatrix} 1 \\ 0 \end{bmatrix} \tag{13.171a}$$

and

$$\begin{bmatrix} E_{\mathrm{vh}}^{\mathrm{r}} \\ E_{\mathrm{hh}}^{\mathrm{r}} \end{bmatrix} = e^{-j2kR_{\mathrm{r}}} \frac{K}{R_{\mathrm{r}}^2} \mathcal{R}\,\mathbf{S}\,\mathcal{T} \begin{bmatrix} 0 \\ 1 \end{bmatrix}, \tag{13.171b}$$

which can be combined into

$$\begin{bmatrix} E_{\mathrm{vv}}^{\mathrm{r}} & E_{\mathrm{vh}}^{\mathrm{r}} \\ E_{\mathrm{hv}}^{\mathrm{r}} & E_{\mathrm{hh}}^{\mathrm{r}} \end{bmatrix} = e^{-j2kR_{\mathrm{r}}} \frac{K}{R_{\mathrm{r}}^2} \mathcal{R}\,\mathbf{S}\,\mathcal{T}. \tag{13.172}$$

Once the distortion matrices $\mathcal{R}$ and $\mathcal{T}$ have been determined through calibration (as discussed in the next section), the true scattering matrix $\mathbf{S}$ can be obtained from

$$\mathbf{S} = \left(\frac{R_{\mathrm{r}}^2}{K} e^{j2kR_{\mathrm{r}}} \right) \mathcal{R}^{-1} \begin{bmatrix} E_{\mathrm{vv}}^{\mathrm{r}} & E_{\mathrm{vh}}^{\mathrm{r}} \\ E_{\mathrm{hv}}^{\mathrm{r}} & E_{\mathrm{hh}}^{\mathrm{r}} \end{bmatrix} \mathcal{T}^{-1}. \tag{13.173}$$

For a reciprocal antenna with $\mathcal{R} = \widetilde{\mathcal{T}}$, characterization of only one matrix is required, simplifying the calibration task considerably. This representation assumes that the distortion matrices are invertible, which is generally the case for real radar systems. The phase factor $\phi = 2kR_{\mathrm{r}}$ is difficult to measure because the phase center of the target and the target position must be known exactly. Usually, only the phases of S_{hv}, S_{vh}, and S_{hh} relative to that of S_{vv} are needed for polarization synthesis or other applications.

13-15.5 Antennas with Diagonal Distortion Matrices

If the radar to be calibrated has excellent cross-polarization isolation, the distortion matrices are approximately diagonal. A ***diagonal distortion matrix*** corresponds to perfect isolation between the v and h ports of the radar antenna; thus,

$$T_{\mathrm{vh}} = T_{\mathrm{hv}} = R_{\mathrm{vh}} = R_{\mathrm{hv}} = 0. \tag{13.174}$$

Even though a polarimetric radar may use only a single antenna to provide both transmit and receive functions, for purposes of illustration we use the block diagram shown in Fig. 13-51 to represent a radar with perfect cross-polarization isolation.

Imposing the condition given by Eq. (13.174) onto Eq. (13.172) leads to

$$\begin{bmatrix} E_{\mathrm{vv}}^{\mathrm{r}} & E_{\mathrm{vh}}^{\mathrm{r}} \\ E_{\mathrm{hv}}^{\mathrm{r}} & E_{\mathrm{hh}}^{\mathrm{r}} \end{bmatrix} = e^{-j2kR_{\mathrm{r}}} \frac{K}{R_{\mathrm{r}}^2} \begin{bmatrix} R_{\mathrm{vv}}T_{\mathrm{vv}}S_{\mathrm{vv}} & R_{\mathrm{vv}}T_{\mathrm{hh}}S_{\mathrm{vh}} \\ R_{\mathrm{hh}}T_{\mathrm{vv}}S_{\mathrm{hv}} & R_{\mathrm{hh}}T_{\mathrm{hh}}S_{\mathrm{hh}} \end{bmatrix}. \tag{13.175}$$

This expression can be abbreviated as

$$E_{pq}^{\mathrm{r}} = e^{-j2kR_{\mathrm{r}}} \frac{K}{R_{\mathrm{r}}^2} R_{pp}T_{qq}S_{pq}, \tag{13.176}$$

$$p, q = \text{ h or v.}$$

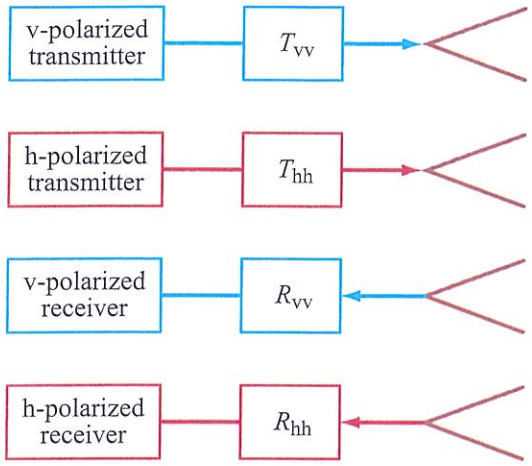

Figure 13-51: Simplified block diagram of a dual-polarized radar system with channel imbalances but no cross-channel leakage.

The standard calibration procedure involves the use of one reference target of known scattering matrix. Upon measuring E^r_{pq} with S_{pq} known, the quantity $(KR_{pp}T_{qq})$ can be determined in both amplitude and phase for all four polarization combinations, with the phase being relative to a selected reference.

The calibration procedure is simple and straightforward, but its accuracy depends on the accuracy with which the scattering matrix $\mathbf{S}$ of the calibration target is known. Of all possible calibration targets, the metal sphere is the easiest to align, and its scattering matrix can be computed exactly (Section 8-5.4). For downward-looking airborne or spaceborne radars, however, a metal sphere is not a practical calibration target because its RCS is not sufficiently large to dominate over the backscatter from the terrain background (see Section 13-10.3), but it is perfectly suitable for calibrating ground-based scatterometers if placed on a nonreflecting pole as depicted in Fig. 13-30(a).

A metal sphere can be used to calibrate only the vv and hh channels of a ground-based scatterometer, because the sphere is a nondepolarizing target: its $S_{hv} = S_{vh} = 0$. Hence, as we see later, we use the sphere to calibrate the co-pol channels and then we perform a second calibration against any depolarizing target (without the need to know its scattering matrix) to calibrate the cross-polarized channels. The calibration procedure is described in detail in the publication by Sarabandi et al. (1990). An abbreviated version follows.

The co-polarized scattering amplitudes of a metal sphere are $S_{vv} = S_{hh} = S_0$, with S_0 being a known quantity. If the radar is used to measure the received electric field $\mathbf{E}^r$ for vv and hh polarizations with the sphere located at a range R_0 from the radar antenna, Eq. (13.176) yields

$$E^0_{vv} = e^{-j2kR_0} \frac{K}{R_0^2} R_{vv} T_{vv} S_0, \tag{13.177a}$$

$$E^0_{hh} = e^{-j2kR_0} \frac{K}{R_0^2} R_{hh} T_{hh} S_0, \tag{13.177b}$$

where the subscript and superscript "0" denote quantities associated with the metal sphere. Similarly, we use subscript and superscript "u" to denote quantities associated with measurements performed on an unknown target or surface of scattering matrix $\mathbf{S}^u$:

$$E^u_{vv} = e^{-j2kR_u} \frac{K}{R_u^2} R_{vv} T_{vv} S^u_{vv}, \tag{13.178a}$$

$$E^0_{hh} = e^{-j2kR_u} \frac{K}{R_u^2} R_{hh} T_{hh} S^u_{hh}. \tag{13.178b}$$

Combining the two pairs of equations yields

$$S^u_{vv} = \left(\frac{E^u_{vv}}{E^0_{vv}}\right)\left(\frac{R_u}{R_0}\right)^2 e^{-j2k(R_0-R_u)} S_0, \tag{13.179a}$$

$$S^u_{hh} = \left(\frac{E^u_{hh}}{E^0_{hh}}\right)\left(\frac{R_u}{R_0}\right)^2 e^{-j2k(R_0-R_u)} S_0. \tag{13.179b}$$

All quantities on the right-hand side of Eq. (13.179) are either known (such as k and S_0) or measured by the radar. Hence, Eq. (13.179) provides calibrated values of the co-polarized components of the scattering matrix of the ground cell illuminated by a scatterometer or the pixel area imaged by a SAR (when using a strong calibration target such as an ARC instead of the sphere).

Calibration of the cross-polarized channels calls for measuring the hv and vh channels of the received electric

field with the radar pointed at a depolarizing calibration target with significant cross-polarized scattering amplitudes. A tilted cylinder or a PARC are perfect candidates. If we denote the measurements with the symbol "c," we have

$$E^{c}_{hv} = e^{-j2kR_c}\frac{K}{R_c^2}R_{hh}T_{vv}S^{c}_{hv}, \tag{13.180a}$$

$$E^{c}_{vh} = e^{-j2kR_c}\frac{K}{R_c^2}R_{vv}T_{hh}S^{c}_{vh}. \tag{13.180b}$$

The reciprocity theorem (Section 5-3.2) states that in the backscattering direction,

$$S^{c}_{hv} = S^{c}_{vh}$$

in the BSA convention. Next, we define the ratio of the two measurements as K_1:

$$K_1 = \frac{E^{c}_{hv}}{E^{c}_{vh}} = \frac{R_{hh}T_{vv}}{R_{vv}T_{hh}}. \tag{13.181}$$

Also, from the co-polarized measurements given by Eq. (13.177) for the sphere or a PARC, we define the product K_2 as

$$K_2 = E^{0}_{vv}E^{0}_{hh} = \frac{K^2}{R_0^4}e^{-j4kR_0}R_{vv}T_{vv}R_{hh}T_{hh}S_0^2. \tag{13.182}$$

Use of Eq. (13.180), in combination with Eqs. (13.181) and (13.182), leads to the solution

$$S^{u}_{hv} = \left(\frac{E^{u}_{hv}}{\sqrt{K_1K_2}}\right)\left(\frac{R_u}{R_0}\right)^2 e^{-j2k(R_0-R_u)}S_0, \tag{13.183a}$$

$$S^{u}_{vh} = \sqrt{\frac{K_1}{K_2}}E^{u}_{vh}\left(\frac{R_u}{R_0}\right)^2 e^{-j2k(R_0-R_u)}S_0. \tag{13.183b}$$

According to the results reported by Sarabandi et al. (1990), this calibration method can be used to calibrate a ground-based scatterometer to an accuracy of ± 0.3 dB in magnitude and $\pm 5°$ in phase.

13-15.6 Nonreciprocal Systems with Full Distortion Matrices

In the general case, the transmit and receive antennas may not be reciprocal of one another, and the isolation between the v and h ports may not be sufficient to justify setting the cross terms of the distortion matrices equal to zero [i.e., Eq. (13.174)]. From Eq. (13.172), the four channels of the received signal are represented by

$$\begin{bmatrix} E^{r}_{vv} & E^{r}_{vh} \\ E^{r}_{hv} & E^{r}_{hh} \end{bmatrix} = e^{-j2kR_r}\frac{K}{R_r^2}\begin{bmatrix} R_{vv} & R_{vh} \\ R_{hv} & R_{hh} \end{bmatrix}\begin{bmatrix} S_{vv} & S_{vh} \\ S_{hv} & S_{hh} \end{bmatrix}\begin{bmatrix} T_{vv} & T_{vh} \\ T_{hv} & T_{hh} \end{bmatrix}. \tag{13.184}$$

To calibrate the radar, we need to determine K, the four elements of $\mathcal{R}$ and the four elements of $\mathcal{T}$. This can be accomplished by using three different calibration targets with known scattering matrices (Whitt et al., 1991). Alternatively, the necessary number of calibration targets can be reduced to fewer than three by taking advantage of reciprocity properties of both the calibration target and the terrain, and by invoking appropriate approximations (van Zyl and Kim, Chapter 4, 2011). Useful calibration-related references include Quegan (1994), Klein and Freeman (1991), van Zyl (1990), Cordey (1993), Zebker and Lou (1990), Freeman et al. (1995), and Sarabandi et al. (1995).

13-16 GNSS-R Bistatic Radar

The use of ***Global Navigation Satellite System*** (GNSS) signals of opportunity, such as those transmitted by the U.S. Global Positioning System (GPS), European ***Galileo***, and Russian ***Globalnaya Navigatsionnaya Sputnikovaya Sistema*** (GLONASS) satellites, for remote sensing purposes can be divided into two general classes. The ***radio occultation technique*** (GNSS-RO) discussed in Section 9-13 provides direct measurements of atmospheric refractivity profiles and, by inference, of the profiles of water-vapor density and air temperature. The ***reflectometry technique*** (GNSS-R) provides direct measurements of the bistatic radar cross section of the Earth surface and of the range to the surface, from which properties of the scattering target can be discerned. See Section 5-4 for a general discussion of bistatic radar. GNSS-R measurements are made using a forward

scattering geometry, at which the radar cross section is generally highest and the scattered signal strength largest. Hall and Cordey (1988) first suggested the use of GNSS signals as a means of making bistatic scatterometer measurements of the ocean surface. A modified GPS navigation receiver could be used as the receive side of a bistatic radar link, and the magnitude of the power received from GPS signals scattered by the ocean could be related to the radar cross section of its surface. Martin-Neira (1993) later extended the possible applications to include ocean altimetry. GNSS signals are modulated by long pseudorandom noise (PRN) codes that enable highly accurate determination of the time-of-flight between the transmitter and receiver, in order to support precise position determination by triangulation. This feature can also be used for altimetry by measuring the difference in time-of-flight between a direct signal path from the transmitter to the receiver and a second signal path that is reflected by the ocean surface. If the locations of the transmitter and receiver are sufficiently well known, the height above sea level of the surface can be inferred from the difference in time-of-flight.

Early experimental demonstrations of the GNSS-R technique were made from stationary platforms and aircraft. Garrison et al. (1998) reported the first serious examination of how bistatic scattering from the ocean surface is related to the local sea state. The ocean surface roughness and, by inference, the near surface wind speed, are found to be highly correlated with the strength of the scattered signal at the specular point of reflection and with the extent of the diffuse scattering away from the specular point. As the winds and the roughness increase, the specular point scattering decreases in magnitude and the ***diffuse scattering region*** (also referred to as the ***glistening zone*** in optics) increases in extent. Both characteristics can be measured and used to estimate wind speed. Platform and airborne demonstrations of other applications of GNSS-R soon followed, including sea-ice mapping (Komjathy et al., 2000) and near-surface soil moisture content (Masters et al., 2004). In each case, the general approach taken is similar to that of conventional backscatter scatterometry, in which the received power is converted to radar cross section by inversion of the bistatic radar equation, which is then related to the dielectric and roughness properties of the target.

There are several important differences between a conventional backscatter scatterometer and a GNSS-R bistatic radar:

(1) The dependence of the radar cross section on target properties can be quite different between backscatter and forward scatter. For example, increasing ocean surface roughness will tend to increase the backscatter and decrease the forward scatter. For this reason, backscatter scatterometers are more amenable to the measurement of higher wind speeds, and GNSS-R bistatic radars have improved performance at lower wind speeds.

(2) The radar hardware is generally simpler and smaller and requires lower power for GNSS-R because there is no transmitter involved, and because GNSS receiver technology has become highly refined to support its mass commercial market.

(3) With GNSS-R systems, precise determination of the location of the scattering target does not require accurate antenna pointing control or knowledge. This is because if the locations of the transmitter and receiver are well known (as is typically the case with standard GNSS navigation capabilities), then the location of the specular point can be determined analytically from geometrical considerations. This can significantly simplify the requirements levied on the airborne or spaceborne platform on which the receiver is deployed.

The first spaceborne detection of an ocean-reflected GPS signal was made by Lowe et al. (2002), using calibration data from the SIR-C radar experiment that fortuitously happened to fall within the transmit passband of the GPS L2 signal at 1228 MHz. A more intentional effort to demonstrate the capabilities of spaceborne GNSS-R remote sensing was undertaken by the UK Space Agency's Disaster Monitoring Constellation (UK-DMC) program. UK-DMC-1 was launched in 2003 into a 680 km polar orbit with a

GNSS-R payload specifically designed to measure GPS signals scattered from the Earth surface. In addition to its GPS receiver, the payload included a nadir-pointing antenna with a peak gain of 11.8 dB and a 3 dB beamwidth of $20° \times 70°$. The mission also supported technology demonstrations for many other payloads, so the on-board GNSS-R processing capability was limited to measurements of up to three reflected signals simultaneously for 20 seconds at a time. The 20-second data records were telemetered to the ground, where they were processed into images of the scattered power received from the surface in the vicinity of the specular point. These images are referred to as ***Delay Doppler Maps***.

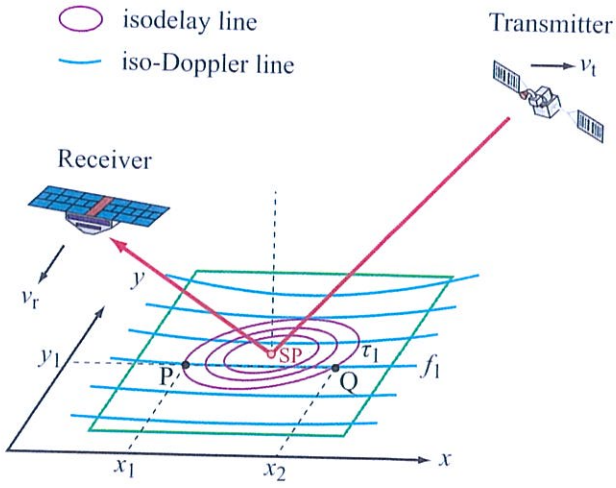

Figure 13-52: Coordinate transformation for the Delay Doppler Map measured by a GNSS-R scatterometer.The specular point (SP) represents the location on the surface with the shortest difference between direct and reflected signal propagation times from the transmitter to the receiver. Longer differences trace out elliptical lines on the surface. The hyperbolae represent lines on the surface of constant Doppler shift. A specific (delay, Doppler) coordinate corresponds to two points (e.g., P and Q) on the surface [Clarizia, 2012].

13-16.1 The Delay Doppler Map

The scattered power received by a GNSS-R sensor is measured by performing a lag correlation of the scattered signal with a time delayed version of the direct signal (or of a replica of the direct signal that is time synchronized to it). The form of the bistatic radar equation given by Eq. (5.29a) can be adapted for use in GNSS-R remote sensing by integrating over the distributed surface target and by explicitly including the effects of the lag correlator (Zavorotny and Voronovich, 2000). The received power can be written as

$$P^r(\tau, f_D) = \frac{P^t \lambda^2}{(4\pi)^3} \iint_A \frac{G_t(x,y)\, G_r(x,y)}{R_t^2(x,y)\, R_r^2(x,y)} \Lambda^2(\tau, x, y) \cdot |S(f_D, x, y)|^2\, \sigma^0(x,y)\, dx\, dy, \tag{13.185}$$

where τ is the difference in time-of-flight between the direct signal and the signal scattered by the surface, f_D is the Doppler shift of the scattered signal relative to the direct signal, P^t is the transmit power, λ is the signal wavelength, R_t and R_r are, respectively, the distances from the scattering target to the transmitter and receiver, G_t and G_r are the transmit and receive antenna gain patterns, Λ is the autocorrelation function of the PRN code for the GNSS signal, S is the response of the Doppler filter, and σ^0 is the bistatic radar cross section per unit area. The integration in Eq. (13.185) is performed over the entire region of diffuse scattering. In general, the received power is highest at the (τ, f_D) coordinates corresponding to the location of the specular point.

The minimum value of τ that produces a surface reflected signal is equal to the difference in time-of-flight between the direct signal and the specular reflection from the surface. If τ is increased above that, scattered power is measured from concentric regions of the glistening zone around the specular point. This is illustrated in Fig. 13-52, which shows a typical spaceborne measurement geometry. The ***specular point*** (SP) and concentric elliptical lines of constant isodelay are shown, together with hyperbolic lines of constant Doppler shift of the transmit carrier frequency. In addition to variations in the time lag of the correlator, the received signal can also be processed through a bank

of Doppler filters to selectively measure scattering along the iso-Doppler lines. Two-dimensional variations of the delay and Doppler values produce a ***Delay Doppler Map*** (DDM) of the scattered power received from the surface. In practice, DDMs are typically sampled over a range of (τ, f) values that includes all significant regions of the glistening zone.

Examples of ocean DDMs measured by UK-DMC-1 are shown in Fig. 13-53 for three different surface conditions. The response of the DDMs to the wind-driven roughening, both in terms of the power scattered from the specular point and the extent of the glistening zone that surrounds it, is consistent with Eq. (13.135). The specular point with the highest scattered power is located at the top of the "horseshoe" shape in the figures. No scattered signal is present for measurements made at lower delay values (above the specular point in the figures). These measurements are typically used to monitor the noise floor of the receiver. Measurements at higher delay values (below the specular point in the figures) map out the glistening zone of the rough surface. Scatter from the specular point decreases, and the extent of the glistening zone increases, with increasing wind speed and roughness.

13-16.2 The Cyclone Global Navigation Satellite System (CYGNSS)

CYGNSS is a NASA spaceborne mission scheduled for launch in 2016. It consists of a constellation of eight microsatellites in low inclination orbit at 500 km altitude (Ruf et al., 2013). Each observatory carries an upgraded version of the UK-DMC-1 GNSS-R receiver. The upgrades permit continuous operation (i.e., 100% duty cycle) with the ability to sample up to 4 reflections simultaneously. The goal of CYGNSS is to better understand the coupling between surface winds and the moist atmosphere within tropical cyclones in order to improve the forecasting of storm genesis and rapid intensification. The ability to measure hurricane force winds with a GNSS-R bistatic radar has been demonstrated by an extensive history of airborne campaigns (Katzberg et al., 2001; Katzberg et al., 2006; Katzberg and Dunion, 2009). The use of a GNSS-R approach enables two key features of the

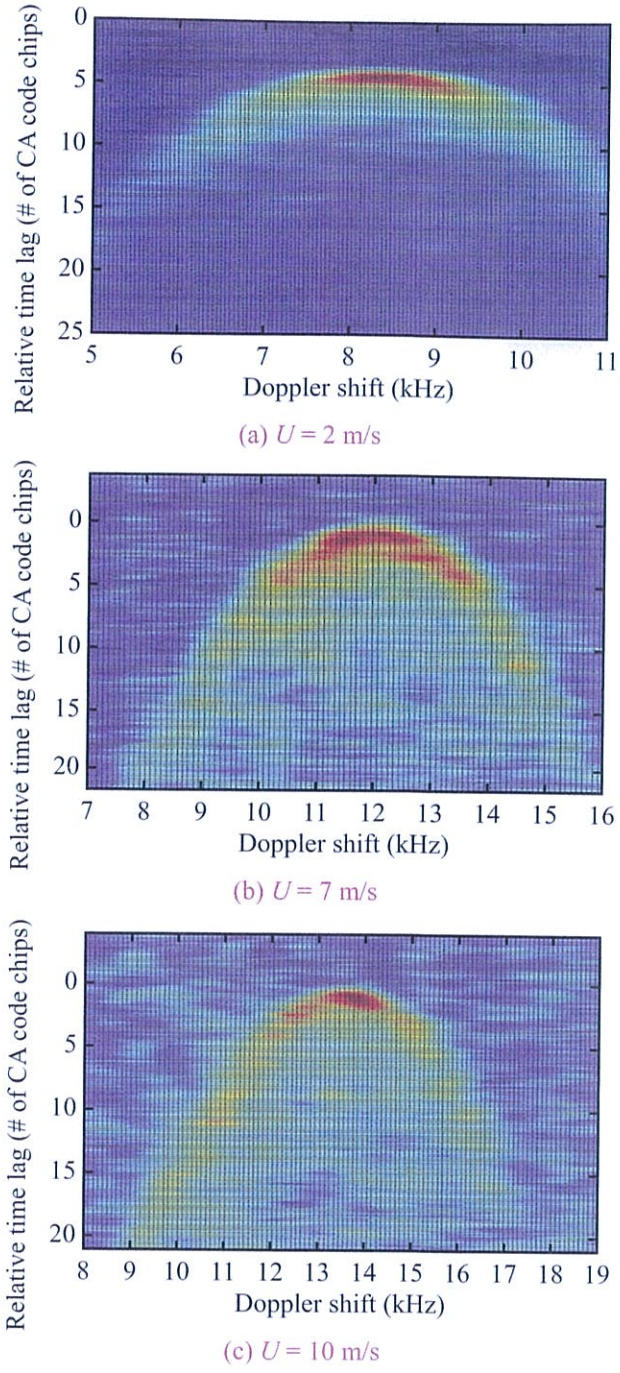

Figure 13-53: Delay Doppler Maps of the ocean surface measured by UK-DMC-1 at surface wind speeds of (a) 2 m/s, (b) 7 m/s, and (c) 10 m/s (referenced to 10 m height above the surface) [Gleason et al., 2005].

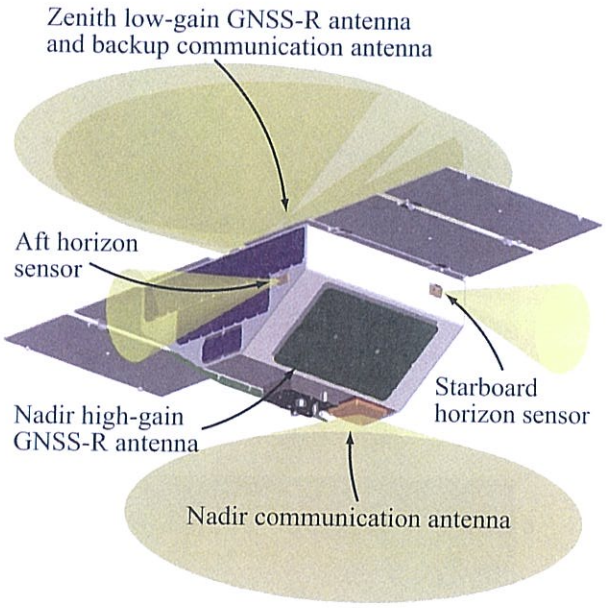

Figure 13-54: The CYGNSS observatory with fully deployed solar arrays measures $159 \times 51 \times 26$ cm, weighs 22 kg, and requires 52 W of power. The keep-out zones for communication antennas and horizon sensors are also shown. The large green panels are its nadir GNSS-R science antennas.

CYGNSS mission. Operation at the GPS L1 carrier of 1575 MHz allows the radar signal to penetrate through the extreme levels of precipitation typically found in the eyewall of a hurricane, which enables the measurement of surface wind speed in its inner core. GPS receivers, with their low power and easy antenna pointing accommodation requirements, allow for the use of small, simple satellites, which makes it affordable to deploy a constellation of eight. An illustration of one of the spacecraft is shown in Fig. 13-54. Use of a constellation produces very frequent (approximately every 3 hours) wind measurements throughout the tropics, which allows for time-resolved imaging of the rapid intensification phase of storm development. The launch of CYGNSS will mark the first time that a GNSS-R sensor is the primary payload on a spaceborne science mission.

PROBLEMS

13.1 A radar system has the following characteristics:

Peak transmitted power $P_t = 10^6$ W
Pulse duration $T_p = 1\mu$s
Bandwidth $B = 1/T_p$
Aperture (effective) area $= 3$ m^2
Wavelength $\lambda = 10$ cm
Noise figure $F = 10$ dB

Determine the received power and the signal-to-noise ratio for a target with a radar cross section of $\sigma = 5$ m^2 at distances of 10, 25, 50, and 100 km.

13.2 A SLAR has the following characteristics:

Peak transmitted power $P_t = 10$ kW
Antenna gain $G = 30$ dB
Wavelength $\lambda = 3$ cm
Horizontal beamwidth $= 0.01$ rad
Pulse duration $T_p = 100$ ns
Receiver bandwidth $B = 1/T_p$
Noise figure $F = 10$ dB

Determine the received power and single-pulse signal-to-noise ratio for $\sigma^0 = -20$ dB, at a height of 5 km and a slant range of 10 km. Assume the antenna boresight is pointed at the target area.

13.3 Three targets are spaced a distance of 5 m apart in a straight line parallel to the axis of motion. They have the same σ and are observed from very far away with a radar operating at a wavelength of $\lambda = 3$ cm.

(a) Sketch the received signal voltage as the radar passes the targets.

(b) Calculate the voltage versus time using the Doppler point of view for a velocity of $u = 50$ m/s.

13.4 Repeat Problem 13.3 with the line of targets perpendicular to the aircraft motion.

13.5 An experimental scatterometer flown on Skylab had the following characteristics:

Signal bandwidth $= 20$ kHz
Noise bandwidth $= 75$ kHz
$T_{S+N} = 1$ s
$T_N = 0.1$ s

Calculate the measurement K_p for the case when the signal-to-noise ratio is -10 dB, 0 dB, and 10 dB. Assume the signal bandwidth is centered in the noise bandwidth.

13.6 A LFMCW radar altimeter uses a chirp bandwidth of 10 MHz with a 100 ms period. Compute the instantaneous frequency of the return difference frequency. What range resolution is achieved?

13.7 Sketch the isorange lines for a radar with 10 m range resolution operation operating at a height of 3 km. The sketch should be to scale and include a minimium of 10 curves that are equally spaced in slant range.

13.8 Sketch the isodops for a radar traveling 200 m/s in level flight at a height of 3 km. Assume a radar operating frequency of 3 GHz. The sketch should be to scale and include a minimium of 10 curves that are equally spaced in Doppler frequency.

13.9 Determine the range-only ambiguity function for a Gaussian pulse envelope given by $p(t) = e^{-t^2/t_0^2}$, where t_0 is a constant. Based on the ambiguity function what is this pulse's equivalent duration and equivalent bandwidth?

13.10 Sketch the range-only ambiguity function for the binary 1101101 where the total pulse duration is T with equally spaced chips. Use continuous integration. What is the equivalent duration and bandwidth of this modulation function? In computing the ambiguity function a 0 should be treated as a -1.